PhD-FSTC-2017-07
The Faculty of Sciences, Technology and Communication

DISSERTATION

Defence held on 27/01/2017 in Luxembourg

to obtain the degree of

DOCTEUR DE L'UNIVERSITÉ DU LUXEMBOURG

EN INGÉNIERIE

by

Srivathsan RAVI
Born on 7 September 1987 in Srirangam (India)

NUMERICAL MODELING OF PIEZOELECTRIC ENERGY HARVESTING DEVICES DRIVEN BY FLOW-INDUCED VIBRATIONS

Dissertation defence committee

Dr.-Ing. Andreas Zilian, Dissertation Supervisor
Professor, Université du Luxembourg

Dr.-Ing. Habil. Sven Klinkel
Professor, RWTH Aachen Universtity

Dr.-Ing. Jean-Régis Hadji-Minaglou, Chairman
Professor, Université du Luxembourg

Dr Jean-François Deü
Professor, Conservatoire National des Arts et Métiers

Dr.-Ing. Bernhard Peters, Vice Chairman
Professor, Université du Luxembourg

Acknowledgments

First and foremost, I wish to express my deepest gratitude to Prof. Andreas Zilian. This dissertation would not have been possible without his continual support and assurances. Prof. Zilian has been a tremendous source of inspiration at all stages of the work. His technical expertise and Zen-like patience have never ceased to amaze me. He was always available to discuss and brainstorm the obstacles that were encountered and knows how to communicate with his students. I thank Prof. Zilian for providing a pleasant research environment and the opportunity to attend conferences during the course of the research. His selfless time and care were often all that kept me going. These four years have been a great learning experience for me. I could not have imagined having a better advisor and mentor for my PhD study.

I would like to thank Prof. Bernhard Peters and Prof. Jean-Régis Hadji-Minaglou for serving as my committee members and providing invaluable insight during the yearly review discussions.

A special thanks to my numerous friends for all the chats and wonderful times we shared over the years. They were fundamental in encouraging and supporting me during the stressful and difficult times.

I am forever indebted to my family for their unparalleled love and support. Without their encouragement this journey would not have been possible.

I thank you Achu for your love and forgiveness throughout these years of separation.

Contents

List of Figures

Chapter 1

Introduction and Literature Review

1.1 Introduction

Energy harvesting or power harvesting refers to the process of deriving useful electrical energy from ambient energy sources such as thermal energy, light energy, and mechanical energy surrounding a system. The research interest in the field of energy harvesting is mainly driven by the technological advances in low-power electronic devices including microelectromechanical systems, portable electronic devices, and wireless sensor networks. Wireless sensor networks in particular have become ubiquitous in medical, industrial, and commercial applications. The portable nature of these devices necessitates their ability to carry their own power supply, which often means relying on batteries for power supply. The demand for more energy consuming features in modern day low-power electronic devices, and a persistent stagnation in the technological development of batteries over the years have provided the necessary impetus for growing research interest in energy harvesting from ambient sources. Among the many ambient energy sources available for power harvesting, vibration-based energy harvesting for powering electronic devices has gained significant attention due to the abundance of vibrational energy which otherwise goes untapped.

There are many methods available to harvest vibrational energy into useful electrical energy. The most prominent methods, as mentioned by Williams and Yates [8], include electrostatic [9], electromagnetic [8, 10], and piezoelectric transductions [1, 11]. Energy harvesting from piezoelectric materials have become prominent, as evident from the number of literature published every year in this field, due to high power densities of piezoelectric materials, smaller size, and relative ease with which they can be designed [12]. Roundy et al. [13] provided a comparison of the three transducers based on their maximum practical and theoretical energy densities, where piezoelectric transduction provided a maximum practical energy density of up to 35.4 $\mathrm{mJcm^{-3}}$ compared to a maximum practical energy density of up to 24.8 $\mathrm{mJcm^{-3}}$ for electrostatic transducers and 4 $\mathrm{mJcm^{-3}}$ for electromagnetic transducers. He mentioned additional considerations that affect the selection of transduction mechanisms. For example, electrostatic transducers are readily implemented in micro-machining processes but require separate voltage cycle to begin the conversion process. Output voltages from electromagnetic transducers are typically well below 1 V in magnitude. Modeling of piezoelectric energy harvesters driven by base-excitations and fluid-flow is the focus of this work.

In basic terms, *piezoelectric effect* or *piezoelectricity* refers to the accumulation of electric charge in certain materials as a response to applied stress. Piezoelectric effect manifests in crystalline materials with no inversion symmetry as a result of coupling between electrical and mechanical behaviors of those materials. Piezoelectric effect is a reversible process and categorized into two parts, namely the *direct* and *inverse* piezoelectric effects. When a piezoelectric material is mechanically strained, there is a change in electric polarization in proportion to the induced strain. This change in polarization leads to an accumulation of electric charge that is collected at the electrodes bonded to the surface of the piezoelectric material. This phenomenon is referred to as the direct piezoelectric effect. It was first experimentally demonstrated by Jaques and Pierre Curie in the year 1880. The inverse piezoelectric effect is characterized by the deformation of a piezoelectric material resulting from the application of an electric field. Gabriel Lippmann, in the year 1881, mathematically deduced the inverse effect from the fundamental principles of thermodynamics. The inverse effect was experimentally confirmed by Curie brothers shortly after.

There are several materials, both natural crystals and man-made, that exhibit a range of piezoelectric effects. Naturally occurring piezoelectric materials include quartz, Rochelle salt, topaz, Berlinite, and biological matter such as dry bone. The piezoelectric effect exhibited by natural materials is very small. As a result, pyrocrystalline ferroelectric ceramics such as barium titanate and lead zirconate titanate (PZT) have been developed with strong electromechanical coupling between the electrical and mechanical states of the materials. The direct and inverse piezoelectric effects manifest in ferroelectric ceramics through a procedure known as poling. Poling of a piezoelectric material is achieved by applying a strong electric field across the material below a material dependent Curie temperature. Piezoelectric materials are characterized by the presence of electric dipole moments present in their crystal lattice below the Curie temperature by virtue of spontaneous displacement of atoms relative to each other or by the presence of molecular groups with electric properties. The dipole moments are initially oriented in parallel to each other in small domains inside the material called Weiss domains. In the presence of an external electric field, these domains—randomly oriented prior to polarization—orient themselves in parallel to the external field causing the macroscopic polarization of the material. The term polarization itself refers to the density of such dipole moments. When the external electric field is removed, the dimensions of the material changes, and there is a remanence of polarization as shown in Fig. 1.1. The orientation of mechanical and electrical axes is determined by the direction of the applied electric field. Although piezoelectric energy harvesters exploit the direct effect of piezoelectric materials, both the piezoelectric effect simultaneously exist in a piezoelectric material.

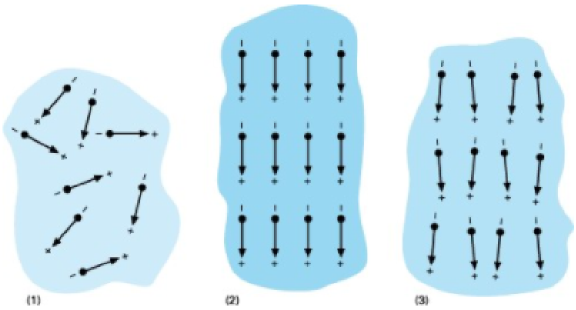

Figure 1.1: **1** Random orientation prior to polarization, **2** during polarization and **3** remanent polarization after removal of the electric field

The power output from piezoelectric energy harvesting devices depends on a lot of factors, including but not limited to, the type of piezoelectric material used, model of piezoelectric coupling, frequency of the ambient vibrations, geometry of the harvesting device, size and shape of the electrodes attached to the piezoelectric material, and the type of harvesting circuit considered. Each of these parameters contribute significantly towards maximization of the power output from a piezoelectric harvester. The predominant focus of this work is on the modeling aspects of base excited and flow-driven piezoelectric energy harvesters. Before reviewing the existing modeling approaches, some seminal works on piezoelectric harvesters driven by both base excitations and fluid flow are reviewed in the next two sections to provide the necessary perspective on various aspects of piezoelectric energy harvesting.

1.2 A Review of Piezoelectric Energy Harvesting Methods

1.2.1 Energy Harvesting from Base Excitations

A wide variety of piezoelectric energy harvesting configurations have been reported in the literature. The most common and the simplest of piezoelectric harvester configurations is a cantilevered beam with one or more piezoelectric layers bonded to a non-piezoelectric substrate layer. A cantilevered harvester configuration that consists of a single piezoelectric layer bonded to a substrate layer, is referred to as a *unimorph* harvester. A *bimorph* harvester is a cantilevered beam where two piezoelectric layers are bonded to either sides of a substrate layer. The piezoelectric layers in a bimorph harvester can be connected in series or parallel based on the intended application. The different configurations can be seen in Fig. 1.2. The electric charge generated due to the direct piezoelectric effect is collected at the electrodes bonded to both sides of the piezoelectric layer. The electrodes are externally coupled an electrical circuit and the type of circuit considered typically depends on the application. Piezoelectric harvesters can operate in two different coupling modes—the –33 mode and the –31—based on the electric field orientation and the polarization direction. In the –31 mode, the force is applied in a direction perpendicular to the polarization direction, and in the –33 mode the force is applied in the same direction as the polarization direction. For a beam type harvester, the coupling mode is determined by the electrode pattern on the piezoelectric layers. The –31 coupling mode in a cantilevered bending harvester is realized by placing the electrodes on the top and bottom surfaces of the piezoelectric layers. The other coupling mode is realized by having all the electrodes on one side of the piezoelectric layer in a pattern that is referred to as interdigitated pattern as shown in Fig. 1.3

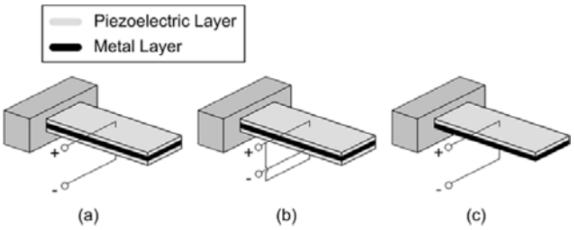

Figure 1.2: Beam type energy harvesters; **a** bimorph configuration - series connection, **b** bimorph configuration - parallel connection and **c** unimorph configuration [1]

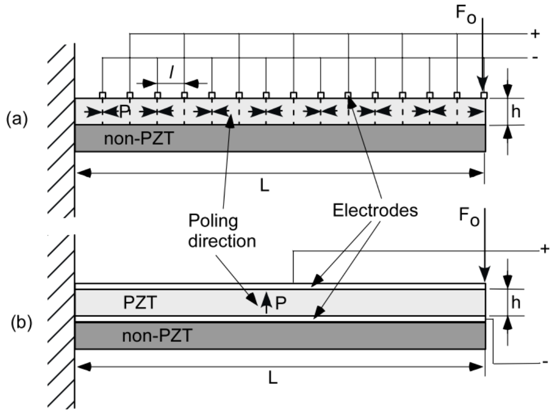

Figure 1.3: Side view of the unimorph bender; **a** –33 mode with interdigitated electrodes and **b** continuous electrode for –31 mode [2]

The energy harvesting performance of unimorph piezoelectric benders was investigated theoretically in Mo et al. [2]. Two types of cantilevers were compared for their energy generating capabilities. The first type was a unimorph bender with interdigitated electrodes exhibiting –33 coupling behavior, and the second type was a conventional was a conventional –31 type bender as shown in Fig. 1.3. The poling direction in the interdigitated electrode was chosen parallel to the stress direction, where the electrodes cover only a portion of the surface. In the other configuration, the electrodes were conventionally placed.

In the interdigitated configuration, it was assumed that the mode in the regions under the electrodes was non-poled. It was found that the interdigitated harvester generated higher voltage output than the conventional bender with an open-circuit voltage 26 times higher than the conventional –31 mode bender. Multiple reasons were cited for the phenomenon such as higher coupling coefficient in the –33 mode compared to the –31 mode and the spacing between the electrodes, which is larger in the case of the interdigitated configuration. A similar study on the influence of coupling modes was carried out by Baker et al. [14]. A piezoelectric stack configuration operating in the –33 mode was compared to a cantilever bender operating in the –31 mode for the amount of electric energy generated per unit of mechanical energy applied. PZT was chosen as the piezoelectric material of choice for both the configurations. When the same force was applied on both the configurations, the power output from the cantilever operating in –31 mode was found to be two orders of magnitude higher than the power output from the stack configuration. The reason for low power output from the stack configuration, despite its higher strain-to-energy conversion rate and robustness, was attributed to the difficulty in inducing appreciable strain due to its high mechanical stiffness. It was concluded from his study that the stack configuration would be able to generate significant energy in environments such as heavy manufacturing facilities, whereas the –31 coupling mode is more suited when the force amplitude is small.

Different types of piezoelectric materials such as single crystals, polymers, piezoceramics, and relaxor-type piezoelectric materials have been used to convert mechanical vibrations to a usable form of energy. The most commonly used piezoelectric material for energy harvesting applications, according to [15], is PZT and its variants PZT-5A and PZT-5H. Although they are the most commonly used materials, PZT is brittle and susceptible to fracture failure; thereby, limiting the straining of the material. To improve flexibility, polymer materials such as *polyvinylidene flouride* (PVDF) have been used for power harvesting, but the piezoelectric coefficients of PVDF are much smaller in magnitude compared to PZT. Apart from piezoelectric ceramics and piezoelectric polymers, piezoelectric composites like *piezoelectric fiber composites* (PFCs) have also been studied for their energy harvesting capabilities. Sodano et al. [16] conducted an experimental comparison between three different piezoelectric materials for power generation. The first harvester type constituted a macro-fiber composite (MFC) with interdigitated electrodes operating in –33 coupling mode. The second harvester incorporated a piezoceramic material with conventional electrode pattern in –31 coupling mode. The third harvester was made of piezoceramic material with an interdigitated electrode pattern. Their results showed that the second actuator type with conventional electrode and poling patter generated an energy of 137 μW at 64 Hz compared to 29 μW generated by the third actuator type and 12 μW by the first actuator made of piezoelectric fiber composite with interdigitated electrodes. It was demonstrated in their study that higher capacitance of the piezoelectric material with interdigitated electrodes deteriorates the power output, therefore impractical to use —33 mode with interdigitated electrodes in real-world applications.

As previously mentioned, cantilever beam type harvesters are one of the most common harvester configurations due to simple design that allows easy integration with many MEMS fabrication processes. In cantilevered beams with constant width (rectangular sections), straining of the piezoelectric material is not uniform. The clamped end of the beam experiences maximum strain, whereas the free end experiences very little strain. This non-uniform strain distribution leads to an under-utilization of the piezoelectric material. Baker et al. [14] studied the effect of strain distribution on the power harvested by optimizing the width of the cantilever configuration. The width was optimized to distribute the strain more evenly in the structure. Experimentally, a 30% increase in power was observed for a cantilevered beam with trapezoidal configuration compared to the conventional rectangular configuration. In a similar study, the effect of strain distribution was investigated experimentally and theoretically by Goldschmidtboeing and Woias [17]. Their results showed that the advantage of triangle-shaped beams in terms of curvature homogeneity was offset by the adverse mass distribution. Thus, the overall efficiency of the triangular beam was only weakly influenced by the beam shape. However, the triangle-shaped beam outperformed the rectangular beam in terms of tolerable excitation amplitude and maximum output power.

One of the most important limitations of a conventional piezoelectric energy harvester is that the natural frequency of the harvester must closely match the natural frequency of the input signal for maximum output power. The design and fabrication of an energy harvester is primarily driven by the knowledge of the driving frequency. In some cases the driving frequency is now known a priori, or the input signal is random. Thus an efficient configuration would be the one that can harvest significant power over a wide range of frequencies. Roundy et al. [13] investigated different methods to design active and passive frequency tuning. Active frequency tuning involves continuous monitoring of the power output and altering the resonant frequency of the harvester accordingly to maximize the output power. Passive tuning involves occasional tuning of the harvester. The tuning is switched off while maintaining new resonance frequency. Roundy et al. [13] stated that as long as the harvester is modeled as a second-order mechanical system, active tuning will never improve the power output of the harvester. Another model suggested by them is designing harvester configurations that inherently possess wide bandwidths of power harvesting. Baker et al. [14] proposed a different solution for the same problem by suggesting a bi-stable mechanism. The mechanism strained the piezoelectric material by snapping it from one stable mode to another. However, experiments showed that the necessary acceleration is four times the gravitational acceleration thereby limiting possible applications of the bi-stable mechanism. For a detailed review of various strategies for increasing the operating frequency range of vibration energy harvesters, the reader is referred to a review published by Zhu et al. [18].

Several studies have been performed on the optimization of the conventional cantilever design for higher power outputs by altering the geometry of the piezoelectric structure, substrate structure, and the electrodes covering the piezoelectric layer. Zhu et al. [19] presented a design study of conventional cantilever piezoelectric harvesters for maximizing the power output. They showed that the power output can be maximized by decreasing the overall length of the harvester. They normalized the power output with gravitational acceleration to be sure that the increase in power output is only due to the change in length and not due to higher acceleration. Power output is usually normalized with the square of acceleration due to gravity if the base acceleration is not kept constant during parametric studies. However, Zhu et al. [19] kept the base displacement constant and normalized the power with respect to gravitational acceleration and incorrectly estimated the influence of beam length on the power output. In another study, Friswell and Adhikari [20] studied the influence of the shape of electrodes on the power output of a harvester. They investigated the performance of a unimorph harvester vibrating in the first mode and connected to a load resistance of 100 kΩ. The length of the piezoelectric structure and the substrate structure were kept the same. They showed that the power output increased by 115 % when the electrode covered approximately half the piezoelectric structure and that a rectangular-shaped electrode is better than a triangular-shaped electrode. They studied the effect of electrode topology for only one resistive load. Thus, it cannot be conclusively said that half coverage is optimal for all situations. Albach et al. [21] performed theoretical and experimental studies on a bimorph harvester made of aluminum core and two PZT layers covered with continuous copper electrodes. They showed that for a given excitation frequency and material properties, power output can be optimized by increasing the beam's dimensions as well as increasing the mechanical stress in piezoceramic layers. The thickness of the beam along with the length direction was optimized in their study leading to a curved geometry. They linearized the curved geometry and obtained a wedge-shaped geometry. The modeling aspects of their study will be discussed later in the chapter. In their experimental investigation, an energy harvester configuration with an optimum linear profile was attached to vacuum pump. The fundamental frequencies of the pump were found to be 50 Hz and 100 Hz. A tip mass was added to the harvester to match the pump frequency. The two piezoceramic layers were connected in parallel. A maximum power output of 15 mW was obtained for a matched load resistance.

The dynamic strain distribution over the length of an energy harvester influences the electric displacement field induced in the harvester. For cantilevered harvesters, vibration modes other than the first mode have strain nodes at certain locations were the dynamic strain changes sign. These strain nodes can have serious impact on the overall power harvested if the electrodes cover the piezoelectric layers fully. Continuous coverage of electrodes for a cantilever vibrating in the second mode will drastically reduce the harvested power due to charge cancellation. This effect was theoretically studied and experimentally demonstrated by Erturk et al. [22]. They proposed that the electrodes be segmented in such a way that the electrode does not cover the location of the strain node. In their experiments, instead of segmenting the electrode, the piezoelectric layer itself was divided into two and placed on either sides of the strain node. The same solution was proposed by Lee et al. [3].

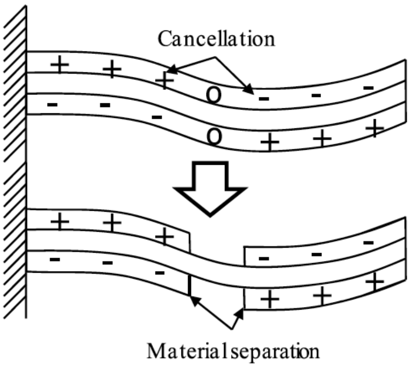

Figure 1.4: Segmented electrode layout to avoid charge cancellation [3]

1.2.2 Energy Harvesting From Fluid Flows

In addition to the focus on piezoelectric energy harvesting from base excitations, recent studies have also focused on harvesting usable energy from fluid flow. A possible energy source present in many locations is the kinetic energy of fluids, i.e wind or water flows. Flow in and around engineering structures may elicit various responses from the structures such as vortex-induced vibrations, flutter, and galloping. These responses may become dangerous and destructive. In many civil engineering applications, methods are often sought to avoid these dangerous interactions of a structure with the surrounding fluid. However, the perspective in flow-driven energy harvesting is to use the available flow energy through controlled hydro or aeroelasticity phenomena and harness potentially harmful structural fluctuations to provide power supply to low-power electronic devices. In flow-driven piezoelectric energy harvesting, the dynamic strain induced in the piezoelectric material by the kinetic energy of the fluid is transformed into electrical energy through direct piezoelectric effect.

Fluid-structure interactions can be classified into three categories based on the excitation mechanism of the structures [23], namely flow-instability induced excitations (IIE), movement-induced excitations (MIE), and extraneous flow-induced excitations (EIE). Instability-induced excitations are characterized by unstable flow regime around a structure caused by the intrinsic properties of the fluid. The flow fluctuations arise beyond a certain value of flow velocity. Vortex-induced vibrations are an example of IIE. Movement-induced excitations are caused due to fluctuating flow forces that arise from vibrations of a structure placed in fluid flow. For example, if there is a perceptible deviation from equilibrium of a structure placed in fluid flow, there is a re-distribution of fluid forces that further increases the initial disturbances. Flutter phenomenon, as a result of the re-distribution of fluid forces around an airfoil due to the feedback from initial disturbance, is an example f movement-induced excitation. Extraneously-induced excitations are independent of any flow instability caused by the structural motion and are caused by flow forces generated by an external energy source.

1.2.2.1 Energy Harvesting From Water Flow

Some researchers have experimentally and theoretically investigated the utilization of these excitation mechanisms for flow-induced piezoelectric energy harvesting. Allen and Smits [24] introduced the concept of energy harvesting eel, where piezopolymer beams shaped like eels were placed behind a bluff body. Dynamic strain was induced in the beams in the fluid developing Kárman vortex sheets. Different membranes ranging from 0.1 mm to 0.7 mm were placed in a water channel running at speeds ranging between 0.05 m/s and 0.8 m/s. Two bluff bodies with widths 5.08 cm and 3.81 cm were used to create the vortex sheets. It was shown that the membranes exhibited lock-in behavior at Reynolds number 20,000 and above. They suggested that the eels must be stiff enough to not dampen the oscillations. Although they provided particle image velocimetry to support their predictions, no explanations were provided regarding the three-way coupling among the different domains.

The study by Allen and Smits [24] was continued by Techet et al. [25]. In their study, multiple eels made of PVDF were stacked vertically behind a single bluff body to study the energy harvesting capabilities of the eels. The lengths of the eels varied between 0.6 mm and 1.2 mm. The eels were 15.25 cm wide with a spacing of 7.6 cm between them to avoid interference during intermittent flapping of the eels. They noted that the flapping of the entire stack was able to lock-in on the frequency of the vortex shedding at velocities above 1 m/s. It was demonstrated that the eels influenced each other to the extent that intermittent flapping was observed even if one of the eels had a phase shift. The motion of the eels was reconstructed by polynomial fit of data obtained from the video. The curvature of the beam was calculated from the strain energy in the material. It was found that the strain was highest at the head and the tail of the beams. Although they studied the straining induced in the eels, power or voltage output from the resulting strain was not quantified.

Another similar study on energy harvesting eels placed in the wake of a bluff body was carried out by Taylor et al. [26]. A number of eels with a total thickness of 150 μm with active PVDF layers were tested in a flow tank at velocities ranging between 0.35 m/s and 0.67 m/s. The generated voltage by the eel was close to 3 V for a flow velocity of 0.5 m/s. Only relative values were given for the power generated making it impossible to compare the results with similar studies presented above.

Flutter response of a piezoelectrically damped cantilever pipe was studied by Elvin and Elvin [27]. A non-dimensional analysis of the overall stability of the system was carried out to investigate the effect of internal damping, mass ratio, load resistance, coupling coefficients, and the location of the piezoelectric structure on the critical velocity. In order to demonstrate the effect of structural damping on the flutter speed, piezoelectric damping was neglected, and the structural and electrical equations were decoupled. It was noted that energy harvesting from instabilities is limited since the critical velocities were relatively high and that the addition of piezoelectric damping could slightly reduce the critical velocity in some cases while increases it in others. The harvesting potential of the pipe's instability is difficult to judge form the results due to the non-dimensional nature of the analysis.

1.2.2.2 Energy Harvesting from Air Flow

Kárman vortex sheets generated by bluff bodies placed in wind flows have also been utilized to study energy harvesting capabilities of piezoelectric energy harvesters. Wind energy can be used to create flapping of flag-like membranes with piezoelectric materials in a unimorph or bimorph configuration. Robbins et al. [28] performed experiments for generating electrical energy from piezoelectric materials placed in wind flow. A cantilever beam with a PVDF layer was attached to a bluff body and placed at the exit of a wind tunnel to harvest wind energy. In the first experiment, a unimorph beam with PVDF layer measuring 25.4 cm in length, 17.78 cm in width, and 0.00508 cm in thickness delivered a power output of approximately 1 mW for a matched load resistance at a wind velocity of 5 m/s. The overall efficiency of the first experiment was rated at 0.03%. Experiments at a flow velocity of 6.7 m/s showed that the power output can be increased to 3 mW if the beam was attached with an end mass weighing 15 g. In a similar study by Pobering and Schwesinger [29], energy harvesting by bimorph beams placed in the wake of a bluff body was investigated experimentally and theoretically. In their experiments, three bimorph beams with length 140 mm, width 11.8 mm, and thickness 0.35 mm were arranged behind each other in the direction of the flow. Power output for a single piezoelectric layer was measured to be 54 μW for a wind velocity of 45 m/s. They noted that water can supply similar power output at much lower velocities due to high energy density.

Akaydin et al. [30] explored experimentally the concept of piezoelectric energy harvesting from turbulent flows with high coherence in spatial and temporal scales. they noted that the turbulent wake of a cylinder at Reynolds number 10,000 and above provide ample opportunities for energy harvesting. In their study, thin flexible cantilever beams with PVDF layer deposited on mylar substrate were placed behind a bluff body. They demonstrated that the most promising arrangement was one where the beam is parallel to the upstream flow. Moreover, the pressure on the beam was affected by two different flow patterns associated with the induced flow ahead and behind the vortices and the low pressure core vortex region. The maximum power output was approximately 4 μW when the distance between the beam and the bluff body is two times the diameter. Significant reduction in the power output was observed when the frequency of vortex shedding was less than the fundamental frequency of the beam.

Erturk et al. [4] conducted experiments on energy harvesting from flow-excited morphing airfoils. The airfoil (Fig. 1.5) with a span on 133 mm and a chord of 127 mm was a bimorph with four M 8557 P1 MFC piezoelectric patches. Only the two piezo patches on the top surface were utilized for energy harvesting. Their experiments showed that a maximum root mean square (RMS) power output of 7 μW was obtained for a 20 degree angle of attach at a flow velocity of 15 m/s.

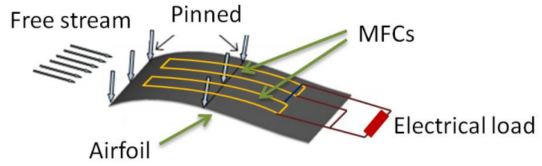

Figure 1.5: Airfoil with MFC patches [4]

In another study, Anton and Inman [31] investigated the possibility of harvesting vibration energy and solar energy from a mini unmanned air vehicle (UAV). They performed an experimental proof of concept study to compare energy harvested from piezoelectric materials and solar panels placed on a UAV. The UAV had a wing span of 1.8 m, a length of 1.1 m and weighed 0.9 kg out of the box. The UAV model was so chosen for its long wing span and flexible foam wings, which provided a conducive environment for vibration harvesting from wing deflections. Two piezoelectric patches—one patch made of PFC and another patch made of MFC—were attached to the wing spar to harvest from the deflection of the wings, and another PFC bimorph cantilever beam was placed on the fuselage to harvest energy from rigid body motions of the aircraft in vertical direction. Results showed that the average power output of the cantilever PFC in the fuselage was 24 μW, the average power output of the MFC attached to the wing spar was 11.3 μW and of the PFC attached to the wing spar was 10.1 μW. It was observed that the higher power output of the cantilever PFC was due to the bimorph configuration. They reported that the piezoelectric patches were able to harvest enough power to fully charge a small battery when the volume of the piezoelectric was increased.

1.3 Review of Piezoelectric Energy Harvesting Models

1.3.1 Models for Base-Excited Harvesters

It is evident from the survey presented in Sect. 1.2 that there are many parameters that influence the power output of a piezoelectric EHD, and a considerable amount of research has been carried out on finding efficient designs and techniques for improving the power harvesting capabilities of piezoelectric energy harvesters. To quantify these influences and develop different strategies for designing energy harvesters for various applications, it is imperative to establish mathematical models to estimate the power outputs of energy harvesters. The fundamental modeling objective of piezoelectric EHDs is the estimation of voltage output across the electric load (circuit) in terms of base motion input and in terms of fluid loading for flow-driven harvesters. The power delivered to the circuit can then be calculated from the voltage output.

Over the past two decades, numerous researchers have proposed different modeling approaches to predict the power output and performance of EHDs. Williams and Yates [8] in 1996 proposed a generalized model for estimating the power generated by an energy harvester through electromagnetic transduction. They represented the energy harvester as as single degree of freedom (SDOF) system with lumped parameters and assumed that the electromechanical coupling is linear and proportional to the velocity. Their model is a reasonable approximation for electromagnetic harvesters but not for piezoelectric energy harvesters. This was stated explicitly by the authors in [8]. Early mathematical modeling approaches for base-excited piezoelectric harvesters were in the form of simplified single degree of freedom and lumped parameter models as well [32, 33]. Although SDOF approaches can provide initial comprehension of the coupled problem, they are restricted to a single vibration mode and fall short in predicting significant features such as dynamic mode shapes, effect of the circuit of the vibrating amplitude, and the effect of strain nodes on the electrical response [34].

Lu et al. [5] proposed a model based on Euler–Bernoulli beam theory for design and analysis of the –31 transverse mode type piezoelectric micro-generator. Although the authors note the importance of matching the fundamental frequency of a harvester to the frequency of the ambient vibrations for maximum power output, their frequency response graphs as shown in Fig. 1.6 do not have any peaks (as seen in plots a and b). This could be due to approximating the effect of electric load on the vibration amplitude as a viscous damping behavior.

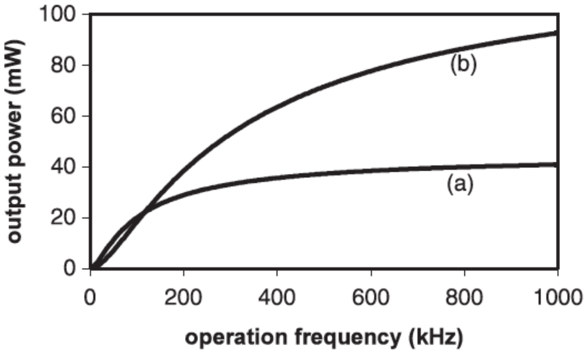

Figure 1.6: Power FRF as reported in [5]

One of the most important contributions to the field of piezoelectric energy harvesting came from Erturk et al. [22, 34–36]. They presented a distributed parameter model based on Euler–Bernoulli beam assumptions. Their comprehensive analytical and experimental studies provide significant insight into the coupled aspects of piezoelectric energy harvesting cantilever beams and address the inaccuracies of SDOF modeling techniques. They accounted for the impact of electrical load on the vibration amplitude of the harvester and showed that the back coupling is more complicated than viscous damping effect. Their results can be compared to Lu et al. [5] to understand why modeling the impact of electrical load as viscous damping would lead to erroneous results. Sodano et al. [11] and Dutoit et al. [33] proposed a Rayleigh-Ritz type discrete formulation for base excited cantilever beams based on Euler–Bernoulli beam theory. Their approach is a discrete version of the distributed parameter model.

Tabesh and Fréchette [37] proposed an improved lumped parameter model based on Euler–Bernoulli beam theory with quadratic electric potential distribution through the thickness of the piezoelectric layer. They showed that linear distribution of electric potential through the thickness of the piezoelectric layer is insufficient to describe the electromechanical behavior of the coupled system as it violates Gauss' law. It is worth remarking that linear electric potential assumption is relied upon in many conventional models (for instance, see [11, 32, 33]). Although some analytical approaches are quite sophisticated in studying the coupled behavior (for instance, see [35,36]), two dimensional analytical approaches are quite limited to simple cases like thin beams with uniform geometry. Numerical solution methods such as finite element method are need to study the electromechanical behavior of complex EHDs.

In their pioneering work on finite element modeling of piezoelectric vibration analysis, Allik and Hughes [38] proposed a finite element formulation with tetrahedral element with mechanical displacements and electric potential as the unknown field variables and took into account both direct and inverse piezoelectric effects. Their work formed the basis of many finite element models, and numerous finite element models have been developed since then–including beam, shell, plate and solid elements—to analyze piezoelectric vibrations. A survey of different finite element formulations for piezoelectrics can be found in [39]. Many finite element formulations (for instance, see [38, 40–45]) employ mechanical displacement and electric potential as the only field variables, and other field variables are derived from these two primary field variables. These finite element formulations can be termed as irreducible finite element formulations. Irreducible elements are susceptible to locking phenomena and mesh distortion when discretizing thin structures. Tzou and Tseng [46] proposed a piezoelectric finite element approach with internal displacement modes to overcome the drawbacks of irreducible elements. In addition to piezoelectric finite elements with incompatible modes/internal degrees of freedom, hybrid piezoelectric finite element formulations have also been proposed to enhance element accuracy and overcome locking phenomena. These formulations contain additional assumed fields besides mechanical displacements and electrical potential. Ghandi and Hagood [47] proposed a hybrid tetrahedral finite element with electric displacement as the assumed field variable in addition to mechanical displacements and electric potential. The most general formulation was presented by Sze and Pan [48] and contained six independent unknown fields, viz., displacements, strains and stresses for the mechanical part and electric potential, electric field and dielectric displacements for the electric part. Further mixed formulations with three and four assumed fields are derived from the six field formulation. A six field formulation was proposed by Klinkel and Wagner [49, 50] with additional enhancements for strain and electric field.

It is worth mentioning here that many of the models cited above assume linear approximation of the electric potential through the thickness of the piezoelectric layer. As mentioned earlier, such an assumption violates Gauss' law. In his review article, Benjeddou [39] clearly pointed out that the electromechanical coupling is only partial in case of a linear approximation. Also, Yang [51] investigated the bending of a plate with piezoelectric actuators and showed that a quadratic approximation of electric potential is necessary in bending dominated problems. Wang [41] presented a finite element model with each element divided into a number of finite sub-layers and a linear though-the-thickness approximation of the potential in each sublayer. By increasing the number of layers in the thickness direction, their model was able to capture the quadratic variation of the potential in the thickness direction of the piezoelectric layer. He concluded that in case of short-circuit condition, linear approximation will not be able to capture the induced potential; however, the global response of the system will not vary much in the case of thin beams. In their study, Klinkel and Wagner [49] assumed a bilinear approximation of the electric field through the thickness of the shell element in addition to a linear approximation of the electric potential. This led to an exact fulfillment of the charge conservation law in bending dominated situations.

It is also pertinent to mention that finite element modeling as an advanced and reliable numerical model has mostly been used to model piezoelectric materials either as sensors or actuators. Almost all the references above are finite element formulations for piezoelectric elements as sensors or actuators. This is also the reason why electrical degrees of freedom are condensed from the global system of equations as done in [38,40,46]. In actuation application, the material deformation is due to the applied voltage. This applied voltage appears as an external forcing term; hence, the system's stiffness remains elastic [44]. In sensing applications, there is added stiffness due to the voltage developed from straining of the piezoelectric material. Thus, finite element formulation for both applications can be reduced to that of a standard elastic vibration problem. However, finite element formulations for energy harvesting applications must account for the electrical load and its influence on the vibration characteristics. Zhu et al. [19, 43] presented a coupled piezoelectric-circuit finite element method, where the circuit consisted of a resistor element. Thomas et al. [44] presented a finite element formulation for piezoelectric shunt damping applications. In both the cases, the approximation of electric potential was assumed to be linear through the thickness of the piezoelectric patch.

1.3.2 Models for Flow-Driven Harvesters

Flow-driven piezoelectric energy harvesting is a strongly coupled problem characterized by complex, three-way coupling of the fluid, the piezoelectric structure, and the electrical circuit. It can be seen from the recent surveys [1, 52–54] that the research—experimental and theoretical—in piezoelectric energy harvesting has focused predominantly on exploiting base excitations, and the focus on flow driven harvesters has rather been limited. Erturk et al. [55] presented a mathematical model for analyzing the energy harvesting potential of piezoaeroelastic systems. They presented a frequency domain analysis of a wing-based piezoaeroelastic energy harvester. In order to gain preliminary insight, they considered a lumped parameter wing-section model, where the piezoelectric coupling was introduced to the plunge degree of freedom along with two structural damping coefficients. A resistive load was considered as the circuit component. They experimentally investigated the effect of piezoelectric coupling on the linear flutter speed and reported an harvested power of 10.7 mW for a resistive load of 100 kΩ at a free stream velocity of 9.30 m/s. They reported a good match between the experimental data and their mathematical model.

De Marqui et al. [56] presented a time-domain piezoaeroelastic model for airflow excitation of cantilevered plates representing a wing-like structures with embedded piezoelectric material for continuous and segmented electrode configurations. Their piezoaeroelastic model was a combination of electromechanically coupled finite element model [42] and an unsteady vortex-lattice aerodynamic model. They studied the electrical power output and displacement at the wing tip for different airflow speeds using continuous and segmented electrode configurations. The interaction between the aerodynamic and the electromechanical domain was captured by an iterative method, and the aerodynamic loads and the structural motion were obtained from distinct numerical methods with distinct meshes. De Marqui et al. [57] expanded their time domain model to include frequency domain analysis for the same wing generator. The unsteady aerodynamic model in this case was based on the doublet-lattice method, and the electromechanically coupled finite element model was combined with the doublet-lattice model to obtain FRFs. Although the models proposed by both Erturk et al. [55] and De Marqui et al. [42, 57] are in good agreement with the experimental data, they are specific to piezoaeroelastic energy harvesting problem, and their applicability to other types of fluid-structure interactions is not discussed in their publications.

Akaydin et al. [58] explored energy harvesting from unsteady turbulent flow using piezoelectric materials, where the action of turbulent boundary layers and wakes of circular cylinders at high Reynolds numbers on piezoelectric cantilever beams was investigated. They used FLUENT software to analyze the three-way interaction accounting for the aerodynamics, structural vibrations, and the electrical response of the piezoelectric material. Navier-Stokes equation was considered to model the incompressible flow field, and the piezoelectric beam was modeled as a SDOF system. As mentioned earlier, SDOF model is a simple approximation of the coupled system and is limited to single vibration model of the beam. The authors themselves suggested the use of strongly coupled methods to improve their modeling approach.

To analyze piezoelectric energy harvesting from vortex-induced vibrations of a circular cylinder, Mehmood et al. [6] presented a numerical model where the balance equations were solved using an accelerated reference frame technique, and the circular cylinder with piezoelectric patch was modeled as a SDOF system as shown in Fig. 1.7. The governing equations were solved simultaneously, and the coupling scheme was based on Hamming fourth order predictor-corrector technique.

More recently Amini et al. [59] presented a more comprehensive numerical model for analyzing piezoelectric harvesting from fluid-structure interactions. Their numerical model was a combination of open-

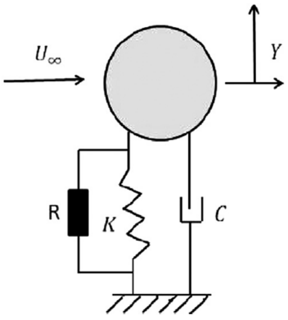

Figure 1.7: Rigid cylinder as presented in [6]

FOAM solver for the fluid domain and finite element method for the piezoelectric structure. The finite element model was based on Euler–Bernoulli approximations with linear through-the-thickness approximation of the electric potential. The model was validated against the results form the model proposed by Akaydin et al. [58]. The modeling approach proposed by Amini et al. [59] is more comprehensive than the model presented in [58].

1.4 Research Objectives

From the review of experimental and modeling approaches for piezoelectric energy harvesting given in this chapter, it is evident that vastly different experimental and modeling approaches have been proposed for base-excited and flow-driven piezoelectric energy harvesters. Reliable and validated analytical models for conventional harvester configurations (e.g. cantilever beams) are commonly found in the literature. When available, analytical solutions and related closed form expressions can provide significant insight into the physics of the problem. They are faster than the numerical solution approaches and help identifying relevant system parameters. However, analytical solutions and closed form expressions are challenging for even moderately complex harvester configurations, and numerical solution techniques become indispensable for analyzing such harvester configurations. The limitations of simpler models such as the distributed-parameter models and phenomenological models are more evident in the case of flow-driven piezoelectric energy harvesters.

Numerical modeling of flow-driven energy harvesters is a very challenging task because of the three-way information exchange between the different physical domains. It has been pointed out in many studies that modeling the effect of electric circuit as some form of viscous damping effect on the harvester will lead to erroneous results. The effect of attached circuit is more sophisticated than viscous damping, and in flow-driven harvesting whatever impact the circuit has on the harvester will in turn affect the flow characteristics of the fluid. In order to obtain the structural deformations and the power generated for a given resistive load, the fluid loads must first be determined. However, the fluid loading profile in turn depends on the structural vibration and the load resistance. Obtaining a mathematical expression for the pressure force on a piezoelectric harvester from fluid loading is not possible, and in most practical scenarios this pressure force is not harmonic in nature. Thus, analytical solutions for harvester deformation is out of the question. It can be seen from the review that almost all the numerical models for flow-driven harvesting follow a partitioned approach for solving the fluid-structure interaction problem. Although Mehmood et al. [6] presented a simultaneous solution, the harvester in their model is considered as spring-mass-damper system, leading to oversimplification of the problem. Partitioned-solution approaches (strongly coupled and loosely coupled) do have advantages. One advantage is that existing sophisticated solvers for each domain can be modified with little effort for application in flow-driven energy harvesting. Another advantage is the possibility of sub-cycling if there is a mismatch in time scales between the flow field and the piezoelectric structure.

In simultaneous solution methods, there is no strict partitioning of the physical domains, and the discretized model equations for the solid and fluid are treated as a single algebraic system of equations and solve din a single iteration loop with consistent time integration schemes for all the physical domains For strongly coupled problems, simultaneous solution approaches ensure stability and accelerated convergence of the coupled system [7]. A monolithic method ensues if the algebraic equations resulting from the discretization schemes chosen for the involved physical domains are solved for in one single system of equations. While plenty of two-dimensional and three-dimensional finite element formulations exist for piezoelectric applications, a sophisticated three-dimensional simultaneous solution approach without restricting assumptions in the context of flow-driven energy harvesting is missing in the literature.

The primary objective of this research work is to develop a computational framework for uniform and simultaneous analysis of smart, low power energy harvesting devices in the context of vibration based energy harvesting and flow-driven piezoelectric energy harvesting. The computational framework will enable reliable sensitivity, robustness and efficiency studies of the non-linear coupled system involving fluid, structure, piezoceramics and electric circuit. The proposed formulation is based on a holistic three-dimensional continuum mechanics modeling approach that utilizes a mixed-hybrid stabilized space-time finite element method for analysis of the coupled system in time and frequency domain. The three dimensional modeling approach enables consistent usage of electrical and mechanical quantities without relying on simplistic assumptions. There are no assumptions on electrostatics, leading to proper satisfaction of the Gauss law. Mixed-hybrid formulation enables overcoming locking phenomena, which is frequently encountered in modeling thin geometries with three-dimensional elements. The proposed formulation is capable of analyzing structures with non-uniform geometries and material properties. Many of the existing mathematical models for piezoelectric energy harvesters have come from research groups belonging to various disciplines. This has often led to oversimplification of certain aspects of the coupled problem. In the lumped parameter modeling approach, for example, the electrical domain consists of the inherent capacitance of the piezoelectric material and the components of the electrical circuit considered. If similar lumped parameters can be made available for the mechanical domain, then the parameters from both the domains can be coupled through piezoelectric constitutive equations. This is a convenient approach is some cases, but this has severe restrictions when it comes to analyzing harvesters with complex geometries and material distribution. It is also the aim of this research to bridge this gap and develop a framework that can be relied upon by these research groups from various disciplines.

Monolithic solution approaches are considered to be more robust than the partitioned (segregated) approaches and proven to be effective even for weakly coupled fluid-structure interaction problems [60]. They provide good convergence even if the behavior of the subsystem is different from the fully coupled system provided the non-linearities are sufficiently resolved [7]. The formulation of the coupled-system as a single algebraic system of equations requires effective preconditioners for iterative solutions. Furthermore, unlike a segregated solution approach which can use and modify existing sophisticated solvers, a new solver for monolithic approach with suitable preconditioner has to be developed, implemented and validated. To that extent, the formulation proposed in this dissertation is developed in an object-oriented python code framework. The developed model is then applied to analyze base-excited piezoelectric bimorph harvesters in time and frequency domain and to analyze the case of a piezoelectric unimorph placed in fluid flow. The circuitry for implementing piezoelectric energy harvesting for practical applications may include different components like a rectifier to convert alternating current from the harvester to direct current, a capacitor to store the energy harvested, or a simple resistive electrical load to predict the power output of a piezoelectric EHD. In this dissertation the circuit is considered to consist of a resistive load. The electromechanical behavior of thin cantilevered piezoelectric EHDs connected to a resistive load has been extensively studied using a variety of analytical modeling approaches (for instance, see [32, 33, 35, 36, 61]). Thus, literature on circuit design and materials research are not reviewed in this work.

1.5 Dissertation Layout

The dissertation is presented as an accumulation of articles that have been published/submitted for publication during the course of the research. Each chapter is to read as a stand-alone work that demonstrates different aspects of the harvesting problem. Since the chapters are reproduction of the articles, key concepts are found in all the chapters. The organization of the chapters is as follows:

The second chapter of this thesis presents an electromechanically coupled frequency domain analysis of bimorph piezoelectric energy harvesters for series and parallel configurations of the piezoelectric layers. The weak form of the governing equations is formulated as a single coupled integral equation with six independent unknown field variables in a mixed-hybrid framework. The element level field variables are eliminated from the global equation through dynamic condensation which results in a pseudo-rational eigenvalue problem. The solution to the rational eigenvalue problem results in the eigenfrequencies and the corresponding mode shapes for the bimorph harvester for any value of resistive load. The results are compared with the results from the simplified mechanical model proposed by Erturk et al. [36]. This chapter is reproduced as published in Acta Mechanica journal under the title *Monolithic modeling and finite element analysis of piezoelectric energy harvesters.*

The third chapter improves upon the formulation by presenting time-domain analysis for the electromechanically coupled problem. The difference in formulation between the time and frequency domain analysis is elucidated. This chapter introduces the space-time finite element formulation concept for analysis in time domain. The element level degrees of freedom are eliminated from the global equation by static condensation. Discontinuous Galerkin method is utilized for integrating the monolithic model in time. Comparison of the results between the frequency and time domain analysis is presented along with the results from the simplified mechanical model proposed by Erturk et al. [36]. The inaccuracies in linear approximation of electric potential through the thickness of the piezoelectric layer and the effect of electrode coverage on the harvested power are also studied in this chapter. This chapter is reproduced here as published in International Journal for Numerical Methods in Engineering (IJNME) under the title *Time and frequency domain analysis of piezoelectric energy harvesters by monolithic finite element modeling.*

The fourth chapter extends the monolithic space-time formulation to include fluid domain for analyzing flow-driven piezoelectric energy harvesters. The coupling between the different domains including the formulation for moving mesh is detailed in this chapter. The monolithic formulation is applied to analyze the case of a lid driven cavity with flexible piezoelectric unimorph bottom wall. The test case provides a suitable platform to assess the performance of the solver as well as the intricacies in modeling flow-driven energy harvesters. The formulation presented in this chapter was published as an exploratory chapter in a book compiled by Prof. A. Ibrahimbegovic for Springer publications [62] and an edited version was published in Proceedings in Applied Mathematics and Mechanics [63]. This chapter will be soon be submitted for publication with the inclusion of additional test cases.

The final chapter provides an overview of the results along with perspectives on future work.

Chapter 2

Frequency Domain Analysis of Piezoelectric Energy Harvesters

Abstract

This chapter is devoted to monolithic modeling of piezoelectric energy harvesting devices. From a modeling perspective, piezoelectric energy harvesting is a strongly coupled phenomenon with two-way coupling between the electromechanical effect of the piezoelectric material and the harvesting circuit. Even in applications related to shunt damping, where the attached electrical circuit is passive, accurate modeling of the strong coupling is crucial for proper evaluation of the relevant parameters. The chapter proposes a monolithic mixed-hybrid finite element formulation for the predictive modeling and simulation of piezoelectric energy harvesting devices. The governing equations of the coupled electro-mechanical problem are converted into a single integral form with six independent unknown fields. Such a holistic approach provides consistent solution to the coupled field equations which involve structural dynamics, electromechanical effect of the piezoelectric patches and the dynamics of the attached harvesting circuit. This allows accurate computation of the eigenvalues and corresponding mode shapes of a harvester for any finite resistive load coupled to the harvester. The fully three-dimensional mixed-hybrid formulation is capable of analyzing structures with non-uniform geometry and varying material properties. The results of the finite element model are verified against the analytical results of a bimorph harvester with tip mass reported in the literature.

2.1 Introduction

In concise terms, piezoelectricity is the accumulation of electric charge in certain crystalline materials with no inversion symmetry as a response to mechanical strains. This effect is called the direct piezoelectric effect. This phenomenon is a reversible process which is characterized by the change in the materials' dimension when subjected to an external voltage. This is called the inverse piezoelectric effect. Piezoelectric energy harvesting devices (EHDs) exploit the direct effect of the piezoelectric materials to generate electrical energy from ambient vibrations. Typical piezoelectric EHDs are manufactured as thin cantilever beams, where an elastic substrate material is attached to one (unimorph) or two (bimorph) layers of piezoelectric patches and connected to a harvesting circuit. In some cases, two piezoelectric patches are directly attached to each other without a non-piezoelectric substrate layer in between. In addition to being used as energy harvesters, piezoelectric materials are utilized for shunt damping applications as well. Piezoelectric materials can also be used as actuators by exploiting the inverse effect. A detailed review on various forms of piezoelectric energy harvesting can be found in [1, 11].

A considerable amount of literature has been published on mathematical modeling of piezoelectric materials in general and piezoelectric energy harvesters in particular. The analytical solutions found in the literature are typically in the form of single degree of freedom models (SDOF) and beam models, which are commonly referred to as lumped parameter and distributed parameter approaches respectively [32, 33, 35, 36, 61]. The lumped parameter approach is the most basic approximation of piezoelectric devices and limited to a single vibration mode. Although SDOF modeling approaches provide some basic insight, they lack the sophistication needed to account for the strongly coupled aspects of the physical problem. A seminal contribution in the area of piezoelectric energy harvesting came from Erturk and Inman [35, 36, 55]. They presented a distributed modeling approach based on Euler–Bernoulli beam assumptions. Their comprehensive analytical and experimental studies provide significant insight into the coupled aspects of piezoelectric energy harvesting cantilever beams and address the inaccuracies of SDOF modeling techniques. Analytical approaches with closed-form solutions are limited to simple geometries, and numerical solutions are needed to study the electromechanical behavior of complex EHDs.

Allik and Hughes [38] presented a significant and pioneering work on finite element modeling of piezoelectric structures. They proposed a formulation with mechanical displacements and electric potential as unknowns and presented a tetrahedral element with the aforementioned unknowns as nodal degrees of freedom. Both direct and inverse piezoelectric effects were included in their formulation. The electrical unknowns were statically condensed leading to a standard elastic vibration problem. Their work formed the basis of many finite element models, and a survey of different finite element formulations for piezoelectric beam, shell, plate and volumetric structures can be found in [39]. Most of the finite element models presented in the survey can be classified as irreducible formulations, where the only unknown field variables are mechanical displacements and electric potential. To alleviate the problem of locking and mesh distortion in irreducible elements, many mixed and hybrid finite element formulations have been proposed [47–49, 64]. Sze and Pan [48] presented the most general formulation containing six independent fields. [49, 50] presented a six-field formulation with additional enhancements for strain and electric field to reduce further locking.

It is pertinent to mention some of the common assumptions in modeling of piezoelectric structures found in the literature. Some conventional models considered a linear approximation of electric potential through the thickness of the piezoelectric patch [11, 33]. However, this approximation was proven to be incorrect [49, 51]. In his review article, Benjeddou [39] clearly pointed out that the electromechanical coupling is only partial in case of a linear approximation. Also, Yang [51] investigated the bending of a plate with piezoelectric actuators and showed that a quadratic approximation of electric potential is necessary in bending-related problems. In his study, [49] assumed a bilinear approximation of electric field through the thickness of the shell element in addition to a linear approximation of the electric potential. This lead to exact fulfillment of the charge conservation law in bending-dominated situations. In applications where the piezoelectric patches are connected to external circuits, the dynamics of the electrical circuit must be taken into consideration. In some studies, the impact of the attached electrical circuit was modeled as viscous damping [5, 65]. This approach was shown to be highly inaccurate by Erturk and Inman [35, 36, 55] in their analytical formulations. Thomas et al. [44] presented an irreducible finite element model for piezoelectric patches connected to an electrical circuit for applications related to shunt damping. Their formulation contained only two piezoelectric variables per patch, namely the voltage between the patches electrodes and the charge accumulated on each electrode. The circuit equation was added to the system of equations as an additional relation between voltage, charge and their respective time derivatives. Becket et al. [66] also presented a similar formulation for shunt damping applications.

A monolithic finite element formulation that provides simultaneous solution to the strongly coupled system is proposed here. The monolithic approach enables to accurately capture the effect of the harvesting circuit. The governing equations of the coupled problem are formulated in a single integral form with six assumed field variables, namely the mechanical velocities, electric potential rate, boundary charge, electric potential, mechanical stresses and dielectric displacements. The originality of the formulation is that it enables to calculate the eigenfrequencies and the corresponding mode shapes of a harvester for any given harvesting circuit. The goal is to propose a monolithic model that is not restricted by the considerations of the geometry, and a model with appropriate electrical boundary conditions that can accurately represent the strong two-way coupling. The proposed formulation can easily be extended to include fluid domain in this monolithic framework for studying flow-driven energy harvesters [62]. This is one of the primary motivations behind the choice of velocities and electric potential rate—instead of displacements and electric potential—as one of the primary field variables.

2.2 Governing Equations: Linear Piezoelectricity

The strong and integral forms of the equations governing the electromechanical behavior of an arbitrary piezoelectric structure are introduced in this section. The model equations are based on the assumptions of linear piezoelectricity and small deformations. The model incorporates three-dimensional piezoelectric constitutive law.

2.2.1 Strong Form Equations: Velocity Potential Rate Formulation

For an arbitrary piezoelectric structure occupying a domain Ω_p with boundary $\partial\Omega_p$, the rate form of the material law describing the direct and inverse piezoelectric effects is given by

$$\dot{\mathbf{S}} - [s^{\vec{D}}]\dot{\mathbf{T}} - [g]^\top \dot{\vec{D}} = \mathbf{0} \quad \text{in} \quad \Omega_p, \tag{2.1}$$

$$\dot{\vec{E}} - [g]\dot{\mathbf{T}} - [\varepsilon^{\mathbf{T}}]^{-1}\dot{\vec{D}} = \vec{0} \quad \text{in} \quad \Omega_p, \tag{2.2}$$

where $\mathbf{T}$ is the stress tensor, $\mathbf{S}$ is the strain tensor, $\vec{E}$ is the electric field vector, $\vec{D}$ is the vector of electrical displacements, $[s^{\vec{D}}]$ is the elastic compliance matrix measured at constant electrical displacement, $[g]$ is the matrix of piezoelectric coupling coefficients in strain-voltage form, and $[\varepsilon^{\mathbf{T}}]$ is the dielectric matrix measured at constant stress. It should be noted that $\mathbf{S}$ and $\vec{E}$ are energy conjugates of $\mathbf{T}$ and $\vec{D}$ respectively, and equivalent representations of Eqs. (2.1) and (2.2) can be obtained by using different forms of piezoelectric coupling coefficients. It should also be noted that all mechanical quantities are one tensorial rank higher than the corresponding electrical quantities.

The mechanical equilibrium equation is given by

$$\rho\dot{\vec{v}} - \vec{\nabla}\cdot\mathbf{T} - \vec{f} = \vec{0} \quad \text{in} \quad \Omega_p, \tag{2.3}$$

where Eq. (2.3) corresponds to the conservation of linear momentum of a solid body for small deformations. Here, ρ denotes the mass density of the piezoelectric structure, $\vec{v}$ the vector of structural velocities, and $\vec{f}$ the vector of body forces. The gradient relation between the linear strain rate tensor and the velocity is given by

$$\dot{\mathbf{S}} - \frac{1}{2}[\nabla\vec{v} + (\nabla\vec{v})^\top] = \mathbf{0} \quad \text{in} \quad \Omega_p. \tag{2.4}$$

A quasi-static approach is adequate to describe the electrical behavior of the piezoelectric structure. Moreover, the piezoelectric structure is considered to be a perfect insulator with no volumetric charge density. Thus, the fundamental electrostatics equations are:

$$\nabla\cdot\vec{D} = 0 \quad \text{in} \quad \Omega_p, \tag{2.5}$$

$$\dot{\vec{E}} + \nabla\psi = \vec{0} \quad \text{in} \quad \Omega_p. \tag{2.6}$$

Equation (2.5) is the differential form of Gauss' law, and Eq. (2.6) is the gradient relation between the electric field rate $\dot{\vec{E}}$ and the rate of electric potential ψ.

The boundary $\partial\Omega_p$ of Ω_p can be subdivided such that $\partial\Omega_p = \Gamma_p^v \cup \Gamma_p^t = \Gamma_p^\psi \cup \Gamma_p^q$, where $\Gamma_p^v \cap \Gamma_p^t = \Gamma_p^\psi \cap \Gamma_p^q = \emptyset$. Γ_p^v is the part of $\partial\Omega_p$ subjected to mechanical essential boundary condition, and Γ_p^t is the part of $\partial\Omega_p$ subjected to mechanical natural boundary condition. They are given by

$$\vec{v} - \bar{\vec{v}} = \vec{0} \quad \text{on} \quad \Gamma_p^v, \tag{2.7}$$

$$\mathbf{T}\cdot\vec{n} - \bar{\vec{t}} = \vec{0} \quad \text{on} \quad \Gamma_p^t, \tag{2.8}$$

where $\bar{\vec{v}}$ and $\bar{\vec{t}}$ are prescribed boundary velocities and tractions, respectively. Similarly, electrical essential and natural boundary conditions are given by

$$\psi - \bar{\psi} = 0 \quad \text{on} \quad \Gamma_p^{\psi}, \tag{2.9}$$

$$\vec{D} \cdot \vec{n} + \bar{q} = 0 \quad \text{on} \quad \Gamma_p^{q}, \tag{2.10}$$

where $\bar{\psi}$ and $\bar{q}$ are prescribed electric potential rate and free charge density per unit surface area, respectively.

2.2.2 Weighted Residual Formulation: Mixed formulation

The weak formulation of the strong form equations is expressed in terms of four unknown fields, namely the velocities $\vec{v}$, the stresses $\mathbf{T}$, the electric potential rate ψ and the electric displacement $\vec{D}$. It is obtained from the strong form equations by the method of weighted residuals and reads after integration by parts as

$$\begin{aligned}
&\int_{\Omega_p} \delta\vec{v} \cdot (\rho\dot{\vec{v}} - \vec{f}) \, \mathrm{d}\Omega_p + \int_{\Omega_p} \dot{\mathbf{S}}(\delta\vec{v}) : \mathbf{T} \, \mathrm{d}\Omega_p + \int_{\Omega_p} \dot{\vec{E}}(\delta\psi) \cdot \vec{D} \, \mathrm{d}\Omega_p && \text{(2.11a)}\\
&+ \sum_{e} \int_{\Omega_p} \delta\mathbf{T} : ([s^{\vec{D}}]\dot{\mathbf{T}} + [g]^{\top}\dot{\vec{D}} - \dot{\mathbf{S}}(\vec{v})) \, \mathrm{d}\Omega_p && \text{(2.11b)}\\
&+ \sum_{e} \int_{\Omega_p} \delta\vec{D} \cdot ([g]\dot{\mathbf{T}} + [\varepsilon^{\mathbf{T}}]^{-1}\dot{\vec{D}} - \dot{\vec{E}}(\psi)) \, \mathrm{d}\Omega_p && \text{(2.11c)}\\
&- \int_{\Gamma_p^t} \delta\vec{v} \cdot \bar{\vec{t}} \, \mathrm{d}\Gamma_p + \int_{\Gamma_p^q} \delta\psi\bar{q} \, \mathrm{d}\Gamma_p \;=\; 0 \qquad \forall \; \delta\vec{v},\; \delta\psi,\; \delta\mathbf{T},\; \delta\vec{D}. && \text{(2.11d)}
\end{aligned}$$

In Eq. (2.11), line (a) corresponds to the weak form of the momentum conservation equation and Gauss' law. In lines (b) and (c), the linear piezoelectric material is considered in integral form on element level leading to a mixed formulation. The last line represents the integral form of the mechanical and electrical Neumann boundary conditions, respectively.

The foregoing mixed formulation with four independent field variables is similar to the variational form presented in [48]. The point of departure is the consideration of velocities and potential rate in Eq. (2.11) in contrast to the classical formulations based on structural displacements and electric potential.

2.3 Piezoelectric Energy Harvesting

The boundary value problem introduced in Sect. 2.2, along with the weak formulation, pertains to any stand-alone piezoelectric structure. However, a piezoelectric structure without conducting electrode(s) has no structural application, because electrode(s) are essential for applying electrical boundary conditions. In applications pertaining to shunt damping and energy harvesting, piezoelectric layer(s) are covered with two or more electrodes that are connected to an electric circuit. The circuit can be active or passive depending on the intended application. Typical piezoelectric EHDs are multilayered structures made of piezoelectric and non-piezoelectric (conducting or dielectric) layers. The EHD is usually placed on a vibrating host structure, and the straining introduced in the piezoelectric layers is converted into an alternating voltage output across the electrodes covering the piezoelectric layers. In this section, we redefine the boundary value problem to include the expressions for electrodes covering the piezoelectric layers and the attached electrical circuit. The expressions thus obtained are included in the general formulation established in Sect. 2.2, leading to a monolithic representation of the coupled harvesting problem.

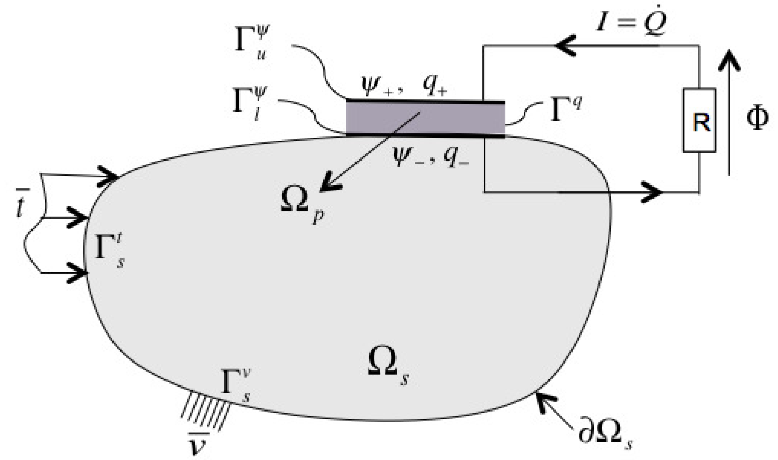

Figure 2.1: An elastic structure with a piezoelectric patch: 2D illustration

As an illustration, we consider an elastic structure occupying a domain Ω_s and equipped with a piezoelectric layer occupying a domain Ω_p (Fig. 2.1). The piezoelectric layer is assumed to be continuously covered on the top and bottom surfaces with perfectly conducting electrodes. The electrodes are equipotential surfaces with negligible thickness. The surfaces of the upper and lower electrodes are denoted by Γ_u^ψ and Γ_l^ψ respectively, such that $\Gamma_p^\psi = \Gamma_u^\psi \cup \Gamma_l^\psi$. In this example, a resistive load (R) is considered as the attached circuit, which is a common assumption in modeling piezoelectric EHDs.

Piezoelectric Layer Equations (2.1)–(2.6) are used to describe the electromechanical behavior of the piezoelectric structure in this example. The electrical boundary conditions, however, are redefined to account for the presence of conducting electrodes and the electrical circuit. We consider the following partition of the boundary $\partial\Omega_p$ of the piezoelectric structure:

$$\Gamma_p^v \cup \Gamma_p^t = \Gamma_p^\psi \cup \Gamma_p^q = \partial\Omega_p, \tag{2.12}$$

$$\Gamma_p^v \cap \Gamma_p^t = \Gamma_p^\psi \cap \Gamma_p^q = \emptyset, \tag{2.13}$$

where Γ_p^v is the part of $\partial\Omega_p$ on which velocities may be prescribed, and Γ_p^t is the part of $\partial\Omega_p$ on which the traction vector may be prescribed. The mechanical boundary conditions are given by Eqs. (2.7)–(2.8). Γ_p^ψ represents the electroded parts of $\partial\Omega_p$, and Γ_p^q represents the unelectroded parts of $\partial\Omega_p$. On Γ_p^ψ, the electrical essential boundary conditions are given by

$$\psi_+ - \psi = 0 \quad \text{on} \quad \Gamma_u^\psi, \tag{2.14}$$

$$\psi_- - \psi = 0 \quad \text{on} \quad \Gamma_l^\psi, \tag{2.15}$$

where ψ_+ and ψ_- are the potential rates at the top and bottom electrodes, respectively. They are spatially constant and vary only with time. On the unelectroded parts, the electrical natural boundary condition is given by Eq. (2.10), where $\bar{q}$ is the free charge density per unit surface area. In this study, we assume the free charge density to be zero on the unelectroded surfaces. The mechanical effects on the electrodes can be neglected because of their relatively small thickness.

The time-dependent potential developed by the harvester due to the strains is given by

$$\dot{\phi} = \psi_+ - \psi_- \quad \text{on} \quad \Gamma_p^\psi, \tag{2.16}$$

where ϕ is the potential developed between the upper and lower electrodes. In energy harvesting applications, one of the electrodes is typically grounded and the other electrode is left open for a floating potential rate to develop. In this example, the lower electrode is grounded by setting the potential rate to zero on Γ_l^ψ, whereupon the electrical essential boundary condition in Eq. (2.15) may be written as

$$\psi_- = \psi = 0 \quad \text{on} \quad \Gamma_l^\psi. \tag{2.17}$$

On the electrodes Γ_u^ψ and Γ_l^ψ, the total free electric charge Q_e is given by

$$Q_e = \int_{\Gamma_u^\psi} q_+ \, \mathrm{d}\Gamma = -\int_{\Gamma_l^\psi} q_- \, \mathrm{d}\Gamma. \tag{2.18}$$

Circuit The electrical circuit constituting a resistive load is described by Ohm's law as

$$\phi - R \cdot I = 0, \tag{2.19}$$

where ϕ is the voltage across the resistor R, and I is the current flowing through the circuit. It is assumed that the voltage across the resistor element is equal to the voltage developed between the electrodes of the piezoelectric layer. This assumption enables a native coupling between the harvesting circuit and the harvester. The current flowing out of the upper electrode (since the potential rate on the lower electrode is set to zero) is given by

$$I = -\dot{Q}_e. \tag{2.20}$$

Substituting Eqs. (2.18) and (2.19) in (2.20), the coupling between the circuit and the electrode can be expressed as

$$\frac{\phi}{R} + \int_{\Gamma_u^\psi} \dot{q}_+ \, \mathrm{d}\Gamma_p. \tag{2.21}$$

2.3.1 Weighted Residual Formulation

The weak formulation of the redefined boundary value problem can now be derived by considering Eq. (2.16) as a constraint to enforce the equipotential condition of the top electrode, and by considering Eq. (2.21) as a constraint to enable the coupling between the circuit and the harvester. Multiplying Eqs. (2.16) and (2.21), respectively, by δq and $\delta\phi$ we additionally obtain

$$+ \int_{\Gamma_u^\psi} \delta q(\dot{\phi} - \psi_+) \, \mathrm{d}\Gamma_p \tag{2.22}$$

$$+ \delta\phi \left(\frac{\phi}{R} + \int_{\Gamma_u^\psi} \dot{q}_+ \, \mathrm{d}\Gamma_p \right). \tag{2.23}$$

Here, ϕ does not vary spatially; hence, the first term in Eq. (2.23) is written outside the integral. Equations (2.22) and (2.23) can be combined with Eq. (2.11) to obtain the single integral form of the piezoelectric layer covered with electrodes and coupled to the circuit:

$$\int_{\Omega_p} \delta\vec{v} \cdot (\rho\dot{\vec{v}} - \vec{f})\, \mathrm{d}\Omega_p + \int_{\Omega_p} \dot{\mathbf{S}}(\delta\vec{v}) : \mathbf{T}\, \mathrm{d}\Omega_p + \int_{\Omega_p} \dot{\vec{E}}(\delta\psi) \cdot \vec{D}\, \mathrm{d}\Omega_p \tag{2.24a}$$

$$+ \sum_e \int_{\Omega_p} \delta\mathbf{T} : ([s^{\vec{D}}]\dot{\mathbf{T}} + [g]^\top \dot{\vec{D}} - \dot{\mathbf{S}}(\vec{v}))\, \mathrm{d}\Omega_p \tag{2.24b}$$

$$+ \sum_e \int_{\Omega_p} \delta\vec{D} \cdot ([g]\dot{\mathbf{T}} + [\varepsilon^{\mathbf{T}}]^{-1}\dot{\vec{D}} - \dot{\vec{E}}(\psi))\, \mathrm{d}\Omega_p - \int_{\Gamma_p^t} \delta\vec{v} \cdot \bar{\vec{t}}\, \mathrm{d}\Gamma_p \tag{2.24c}$$

$$+ \int_{\Gamma_u^\psi} \delta q_+ \dot{\phi}\, \mathrm{d}\Gamma_p + \int_{\Gamma_u^\psi} \delta\phi \dot{q}_+\, \mathrm{d}\Gamma_p \tag{2.24d}$$

$$- \int_{\Gamma_u^\psi} \delta q_+ \psi_+\, \mathrm{d}\Gamma_p - \int_{\Gamma_u^\psi} \delta\psi_+ q_+\, \mathrm{d}\Gamma_p \tag{2.24e}$$

$$+ \delta\phi\frac{\phi}{R} \;=\; 0 \qquad \forall\ \delta\vec{v},\ \delta\psi,\ \delta\phi,\ \delta q,\ \delta\mathbf{T},\ \delta\vec{D}. \tag{2.24f}$$

In Eq. (2.24), second integral in line (e) corresponds to the charges accumulated on the surface due to the piezoelectric effect. Also, $\bar{q} = 0$ on Γ_p^q because no external surface charge densities are prescribed.

Elastic Structure For the linear elastic structure at small deformations and occupying the domain Ω_s, the integral form can be obtained using the same basic principles and is given by

$$\int_{\Omega_s} \delta\vec{v} \cdot (\rho\dot{\vec{v}} - \vec{f})\, \mathrm{d}\Omega_s + \int_{\Omega_s} \dot{\mathbf{S}}(\delta\vec{v}) : \mathbf{T}\, \mathrm{d}\Omega_s \tag{2.25a}$$

$$+ \sum_e \int_{\Omega_s} \delta\mathbf{T} : ([s^{\vec{D}}]\dot{\mathbf{T}} - \dot{\mathbf{S}}(\vec{v}))\, \mathrm{d}\Omega_s \tag{2.25b}$$

$$- \int_{\Gamma_s^t} \delta\vec{v} \cdot \bar{\vec{t}}\, \mathrm{d}\Gamma_s \;=\; 0 \qquad \forall\ \delta\vec{v},\ \delta\mathbf{T}, \tag{2.25c}$$

where Γ_s^t is the part of $\partial\Omega_s$ on which structural natural boundary condition is prescribed. The subscript s denotes the domain of the elastic substructure.

Equations (2.24) and (2.25), together, constitute the monolithic integral form of the coupled piezoelectric energy harvesting problem. The formulation presented in this section can be applied to any piezoelectric harvester configuration with one or several piezoelectric layers. Constitutive laws for viscoelastic and viscoplastic materials can also be used within the mixed formulation established in this section.

Remark 1 It can be noted that the electrical quantities are not present in Eq. (2.25). This is valid only if the elastic structure Ω_s is a conducting material, because both the electric field and the electric displacement will vanish within a conductor. If Ω_s is made of a dielectric material, only the piezoelectric coupling coefficient $[g]$ will vanish, but the electric field will be present [44].

Remark 2 If there are more than one piezoelectric layer attached to Ω_s, and if Ω_s is a conducting material, then all the electrodes glued to Ω_s must be electrically connected in such a way that they share the same potential. If Ω_s is a dielectric material, the electrodes must be located far apart from each other so that the electrical field in Ω_s is of the same order of magnitude than in Ω_p [44].

2.3.2 Finite Element Discretization

The finite element model of the coupled system can be obtained directly from Eqs. (2.24) and (2.25). For the piezoelectric patch, Eqs. (2.7) and (2.9) are satisfied by defining velocities and electric potential rate as nodal d.o.f.s. of the elements discretizing Ω_p. This ensures zeroth-order continuity of the velocities and electric potential rate at the element interface. For the host structure, only velocities are defined as the nodal d.o.f.s of the elements discretizing Ω_s, thereby satisfying Eq. (2.7). There is no continuity requirement on the other two field variables, namely the assumed stresses and dielectric displacements. At the boundary between Ω_s and Ω_p, the nodes of the elements discretizing Ω_s must coincide with the nodes of the elements discretizing Ω_p to couple the two domains. Isoparametric hexahedral elements are employed to discretize Ω_p and Ω_s. Within any element, the geometry and the continuous field variables are interpolated from their nodal values using standard tensor product interpolation functions as

$$\vec{x}^e = \mathbf{N}_x \hat{\vec{x}}^e, \quad \vec{v}^e = \mathbf{N}_v \hat{\vec{v}}^e, \quad \psi^e = \mathbf{N}_\psi \hat{\vec{\psi}}^e, \tag{2.26}$$

where $\hat{\vec{x}}^e, \hat{\vec{v}}^e$ and $\hat{\vec{\psi}}^e$ are the vectors of nodal co-ordinates, nodal velocities and nodal potential rate, respectively. $\mathbf{N}_x$ is the co-ordinate interpolation matrix, $\mathbf{N}_v$ is the velocity interpolation matrix, and $\mathbf{N}_\psi$ is the potential rate interpolation matrix. Because the stress tensor $\mathbf{T}$ and the strain tensor $\mathbf{S}$ are symmetric, they can conveniently be expressed as vectors of six components using *Voigt* notation as $\vec{T} = \{t_{xx},\ t_{yy},\ t_{zz},\ t_{xy},\ t_{xz}\ t_{yz}\}^\top$ and $\vec{S} = \{s_{xx},\ S_{yy},\ S_{zz},\ 2S_{xy},\ 2S_{xz}\ 2S_{yz}\}^\top$, respectively. Substituting Equation (2.26) in Eqs. (2.4) and (2.6), the strain $\vec{S}$ and electric field $\vec{E}$ in the element can be expressed as

$$\vec{S}^e = \mathbf{B}_v \hat{\vec{v}}^e, \quad \vec{E}^e = -\mathbf{B}_\psi \hat{\vec{\psi}}^e, \tag{2.27}$$

where $\mathbf{B}_v$ and $\mathbf{B}_\psi$ are the matrices containing the global spatial derivatives of the velocity shape functions and electric potential rate shape functions, respectively. The assumed stresses and electric displacements are defined only inside the elements, and they are discontinuous at the element edge. The shape functions for the assumed stresses and electric displacements are the same as the functions employed in [48]. Within an element, the shape functions for the assumed stresses and electric displacements are given by

$$\vec{T}^e = \mathbf{N}_t \hat{\vec{T}}^e, \quad \vec{D}^e = \mathbf{N}_d \hat{\vec{\beta}}^e, \tag{2.28}$$

where $\mathbf{N}_t$ is the stress shape function matrix, $\hat{\vec{T}}^e$ is the vector of local stress components, $\mathbf{N}_d$ is the electric displacement shape function matrix, and $\hat{\vec{\beta}}^e$ is the vector of local electric displacement components. For a typical isoparametric hexahedral element with eight nodes, 18 stress components and 7 electric displacement components are needed to secure proper element rank.

At this point, the circuit and the electrodes covering the patch are not accounted for in the finite element formulation. We identify from Eq. (2.17) that only Γ_u^ψ contributes to the floating potential and Γ_l^ψ is grounded. In the finite element model, grounding is achieved by setting the potential rate (ψ) degrees of freedom at the bottom nodes of the elements discretizing Ω_p to zero. Isoparametric surface elements are employed to discretize Γ_u^ψ with electric charge q and electric potential rate ψ as nodal d.o.f.s. Their values inside an element are interpolated from their nodal values as

$$q^e = \mathbf{N}_q \hat{\vec{q}}^e, \quad \psi^e = \mathbf{N}_\psi \hat{\boldsymbol{\psi}}^e, \tag{2.29}$$

where $\mathbf{N}_q$ is the charge interpolation matrix and $\hat{\vec{q}}^e$ is the vector of nodal electric charge. At the piezoelectric layer–electrode boundary, the nodes of the elements discretizing Ω_p and Γ_u^ψ must coincide to couple the electrode and the piezoelectric patch.

It is worth pausing here to evaluate the terms in Eq. (2.24). The integrals in lines (d) and (e) contribute to modeling the equipotential electrode. Because the electrodes are assumed to be perfectly conductive, a single potential difference can be defined across them. The potential rate (ψ) at the nodes of the elements discretizing Γ_u^ψ is coupled to the potential (ϕ) through the electric charge (q). Thus, ϕ is the spatially constant floating potential value across the top electrode. This is modeled by creating a virtual node with electric potential ϕ as the only degree of freedom and coupling it to the elements discretizing Γ_u^ψ. Hence, the shape function $\mathbf{N}_\phi$ for ϕ is I.

The semi-discrete element-level matrix relations are given by

$$\begin{bmatrix} \mathbf{M}_{vv}^e & 0 & 0 & 0 & 0 & 0 \\ 0 & 0 & 0 & 0 & 0 & 0 \\ 0 & 0 & 0 & \mathbf{F}_{q\phi}^e & 0 & 0 \\ 0 & 0 & \mathbf{F}_{\phi q}^e & 0 & 0 & 0 \\ 0 & 0 & 0 & 0 & \mathbf{F}_{tt}^e & \mathbf{F}_{td}^e \\ 0 & 0 & 0 & 0 & \mathbf{F}_{dt}^e & \mathbf{F}_{dd}^e \end{bmatrix} \begin{Bmatrix} \dot{\hat{\vec{v}}}^e \\ \dot{\hat{\vec{\psi}}}^e \\ \dot{\hat{\vec{q}}}^e \\ \dot{\hat{\phi}} \\ \dot{\hat{\vec{T}}}^e \\ \dot{\hat{\vec{\beta}}}^e \end{Bmatrix} + \begin{bmatrix} 0 & 0 & 0 & 0 & \mathbf{K}_{vt}^e & 0 \\ 0 & 0 & \mathbf{K}_{\psi q}^e & 0 & 0 & \mathbf{K}_{\psi d}^e \\ 0 & \mathbf{K}_{q\psi}^e & 0 & 0 & 0 & 0 \\ 0 & 0 & 0 & \mathbf{K}_{\phi\phi} & 0 & 0 \\ \mathbf{K}_{tv}^e & 0 & 0 & 0 & 0 & 0 \\ 0 & \mathbf{K}_{d\psi}^e & 0 & 0 & 0 & 0 \end{bmatrix} \begin{Bmatrix} \hat{\vec{v}}^e \\ \hat{\vec{\psi}}^e \\ \hat{\vec{q}}^e \\ \hat{\phi} \\ \hat{\vec{T}}^e \\ \hat{\vec{\beta}}^e \end{Bmatrix} = \begin{Bmatrix} \hat{\vec{f}}^e \\ \vec{0} \\ \vec{0} \\ \vec{0} \\ \vec{0} \\ \vec{0} \end{Bmatrix}, \tag{2.30}$$

where the entries in the matrices are given by

$$\mathbf{M}_{vv}^e = \rho \int_\Omega \mathbf{N}_v^\top \mathbf{N}_v \ \mathrm{d}\Omega, \quad \mathbf{F}_{q\phi}^e = {\mathbf{F}_{q\phi}^e}^\top = \int_\Omega \mathbf{N}_q^\top \mathbf{N}_\phi \ \mathrm{d}\Omega, \tag{2.31a}$$

$$\mathbf{F}_{td}^e = {\mathbf{F}_{td}^e}^\top = \int_\Omega \mathbf{N}_t^\top [g]^\top \mathbf{N}_d \ \mathrm{d}\Omega, \quad \mathbf{F}_{tt}^e = \int_\Omega \mathbf{N}_t^\top [s^{\vec{D}}] \mathbf{N}_t \ \mathrm{d}\Omega, \tag{2.31b}$$

$$\mathbf{F}_{dd}^e = \int_\Omega \mathbf{N}_d^\top [\varepsilon^{\mathbf{T}}] \mathbf{N}_d \ \mathrm{d}\Omega, \quad \mathbf{K}_{vt}^e = -{\mathbf{K}_{vt}^e}^\top = \int_\Omega \mathbf{B}_v^\top \mathbf{N}_t \ \mathrm{d}\Omega, \tag{2.31c}$$

$$\mathbf{K}_{\psi d}^e = -{\mathbf{K}_{\psi D}^e}^\top = \int_\Omega \mathbf{B}_\psi^\top \mathbf{N}_d \ \mathrm{d}\Omega, \quad \mathbf{K}_{\psi q}^e = {\mathbf{K}_{\psi q}^e}^\top = \int_\Omega \mathbf{N}_\psi^\top \mathbf{N}_q \ \mathrm{d}\Omega, \tag{2.31d}$$

$$\mathbf{K}_{\phi\phi} = \mathbf{N}_\phi^\top \frac{1}{R} \mathbf{N}_\phi. \tag{2.31e}$$

The assumed stresses and electrical displacements, as mentioned earlier, are not continuous and can be condensed on the element level. The global finite element equations are achieved by adding the contributions from each element of the finite element mesh. This leads to a mixed-hybrid formulation of the coupled problem. The dynamic condensation of the stresses and electrical displacements is explained in the following section.

2.3.3 Dynamic Condensation and Frequency Domain Analysis

This subsection deals with the dynamic condensation of the internal degrees of freedom, and the determination of eigenfrequencies and eigenmodes for the setup shown in Fig. 2.1. Equation (2.30) for the homogeneous problem may be written as

$$\begin{bmatrix} \mathbf{M}^e_{vv} & 0 & 0 & 0 & 0 & 0 \\ 0 & 0 & 0 & 0 & 0 & 0 \\ 0 & 0 & 0 & \mathbf{F}^e_{q\phi} & 0 & 0 \\ 0 & 0 & \mathbf{F}^e_{\phi q} & 0 & 0 & 0 \\ 0 & 0 & 0 & 0 & \mathbf{F}^e_{tt} & \mathbf{F}^e_{td} \\ 0 & 0 & 0 & 0 & \mathbf{F}^e_{dt} & \mathbf{F}^e_{dd} \end{bmatrix} \begin{Bmatrix} \dot{\hat{\vec{v}}}^e \\ \dot{\hat{\vec{\psi}}}^e \\ \dot{\hat{\vec{q}}}^e \\ \dot{\hat{\phi}} \\ \dot{\hat{\vec{T}}}^e \\ \dot{\hat{\vec{\beta}}}^e \end{Bmatrix} + \begin{bmatrix} 0 & 0 & 0 & 0 & \mathbf{K}^e_{vt} & 0 \\ 0 & 0 & \mathbf{K}^e_{\psi q} & 0 & 0 & \mathbf{K}^e_{\psi d} \\ 0 & \mathbf{K}^e_{q\psi} & 0 & 0 & 0 & 0 \\ 0 & 0 & 0 & \mathbf{K}_{\phi\phi} & 0 & 0 \\ \mathbf{K}^e_{tv} & 0 & 0 & 0 & 0 & 0 \\ 0 & \mathbf{K}^e_{d\psi} & 0 & 0 & 0 & 0 \end{bmatrix} \begin{Bmatrix} \hat{\vec{v}}^e \\ \hat{\vec{\psi}}^e \\ \hat{\vec{q}}^e \\ \hat{\phi} \\ \hat{\vec{T}}^e \\ \hat{\vec{\beta}}^e \end{Bmatrix} = \vec{0}. \tag{2.32}$$

In order to obtain the global matrix equations and frequency response functions of the problem, we seek the solutions of the form

$$\hat{\vec{v}}(t) = \tilde{\vec{v}} \cdot e^{\lambda t}, \quad \hat{\vec{\psi}}(t) = \tilde{\vec{\psi}} \cdot e^{\lambda t}, \quad \hat{\phi}(t) = \tilde{\vec{\phi}} \cdot e^{\lambda t}, \tag{2.33a}$$

$$\hat{\vec{q}}(t) = \tilde{\vec{q}} \cdot e^{\lambda t}, \quad \hat{\vec{T}}(t) = \tilde{\vec{t}} \cdot e^{\lambda t}, \quad \hat{\vec{\beta}}(t) = \tilde{\vec{\beta}} \cdot e^{\lambda t}, \tag{2.33b}$$

and thus

$$\dot{\hat{\vec{v}}}(t) = \lambda \tilde{\vec{v}} \cdot e^{\lambda t}, \quad \dot{\hat{\vec{\psi}}}(t) = \lambda \tilde{\vec{\psi}} \cdot e^{\lambda t}, \quad \dot{\hat{\phi}}(t) = \lambda \tilde{\vec{\phi}} \cdot e^{\lambda t}, \tag{2.34a}$$

$$\dot{\hat{\vec{q}}}(t) = \lambda \tilde{\vec{q}} \cdot e^{\lambda t}, \quad \dot{\hat{\vec{T}}}(t) = \lambda \tilde{\vec{t}} \cdot e^{\lambda t}, \quad \dot{\hat{\vec{\beta}}}(t) = \lambda \tilde{\vec{\beta}} \cdot e^{\lambda t}, \tag{2.34b}$$

where λ is the eigenvalue, and t is the time. The assumed stresses and electric displacements in Eq. (2.32) need to be condensed before obtaining the global matrix equations. The finite element mesh for the entire setup is comprised of different element types, and it can be seen that the elemental matrices in Eq. (2.32) comprises the contribution of each of the element types. However, only the elements discretizing Ω_s and Ω_p contain internal d.o.f.s.

Elastic Structure The element-level matrix equation for the *structural elements* discretizing Ω_s is given by

$$\begin{bmatrix} \mathbf{M}^e_{vv} & 0 \\ 0 & \mathbf{F}^e_{tt} \end{bmatrix} \begin{Bmatrix} \dot{\hat{\vec{v}}}^e \\ \dot{\hat{\vec{T}}}^e \end{Bmatrix} + \begin{bmatrix} 0 & \mathbf{K}^e_{vt} \\ \mathbf{K}^e_{tv} & 0 \end{bmatrix} \begin{Bmatrix} \hat{\vec{v}}^e \\ \hat{\vec{T}}^e \end{Bmatrix} = \vec{0}. \tag{2.35}$$

Substituting Eq. (2.34) in (2.35), we obtain

$$\begin{bmatrix} \lambda \mathbf{M}^e_{vv} & \mathbf{K}^e_{vt} \\ \mathbf{K}^e_{tv} & \lambda \mathbf{F}^e_{tt} \end{bmatrix} \begin{Bmatrix} \tilde{\vec{v}}^e \\ \tilde{\vec{T}}^e \end{Bmatrix} = \vec{0}. \tag{2.36}$$

Employing dynamic condensation to eliminate the assumed stresses in Eq. (2.36) yields the condensed element matrix equation

$$\left[\lambda \mathbf{M}^e_{vv} - \frac{1}{\lambda} \mathbf{G}^{*e} \right] \tilde{\vec{v}}^e = \vec{0}, \quad \mathbf{G}^{*e} = \mathbf{K}^e_{vt} {\mathbf{F}^e_{tt}}^{-1} \mathbf{K}^e_{tv}, \tag{2.37}$$

where $\mathbf{G}^{*e}$ is the element-level hybridized stiffness matrix.

Piezo Elements Similar to Eq. (2.35), the element-level matrix equation for the *piezo elements* discretizing Ω_p, after considering Eq. (2.34), is given by

$$\begin{bmatrix} \lambda \mathbf{M}^e_{vv} & 0 & \mathbf{K}^e_{vt} & 0 \\ 0 & 0 & 0 & \mathbf{K}^e_{\psi d} \\ \mathbf{K}^e_{tv} & 0 & \lambda \mathbf{F}^e_{tt} & \lambda \mathbf{F}^e_{td} \\ 0 & \mathbf{K}^e_{d\psi} & \lambda \mathbf{F}^e_{dt} & \lambda \mathbf{F}^e_{dd} \end{bmatrix} \begin{Bmatrix} \tilde{\vec{v}}^e \\ \tilde{\vec{\psi}}^e \\ \tilde{\vec{T}}^e \\ \tilde{\vec{\beta}}^e \end{Bmatrix} = \vec{0}. \tag{2.38}$$

The assumed stresses and electrical displacements are eliminated using the same procedure, and the condensed element matrix equation for the elements discretizing Ω_p is given by

$$\left[\lambda \begin{bmatrix} \mathbf{M}^e_{vv} & 0 \\ 0 & 0 \end{bmatrix} - \frac{1}{\lambda} \mathbf{G}^{*e} \right] \begin{Bmatrix} \tilde{\vec{v}}^e \\ \tilde{\vec{\psi}}^e \end{Bmatrix} = \vec{0}, \tag{2.39}$$

where the hybridized stiffness matrix $\mathbf{G}^{*e}$ is given by

$$\mathbf{G}^{*e} = \begin{bmatrix} \mathbf{K}^e_{vt} & 0 \\ 0 & \mathbf{K}^e_{\psi d} \end{bmatrix} \begin{bmatrix} \mathbf{F}^e_{tt} & \mathbf{F}^e_{td} \\ \mathbf{F}^e_{dt} & \mathbf{F}^e_{dd} \end{bmatrix}^{-1} \begin{bmatrix} \mathbf{K}^e_{tv} & 0 \\ 0 & \mathbf{K}^e_{d\psi} \end{bmatrix} \tag{2.40}$$

Thus, the global matrix equations for the entire mesh is obtained by adding the contributions from each element of all the element types (structural, piezo, surface elements and the virtual node) and can be expressed as

$$\left[\lambda \mathbf{M} + \mathbf{C} - \frac{1}{\lambda} \mathbf{H} \right] \tilde{\vec{\alpha}} = \vec{0}, \tag{2.41}$$

where

$$\mathbf{M} = \begin{bmatrix} \mathbf{M}_{vv} & 0 & 0 & 0 \\ 0 & 0 & 0 & 0 \\ 0 & 0 & 0 & \mathbf{F}_{q\phi} \\ 0 & 0 & \mathbf{F}_{\phi q} & 0 \end{bmatrix}, \quad \mathbf{C} = \begin{bmatrix} 0 & 0 & 0 & 0 \\ 0 & 0 & \mathbf{K}_{\psi q} & 0 \\ 0 & \mathbf{K}_{q\psi} & 0 & 0 \\ 0 & 0 & 0 & \mathbf{K}_{\phi\phi} \end{bmatrix}, \quad \tilde{\vec{\alpha}} = \begin{Bmatrix} \tilde{\vec{v}} \\ \tilde{\vec{\psi}} \\ \tilde{\vec{q}} \\ \tilde{\vec{\phi}} \end{Bmatrix}, \tag{2.42a}$$

$$\mathbf{H} = \begin{bmatrix} \boxed{\mathbf{G}^*} & \begin{matrix} 0 & 0 \\ 0 & 0 \end{matrix} \\ \begin{matrix} 0 & 0 \\ 0 & 0 \end{matrix} & \begin{matrix} 0 & 0 \\ 0 & 0 \end{matrix} \end{bmatrix}, \tag{2.42b}$$

where $\mathbf{G}^*$ is obtained after assembly of element-level matrix contributions. It can be observed that the foregoing homogeneous, coupled Eq. (2.41) resembles a rational eigenvalue problem, and the eigenvalues and eigenvectors are obtained by transforming Eq. (2.41) into a first-order system. It is important to understand the nature of the matrices in the coupled equation. Matrix $\mathbf{M}$ can be interpreted as the mass matrix (without abuse of the term) to the extent that the inertial term $\mathbf{M}_{vv}$ is present, and $\mathbf{H}$ is the hybridized stiffness matrix. $\mathbf{C}$ can be interpreted as the damping matrix. It is obvious that any type of harvesting circuit attached to the piezoelectric layer will cause energy dissipation in the system; hence, it is not surprising that $\mathbf{K}_{\phi\phi}$ should find its place in the damping matrix. Thus, the eigenvalues ($\lambda_r = -\delta_r \pm i\omega_r$) are obtained as complex conjugate pairs with real and imaginary part. The eigenfrequency for a mode r is calculated from the imaginary part as $\omega_r = \Im(\lambda_r)$.

For a piezoelectric layer not connected to any circuit, the two possible configurations (boundary conditions) are the short-circuit and open-circuit configurations. Short-circuit condition is characterized by zero potential difference between the electrodes covering the patches. Open-circuit condition is characterized by floating potential on the electrodes, and the total charge remains zero. In our formulation, these two limit boundary conditions are accommodated by assuming a very low resistance for the short-circuit case, and a high resistance for the open-circuit case. One of the main advantages of the formulation is that, because the electrical circuit is fully incorporated in the monolithic formulation, eigenvalues and eigenmodes can be obtained not just for the short-circuit and open-circuit conditions but also for any finite value of resistance.

Structural Damping At this point, it is pertinent to mention the incorporation of damping inherent in real structures. Structural damping of a desired mode is accomplished using mass-proportional damping and expressed as

$$\tilde{\mathbf{D}}_{vv} = \gamma_r \mathbf{M}_{vv}, \tag{2.43}$$

where γ_r is the modal mass-proportional damping coefficient calculated from experimentally obtained modal damping ratio (ζ_r) using the formula

$$\gamma_r = 2\zeta_r \omega_r, \tag{2.44}$$

where ω_r is the natural frequency of the mode considered. $\tilde{\mathbf{D}}_{vv}$ is subsequently incorporated in the damping matrix given in Eq. (2.41) as

$$\mathbf{C} = \begin{bmatrix} \tilde{\mathbf{D}}_{vv} & 0 & 0 & 0 \\ 0 & 0 & \mathbf{K}_{\psi q} & 0 \\ 0 & \mathbf{K}_{q\psi} & 0 & 0 \\ 0 & 0 & 0 & \mathbf{K}_{\phi\phi} \end{bmatrix}. \tag{2.45}$$

Equation (2.45) represents the damping matrix which accounts for the damping effect due to the attached circuit, and the damping inherent to the structure. This damping formulation can be extended to include strain rate damping as well.

2.4 Numerical Example and Validation

The aim of this section is to validate the model proposed in Sect. 2.3 by comparing the results from the model with results proposed by Erturk and Inman [36] for a piezoelectric bimorph cantilever with series and parallel configurations of the piezoelectric layers. The steady-state electromechanical frequency response functions (FRFs) obtained from the simulations—relating the voltage, power and tip velocity outputs to base acceleration—are compared with the FRFs given in [36]. All the comparisons pertain only to the first bending mode of the harvester.

2.4.1 Configuration and Modeling of the Bimorph Harvester: Series Configuration

The modeled geometry (see Fig. 2.2(a)) is a composite cantilever beam with a tip mass where a brass substructure is sandwiched between two identical piezoceramic layers. In the series configuration, the piezoceramic layers are poled in opposite directions. The electrodes covering the top and bottom piezoceramic layers constitute the output terminals of the harvester. As an energy harvesting device, the cantilever structure is subjected to base excitations at the fixed end of the cantilever. The geometric and material parameters of the harvester are given in Table 2.1

We now apply the concepts established in Sect. 2.3 to the setup shown in Fig. 2.2(a). In Table 2.1, the permittivity $\varepsilon_{33}^{\mathbf{S}}$ ($\varepsilon_0 = 8.854$ pFm^{-1}) is the measure at constant strain, and the piezoelectric

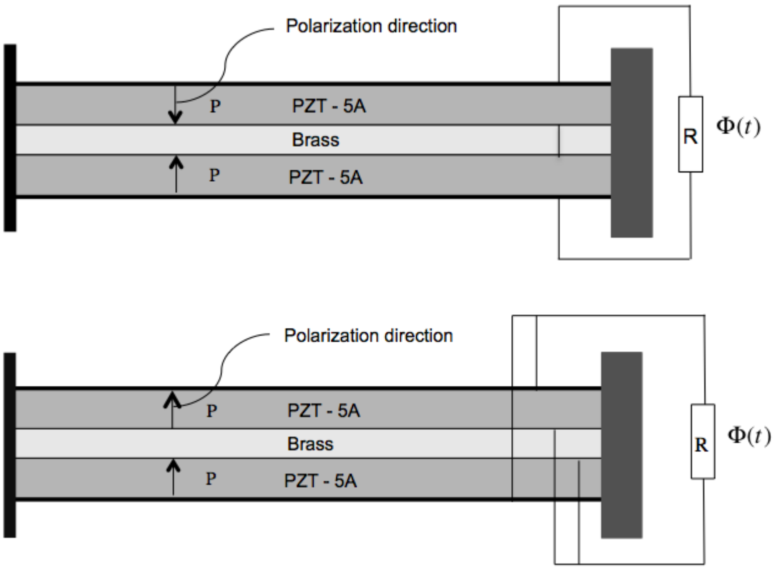

Figure 2.2: Bimorph piezoelectric energy harvester; **a** series connection; **b** parallel connection

coupling coefficient d_{31} is the measure used in strain-charge form of the piezoelectric constitutive equation. However, in Eqs. (2.1) and (2.2), the permittivity $\varepsilon^{\mathbf{T}}$ is a measure at constant stress, and $[g]$ is the piezoelectric coupling matrix in strain-voltage form. Hence, the following relations

$$[\varepsilon^{\mathbf{T}}] = [\varepsilon^{\mathbf{S}}] + [d][c^{\vec{E}}][d]^{\top}, \tag{2.46}$$

$$[\varepsilon^{\mathbf{T}}]^{-1} = ([\varepsilon^{\mathbf{S}}] + [d][c^{\vec{E}}][d]^{\top})^{-1}. \tag{2.47}$$

are used to transform the values in the table to fit the formulation given in (2.1) and (2.2), where $[c^{\vec{E}}]$ is the Young's modulus Y_p of the piezoelectric material measured at constant electric field as given in Table 2.1. The compliance matrix at constant dielectric displacement is obtained from the table values as follows

$$[s^{\vec{D}}] = [c^{\vec{E}}]^{-1} - ([d]^{\top}[\varepsilon^{\mathbf{T}}]^{-1}[d]), \tag{2.48}$$

and the piezoelectric voltage coefficient derived from displacement coefficient is given by

$$[g] = [\varepsilon^{\mathbf{T}}]^{-1}[d]. \tag{2.49}$$

The discretization of the setup in Fig. 2.2(a) follows the same procedure as in Sect. 2.3. The brass layer is discretized by isoparametric hexahedral elements with velocity components as nodal d.o.f.s., and the piezoceramic layers are discretized by isoparametric hexahedral elements with velocity and electric potential rate as nodal d.o.f.s. The electrodes are discretized by surface elements, and the virtual node enables the coupling of the circuit to the bimorph harvester. In the finite element formulation, polarization direction of the piezoceramic layers is represented by the sign of the piezoelectric coefficient $[g]$. For realizing series connection in the finite element formulation, the sign of $[g]$ in the bottom layer is opposite to that of the top layer so that the direction of the instantaneous electric field is the same in both the layers. To realize the electrical boundary conditions for the series connection, the potential rate (ψ) d.o.f.s at the nodes of the elements discretizing the bottom electrodes are grounded, and the top electrode is connected to the electrical circuit. As mentioned in Sect. 2.3.1, the potential rate value at the top interface between the piezoceramic layer and the brass substructure must be equal to the potential

Table 2.1: Geometric and material properties of the energy harvester

Quantity	Dimension	Value
Length of the beam	L (mm)	50.8
Width of the beam	b (mm)	31.8
Thickness of the piezo. patch (PZT-5A)	h_p (mm)	0.26 (each)
Thickness of the substructure	h_s (mm)	0.14
Young's modulus of the substructure (brass)	Y_s (G Pa)	105
Young's modulus of PZT-5A	Y_p (G Pa)	66
Mass density of the substructure (brass)	ρ_s $\left(\mathrm{kg\,m^{-3}}\right)$	9000
Mass density of PZT-5A	ρ_p $\left(\mathrm{kg\,m^{-3}}\right)$	7800
Piezoelectric displacement coefficient	d_{31} $\left(\mathrm{p\,m\,V^{-1}}\right)$	−190
Permittivity	$\varepsilon_{33}^{\mathbf{S}}$ $\left(\mathrm{F\,m^{-1}}\right)$	$1500\,\varepsilon_0$
Modal damping coefficient	γ_r $\left(\mathrm{rad\ ms^{-1}}\right)$	0.0156
Tip mass	M_t (g)	12

rate value at the bottom interface between the piezoceramic layer and the substructure. This ensures the absence of electrical field inside the brass substructure. This condition is realized by enforcing this equality condition by Lagrange multipliers.

It should be added that in base excitation of the bimorph cantilever, in the absence of other external forces, the effective force on the cantilever is due to its inertia. To simulate this scenario, periodic excitation (a cosine or a sine function) is imposed on the transverse velocity d.o.f.s ($\tilde{\vec{v}}_y$) on the fixed end of the bimorph cantilever. The forcing term is given by

$$\tilde{\vec{f}} = (\tilde{\vec{p}} - i\tilde{\vec{q}})e^{\lambda t}. \tag{2.50}$$

For obtaining the various FRFs, these d.o.f.s are taken to the right-hand side of the Eq. (2.41) and expressed as

$$\left[\lambda\mathbf{M} + \mathbf{C} - \frac{1}{\lambda}\mathbf{H}\right]\tilde{\vec{\alpha}} = (\tilde{\vec{p}} - i\tilde{\vec{q}}), \tag{2.51}$$

where the complex amplitude $\tilde{\vec{\alpha}}$ is computed by solving the associated system of equations.

$$\tilde{\vec{\alpha}} = \left[\lambda\mathbf{M} + \mathbf{C} - \frac{1}{\lambda}\mathbf{H}\right]^{-1}(\tilde{\vec{p}} - i\tilde{\vec{q}}). \tag{2.52}$$

In the example considered in this section, the base velocity is sinusoidal in nature and given by

$$\left[\lambda\mathbf{M} + \mathbf{C} - \frac{1}{\lambda}\mathbf{H}\right]\tilde{\vec{\alpha}} = (\vec{0} - i\tilde{\vec{q}}). \tag{2.53}$$

In Eq. (2.53) $\tilde{\vec{q}}$ is a vector with nonzero entries that correspond to the mechanical Dirichlet nodes with $\frac{g}{\omega}$ as the prescribed base velocity, where $g = 9.81$ ms^{-2} is the acceleration due to gravity and ω is the excitation frequency.

Figure 2.3(a) compares the simulated voltage FRF with the FRF obtained analytically [36] for three different values of load resistance: 1, 33, and 470 kΩ. Here, 1 kΩ resistive load is very close to the short-circuit condition ($R \to 0$) for the depicted energy harvester, and 470 kΩ resistive load is close to the open-circuit condition ($R \to \infty$) for the depicted energy harvester. It can be observed that the voltage increases monotonically with the increase in the value of load resistance. The numerical model predicts an increase in maximum voltage output from 1.56 V at short-circuit condition to 92.3 V at open-circuit condition. As the resistance increases, there is also a shift in the resonance frequency from 46.2 Hz at short-circuit condition to 48.5 Hz at open-circuit condition. The analytical model predicts the short-circuit and open-circuit resonance frequencies to be 45.7 Hz and 48.2 Hz respectively. It should be pointed out that the analytical model is a distributed parameter formulation based on Euler–Bernoulli beam theory and valid for thin piezoelectric harvester. The resonance frequency (in the analytical model) at short-circuit condition is obtained from electrically uncoupled equation (assuming $R = 0$), and the resonance frequency for any finite value of resistance is obtained from the voltage or vibration FRF. In the numerical model, however, the resonance frequency for any finite value of resistance can be obtained by solving the rational eigenvalue problem given in Eq. (2.41).

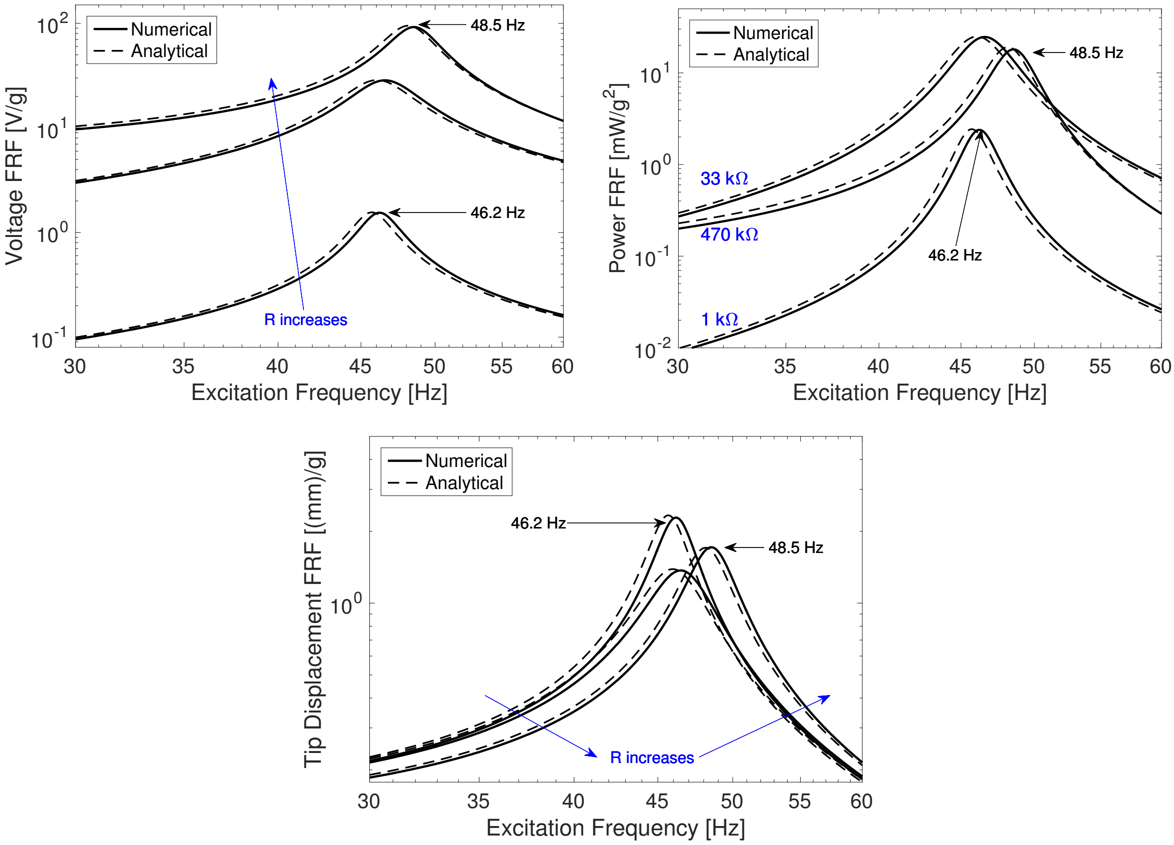

Figure 2.3: Comparison of numerical and analytical FRFs for three different values of load resistance–series connection; **a** voltage FRF, **b** power FRF and **c** tip displacement FRF

Figure 2.3(b) compares the simulated and analytical power FRFs for the same three resistive loads. From the power output FRF, it can be observed that the power neither increases nor decreases monotonically with changing resistive loads, but the FRFs of different values of resistance intersect with each other. The variation of tip displacement for changing load resistance is shown in Fig. 2.3(c). The tip displacement is damped with changing load resistance for excitation at the short-circuit frequency but increases in magnitude with changing load resistance for excitation at the open-circuit frequency. This behavior is more complex than simple viscous damping. If the harvester is excited at open-circuit frequency (48.5 Hz), both the voltage output and the tip displacement will increase with increasing values of resistance.

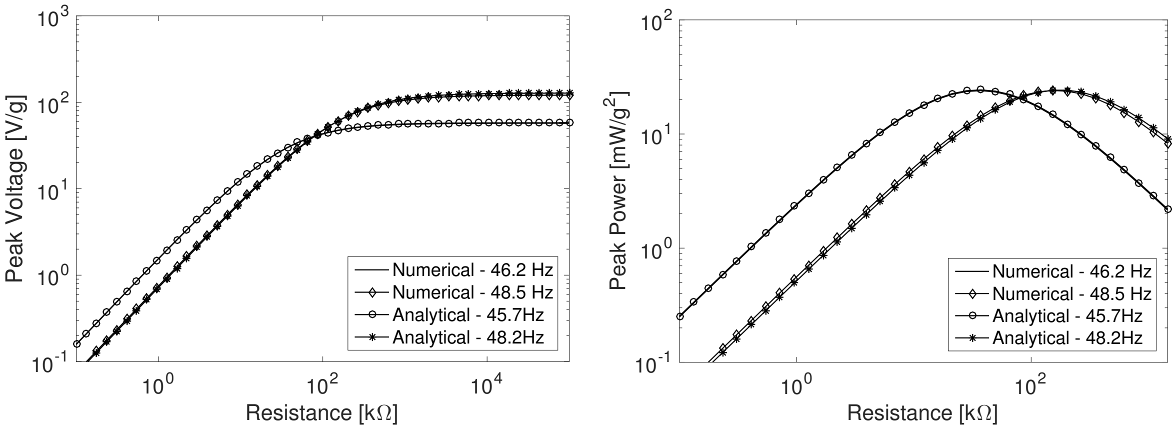

Figure 2.4: **a** Variation of peak voltage for excitation at short- and open-circuit conditions with changing load resistance and **b** variation of peak power for excitation at short- and open-circuit conditions with changing load resistance

It is easier to identify the *optimum resistive load* that gives the maximum power output for a given frequency if the frequency of excitation is kept constant and power output is plotted for changing values of load resistance. Figure 2.4(a) depicts the variation of voltage output with change in load resistance for excitations at short- and open-circuit frequencies. The voltage increases monotonically with change in load resistance in both the cases. In the limit $R \to \infty$, the maximum voltage is 57.3 V/g when excited at 46.2 Hz and 120.8 V/g when excited at 48.5 Hz. For a load resistance of 76 kΩ, the voltage output in both the cases is 40 V/g. Figure 2.4(b) shows the variation of power output with changing load resistance for excitations at short- and open-circuit frequencies. The maximum power output in both the cases is 23.9 mW/g^2. Thus, the optimum load for excitation at the short-circuit frequency is 37.3 kΩ, and the optimum load is 153 kΩ for excitation at the open-circuit frequency. It can be observed from the figures that the numerical results are in very good agreement with the data from the analytical model. As mentioned earlier, the analytical model is a simplified mathematical model based on Euler–Bernoulli beam theory and the numerical results are based on finite element approximation; hence, there is bound to be a slight difference in the natural frequencies predicted by these two distinctly different models.

2.4.2 Configuration and Modeling of the Bimorph Harvester: Parallel Configuration

The modeled geometry (see Fig. 2.2(b)) is very similar to the series configuration setup. In parallel configuration, the piezoceramic layers are poled in the same direction. The top and bottom electrodes constitute one end of the harvester terminal, and the electrodes at the piezoceramic–brass interfaces constitute the other end of the harvester terminal. The geometric and material properties are the same as the properties considered for the series configuration (Table 2.1).

The only difference in the numerical model between the series and parallel configuration is in the way the electrical boundary conditions are realized. To realize the electrical boundary conditions for the parallel configuration, the potential rate (ψ) d.o.f.s at the top and bottom piezoceramic–brass interface nodes are set to zero. The outside electrodes constitute the other end of the terminal and are connected to the circuit. There is no change in the mechanical boundary conditions when compared to the series

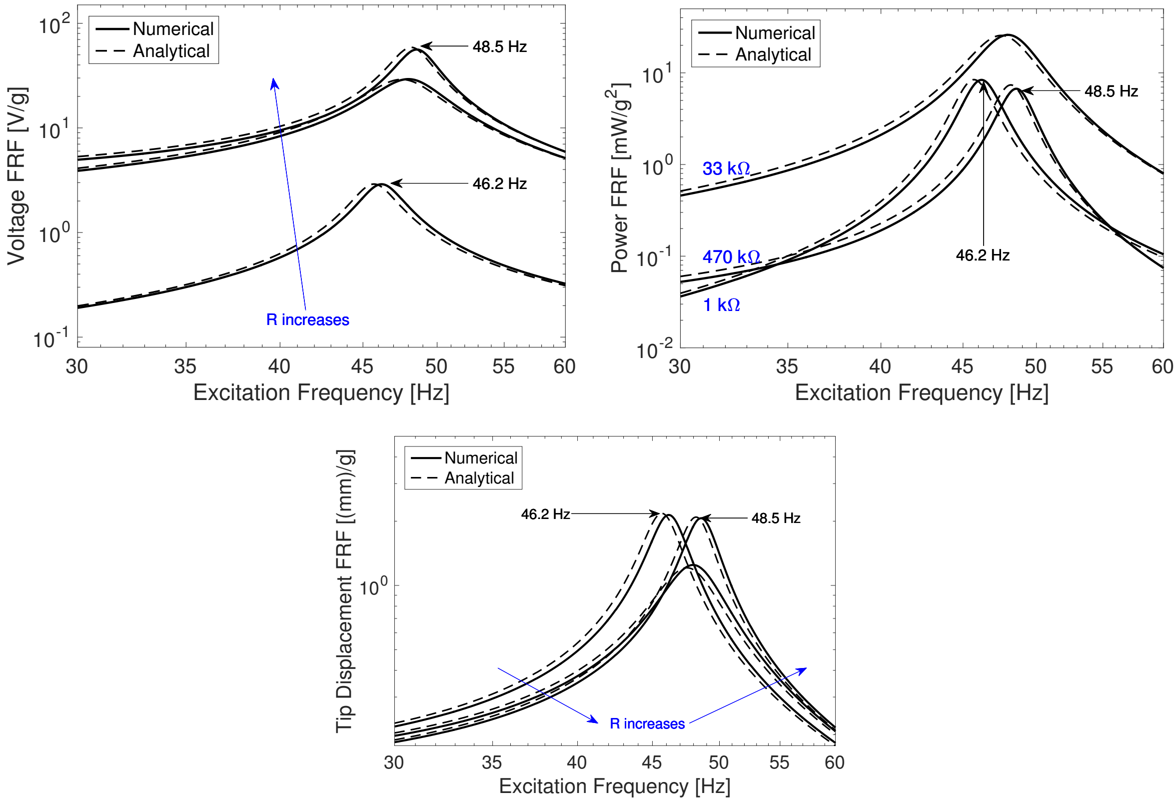

Figure 2.5: Comparison of numerical and analytical FRFs for three different values of load resistance–parallel connection; **a** voltage FRF, **b** power FRF and **c** tip displacement FRF

configuration. The mechanical damping ratio is kept unchanged, and the harvester is tested for the same three values of load resistance considered for the series configuration. Figure 2.5 depicts the voltage, power and tip displacement FRFs for the three resistive loads. The short-circuit and open-circuit frequencies for the parallel configuration are identical to the series configuration. However, for a finite value of load resistance, the effect of the circuit on the harvester in parallel configuration is different than the effect in series configuration. Once again, the results from the numerical model are in good agreement with the results from the analytical model.

Figure 2.6 shows the comparisons of the series and parallel configurations for excitation at the short-circuit frequency. In both configurations, the maximum power outputs at the short-circuit frequency are identical but for different values of optimum load. Figure 2.6(b) shows that a maximum power output of 24 mW/g^2 is harvested for a resistive load of 9.1 kΩ in the parallel configuration, whereas the same power output is harvested for a resistive load of 37.27 kΩ in the series configuration. In the parallel configuration, the power output is achieved with a current amplitude of 1.64 mA/g and a voltage amplitude of 14.9 V/g, whereas in the series configuration, the power output is achieved with a current amplitude of 0.8 mA/g and a voltage amplitude of 30 V/g. The voltage output in series configuration is approximately twice the voltage output in parallel configuration, and the current output in series configuration is approximately half the current output in parallel configuration. The overall power output remains the same in both the configurations.

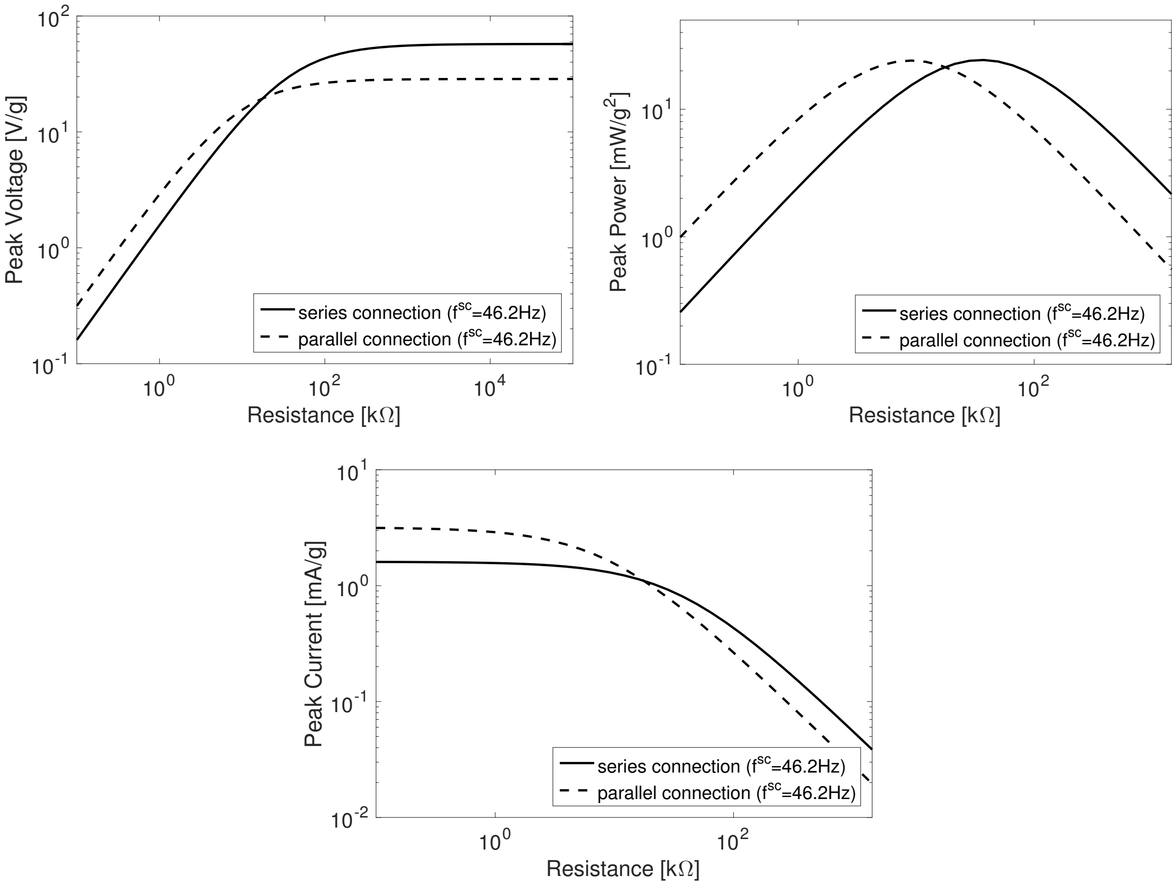

Figure 2.6: Comparison between series and parallel configurations for excitations at the short-circuit resonance frequency; **a** voltage versus resistance, **b** peak power versus resistance and **c** current versus resistance

2.5 Conclusions

A monolithic, mixed-hybrid finite element model is proposed to study piezoelectric EHDs. The formulation is applied to study a bimorph cantilever piezoelectric EHD for both series and parallel configuration of the piezoelectric layers. The strong form of the equations are converted into a monolithic integral form with six unknown fields, and the element leved fields are eliminated by dynamic condensation. The resulting rational eigenvalue problem is then solved to obtain the eigenvalues of the harvester connected to a resistive load. The various frequency response functions obtained from the finite element formulation are compared to the results reported in the literature. The originilatiy of the formulation is in the natural inclusion of equipotential condition for the electrodes and inclusion of the resistive load in the coupled equation. The formulation enables accurate computation of the eigenvalues of an harvester for any finite resistive load. The formulation can also be extended to include fluid domain to study flow-driven energy harvesters.

Chapter 3

Time and Frequency Domain Analysis of Piezoelectric Energy Harvesters

---

Abstract

The successful design of piezoelectric energy harvesting devices relies upon the identification of optimal geometrical and material configurations in order to maximize the power output for a specific band of excitation frequencies. Extendable predictive models and associated approximate solution methods are essential for analysis of a wide variety of future advanced energy harvesting devices involving more complex geometries and material distributions. Based on a holistic continuum mechanics modeling approach to the multi-physics energy harvesting problem, this chapter proposes a monolithic numerical solution scheme utilizing a mixed-hybrid 3D finite element formulation of the coupled governing equations for analysis in time and frequency domain. The weak form of the electromechanics/circuit-system uses velocities and potential rate within the piezoelectric structure, free boundary charge on the electrodes and potential at the level of the generic electric circuit as global degrees of freedom. The approximation of stress and dielectric displacement follows the work by Pian, Sze and Pan. Results obtained with the proposed model are compared with analytical results for the reduced-order model of a cantilevered bimorph harvester with tip mass reported in the literature. The flexibility of the method is demonstrated by studying the influence of partial electrode coverage on the generated power output.

3.1 Introduction

Piezoelectric materials exhibit two kinds of electromechanical coupling effects namely direct and inverse piezoelectric effects. The direct effect is characterized by the accumulation of electric charge in certain crystalline materials with no inversion symmetry as a response to mechanical strains and the inverse effect by the change in the materials' dimension as a response to applied electrical potential. These effects make piezoelectric materials indispensable for many applications including energy harvesting, low power sensors, actuators, transducers, and damping of structural vibrations. Research interest in energy harvesting from ambient vibrations has been growing significantly in the past few years owing to the recent advances in wireless technology and microelectromechanical systems. There are different mechanisms available to convert ambient vibration energy into electrical energy like electromagnetic, electrostatic, and piezoelectric transductions. Of all these methods, energy harvesting by piezoelectric transduction has received the most attention due to high power densities of piezoelectric materials, smaller size, and relative ease with which they can be designed [12]. A detailed review on various forms of piezoelectric energy harvesting can be found in [1, 11, 12].

Many piezoelectric energy harvesting devices (EHDs) are manufactured as thin films, typically as cantilevered beams with one or more layers of piezoelectric patches that are coupled to an electrical circuit. The circuitry for implementing piezoelectric energy harvesting for practical applications may include different components like a rectifier to convert alternating current from the harvester to direct current, a capacitor to store the energy harvested, or a simple resistive electrical load to predict the power output of a piezoelectric EHD. The electromechanical behavior of thin cantilevered piezoelectric EHDs connected to a resistive load has been extensively studied using a variety of analytical modeling approaches (for instance, see [32, 33, 35, 36, 61]). From a modeling perspective, thin cantilevered harvesters easily lend themselves to closed form solution. Erturk and Inman [35] presented a distributed modeling approach based on Euler–Bernoulli beam assumptions and provided significant insight into the coupled aspects of piezoelectric energy harvesting problem. They also addressed the inaccuracies of single degree of freedom (SDOF) modeling approaches. However, analytical models for complex energy harvesting configurations are challenging in terms of geometry, material positioning and electrode patterns. Numerical methods are needed to predict and simulate the electromechanical behavior of such systems.

In their pioneering work on finite element modeling of piezoelectric vibration analysis, Allik and Hughes [38] proposed a formulation with mechanical displacements and electric potential as the unknown field variables and took into account both direct and inverse piezoelectric effects. Since then numerous finite element models have been developed—including beam, shell, plate and solid elements—to analyze piezoelectric vibrations. A survey of different finite element formulations for piezoelectrics can be found in [39]. Many of the reviewed finite elements use the unknowns as suggested by [38] with a linear approximation of the electric potential through the thickness of the element. Mixed and hybrid finite element formulations are presented in references [46, 48–50, 67]. These formulations contain additional assumed fields besides mechanical displacements and electrical potential which reduces locking phenomenon and makes the elements less susceptible to mesh distortion. The most general formulation was presented by Sze [48] and contained six independent unknown fields, viz., displacements, strains and stresses for the mechanical part and electric potential, electric field and dielectric displacements for the electric part. Further mixed formulations with three and four assumed fields are derived from the six field formulation. A six field formulation was proposed by Klinkel [49, 50] with additional enhancements for strain and electric field. Thomas et al. [44] proposed a finite element formulation for piezoelectric elements that contained only two piezoelectric variables per piezoelectric patches namely the voltage between the electrodes covering the patches and the charge contained in the electrodes. The circuit equation was added to the system of equations as an additional relation between voltage, charge and their respective time derivatives.

This chapter presents a three-dimensional monolithic mixed-hybrid finite element formulation with six independent unknown fields—velocities, stresses, potential rate, dielectric displacements, electric charge, and electric potential—in time domain and frequency domain for piezoelectric vibration analysis. For the time domain analysis, the governing equations are discretized by time-discontinuous space-time finite elements leading to a uniform discretization of and simultaneous solution to the coupled problem. Hughes and Hulbert [68] introduced stabilized space-time finite element method for elastodynamics and applied their formulation for wave propagation problems. The fully discrete method enables consistent discretization of space and time, enabling the variation of temporal discretization over the spatial domain [7, 68]. For the frequency domain analysis, the monolithic semi-discrete weak form of the governing equations is converted into a rational eigenvalue problem. The eigenvalues and eigenvectors are obtained after converting the rational eigenvalue problem into a first order system.

The proposed formulation has several advantages. The monolithic formulation enables to calculate the natural frequencies of a piezoelectric harvester in the presence of any resistive load. This is unlike many of the referenced articles (for instance, see [35, 61]) in which the natural frequencies are calculated first for the uncoupled system, and the natural frequencies in the presence of a finite resistive load are inferred from the voltage and displacement frequency response functions (FRFs). The three-dimensional modeling approach enables straight forward application of the piezoelectric constitutive laws. They allow to describe the electromechanical behavior without assuming the electrical field and electrical displacement to vanish in particular directions, leading to a proper satisfaction of the Gauss' law. The formulation is also unique in its treatment of equipotentiality condition in the electrodes. The local *electric potential rate* variables in the electroded faces of the three-dimensional elements discretizing the piezoelectric patches are coupled to the global *electric potential* variable through the local boundary *electric charge* variables. This naturally enforces the equipotentiality condition. The electric charge variables can be thought of as Lagrange multipliers from a mathematical perspective.

3.2 Model equations for a generic piezoelectric EHD

The strong form of equations governing the electromechanical behavior of a generic piezoelectric energy harvester are given in this section.

As an illustration, we consider an arbitrarily shaped elastic structure occupying a domain Ω_s with boundary $\partial\Omega_s$ and equipped with a piezoelectric layer occupying a domain Ω_p with boundary $\partial\Omega_p$ (Fig. 3.1). Without loss of generality, the piezoelectric layer is assumed to be fully and continuously covered on its top and bottom surfaces with perfectly conducting electrodes. The electrodes are equipotential surfaces with negligible thickness. The surfaces of the upper and lower electrodes are denoted by Γ_u^ψ and Γ_l^ψ respectively, such that $\Gamma_p^\psi = \Gamma_u^\psi \cup \Gamma_l^\psi$. In this example, a resistive load (R) is considered as the attached circuit, which is a common assumption in modeling piezoelectric EHDs.

Linear Piezoelectricity For the piezoelectric layer in this example, the rate form of the direct and inverse constitutive equations describing the coupling properties can be expressed as

$$\dot{\mathbf{S}} - [s^{\vec{D}}]\dot{\mathbf{T}} - [g]^\top \dot{\vec{D}} = \mathbf{0} \quad \text{in} \quad \Omega_p, \tag{3.1}$$

$$\dot{\vec{E}} - [g]\dot{\mathbf{T}} - [\varepsilon^{\mathbf{T}}]^{-1}\dot{\vec{D}} = \vec{0} \quad \text{in} \quad \Omega_p, \tag{3.2}$$

where $\mathbf{T}$ is the Cauchy stress tensor, $\mathbf{S}$ is the strain tensor, $\vec{E}$ is the electric field vector, $\vec{D}$ is the vector of electrical displacements, $[s^{\vec{D}}]$ is the elastic compliance matrix measured at constant electrical displacement, $[g]$ is the matrix of piezoelectric coupling coefficients in strain-voltage form, and $[\varepsilon^{\mathbf{T}}]$ is the dielectric matrix measured at constant stress. $\mathbf{S}$ and $\vec{E}$ are energy conjugates of $\mathbf{T}$ and $\vec{D}$ respectively. Equivalent representations of Eqs. (3.1) and (3.2) can be obtained by using different forms of piezoelectric coupling coefficients. The mechanical quantities are one tensorial rank higher than the corresponding electrical quantities.

The mechanical equilibrium equation is given by

$$\rho\dot{\vec{v}} - \nabla \cdot \mathbf{T} - \vec{f} = \vec{0} \quad \text{in} \quad \Omega_p, \tag{3.3}$$

where Eq. (3.3) corresponds to the conservation of linear momentum of a solid body for small deformations. Here, ρ denotes the mass density of the piezoelectric structure, $\vec{v}$ the vector of structural velocities, and $\vec{f}$ the vector of body forces. The gradient relation between the linear strain rate tensor and the velocity is given by

$$\dot{\mathbf{S}} - \frac{1}{2}[\nabla\vec{v} + (\nabla\vec{v})^\top] = \mathbf{0} \quad \text{in} \quad \Omega_p. \tag{3.4}$$

The electrical behavior of the piezoelectric structure is adequately described by a quasi-static approach. The piezoelectric structure is considered to be a perfect insulator with no volumetric charge density. Thus, the fundamental electrostatics equations are:

$$\nabla \cdot \vec{D} = 0 \quad \text{in} \quad \Omega_p, \tag{3.5}$$

$$\dot{\vec{E}} + \nabla\psi = \vec{0} \quad \text{in} \quad \Omega_p. \tag{3.6}$$

Equation (3.5) is the differential form of Gauss' law, and Eq. (3.6) is the gradient relation between the electric field rate $\dot{\vec{E}}$ and the rate of electric potential ψ. We consider the following partition of the boundary $\partial\Omega_p$ of the piezoelectric structure

$$\Gamma_p^v \cup \Gamma_p^t = \Gamma_p^\psi \cup \Gamma_p^q = \partial\Omega_p, \tag{3.7}$$

$$\Gamma_p^v \cap \Gamma_p^t = \Gamma_p^\psi \cap \Gamma_p^q = \emptyset, \tag{3.8}$$

where Γ_p^v is the part of $\partial\Omega_p$ on which velocities $\bar{\vec{v}}$ may be prescribed as

$$\vec{v} - \bar{\vec{v}} = \vec{0} \quad \text{on} \quad \Gamma_p^v, \tag{3.9}$$

and Γ_p^t is the part of $\partial\Omega_p$ on which the traction vector $\bar{\vec{t}}$ may be prescribed as

$$\mathbf{T} \cdot \vec{n} - \bar{\vec{t}} = \vec{0} \quad \text{on} \quad \Gamma_p^t. \tag{3.10}$$

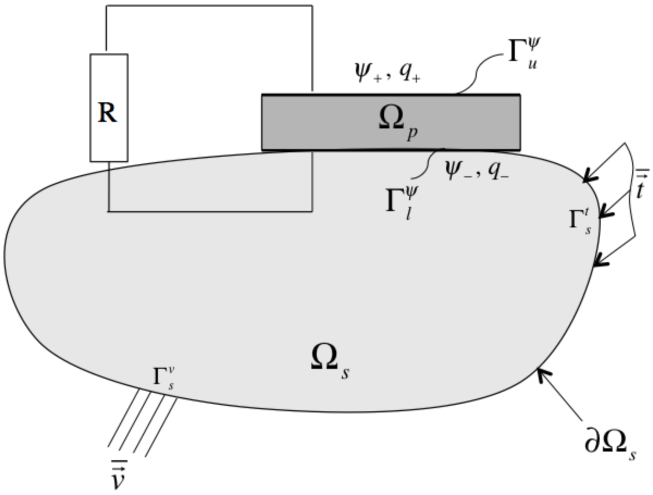

Figure 3.1: An elastic structure with a piezoelectric patch: 2D illustration

Electrodes Electrodes are essential for applying electrical boundary conditions. A piezoelectric structure without conducting electrodes has no structural application; hence, the electrical boundary conditions are essentially equations pertaining to the electrodes. In this example, Γ_p^ψ represents the electroded pats of $\partial\Omega_p$ and Γ_p^q represents the unelectroded parts of $\partial\Omega_p$. On Γ_p^ψ, the electrical essential boundary conditions are given by

$$\psi_+ - \psi = 0 \quad \text{on} \quad \Gamma_u^\psi, \tag{3.11}$$

$$\psi_- - \psi = 0 \quad \text{on} \quad \Gamma_l^\psi, \tag{3.12}$$

where ψ_+ and ψ_- are the potential rates at the top and bottom electrodes respectively. They are spatially constant and vary only with time. The electrical natural boundary condition on the electroded parts is given by

$$\vec{D} \cdot \vec{n} + \bar{q} = 0 \quad \text{on} \quad \Gamma_p^q, \tag{3.13}$$

where $\bar{q}$ is the free charge density per unit surface area. We assume the free charge density in this example to be zero on the unelectroded surfaces. The mechanical effects on the electrodes can be neglected because of their relatively small thickness.

The time-dependent electric potential developed between the electrodes covering the patches due to the straining of the harvester is given by

$$\dot{\phi} = \psi_+ - \psi_- \quad \text{on} \quad \Gamma_p^\psi. \tag{3.14}$$

It is common in energy harvesting applications to ground one of the electrodes and leave the other electrode open for floating potential to develop. In this example, the lower electrode is grounded by setting the potential rate to zero on Γ_l^ψ. Equation (3.12) can thus be rewritten as

$$\psi_- = \psi = 0 \quad \text{on} \quad \Gamma_l^\psi. \tag{3.15}$$

The total free electric charge Q_e on the electrodes Γ_u^ψ and Γ_l^ψ can be expressed as

$$Q_e = \int_{\Gamma_u^\psi} q_+ \, \mathrm{d}\Gamma = -\int_{\Gamma_l^\psi} q_- \, \mathrm{d}\Gamma. \tag{3.16}$$

Circuit The electrical circuit consists of a simple resistive load connected to the electrodes of the piezoelectric layer. Ohm's law is a relation between the current (I) flowing through a conductor between two points and the potential (ϕ) developed across the two points. It is expressed as

$$\phi - R \cdot I = 0, \tag{3.17}$$

where R is the resistance offered by the conductor. In the circuit configuration we are considering, the resistive load is directly connected to the harvester. Therefore, it can be considered that the voltage across the resistor element is equal to the voltage developed between the electrodes of the piezoelectric layer. This assumption enables a native coupling between the harvesting circuit and the harvester. The current flowing out of the upper electrode (since the potential rate on the lower electrode is set to zero) is given by

$$I = -\dot{Q}_e. \tag{3.18}$$

Substituting Eqs. (3.16) and (3.17) in Eq. (3.18), the governing equations that describe the coupling between the circuit and the electrodes can be expressed as

$$\frac{\phi}{R} + \int_{\Gamma_u^\psi} \dot{q}_+ \, \mathrm{d}\Gamma_p. \tag{3.19}$$

Elastic Structure For the linear elastic structure at small deformations occupying the domain Ω_s with boundary $\partial\Omega_s$, the governing equations are essentially the same as the governing equations for the piezoelectric layer but without the electrical variables. The equations can be summarized as

$$\dot{\mathbf{S}} - [s]\dot{\mathbf{T}} = \mathbf{0} \quad \text{in} \quad \Omega_s, \tag{3.20}$$

$$\rho\dot{\vec{v}} - \nabla \cdot \mathbf{T} - \vec{f} = \vec{0} \quad \text{in} \quad \Omega_s, \tag{3.21}$$

$$\dot{\mathbf{S}} - \frac{1}{2}[\nabla\vec{v} + (\nabla\vec{v})^\top] = \mathbf{0} \quad \text{in} \quad \Omega_s. \tag{3.22}$$

$$\vec{v} - \bar{\vec{v}} = \vec{0} \quad \text{on} \quad \Gamma_s^v, \tag{3.23}$$

$$\mathbf{T} \cdot \vec{n} - \bar{\vec{t}} = \vec{0} \quad \text{on} \quad \Gamma_s^t, \tag{3.24}$$

where $\Gamma_s^v \cup \Gamma_s^t = \partial\Omega_s$ and $\Gamma_s^v \cap \Gamma_s^t = \emptyset$. Here, $[s]$ is the elastic compliance matrix, ρ the density, $\mathbf{T}$ the stress tensor, and $\mathbf{S}$ the strain tensor.

Thus, Eqs. (3.1)–(3.24) are the strong form of the governing equations for an energy harvester coupled with an electrical circuit. Since the electrical circuit is directly connected to the harvester as evident from Eq. (3.19), the value of the load resistor will influence the vibration amplitude of the harvester. Here, we shall see that this influence is quite sophisticated and requires careful treatment for reliable results on the power output as well as the identification of optimal harvesting configuration. In the following sections it will be shown that modeling the effect of the electrical circuit as viscous damping is inappropriate.

3.3 Frequency Domain Analysis

In this section, the weak form of the model equations given in Sect. 3.2 is derived for frequency domain analysis in a mixed formulation and presented along with the discretization method. Piezoelectric harvesters are typically very thin. Irreducible three-dimensional finite element formulations for thin structures are susceptible to locking phenomenon, and mixed formulations mitigate this locking phenomenon by considering additional unknowns besides the primary unknown fields.

3.3.1 Weak Form

Piezoelectric Layer The weak form for the piezoelectric layer is expressed in terms of six unknown field variables, namely the velocities $\vec{v}$, the assumed stresses $\mathbf{T}$, the electric potential rate ψ, the assumed electric displacements $\vec{D}$, the electric charge q, and the global electric potential ϕ. It is derived from the strong form equations by the method of weighted residuals and reads after integration by parts as

$$\int_{\Omega_p} \delta\vec{v}\cdot(\rho\dot{\vec{v}} - \vec{f})\,\mathrm{d}\Omega_p + \int_{\Omega_p} \dot{\mathbf{S}}(\delta\vec{v}) : \mathbf{T}\,\mathrm{d}\Omega_p + \int_{\Omega_p} \dot{\vec{E}}(\delta\psi)\cdot\vec{D}\,\mathrm{d}\Omega_p \tag{3.25a}$$

$$+\sum_e \int_{\Omega_p^e} \delta\mathbf{T} : ([s^{\vec{D}}]\dot{\mathbf{T}} + [g]^\top\dot{\vec{D}} - \dot{\mathbf{S}}(\vec{v}))\,\mathrm{d}\Omega_p \tag{3.25b}$$

$$+\sum_e \int_{\Omega_p^e} \delta\vec{D}\cdot([g]\dot{\mathbf{T}} + [\varepsilon^{\mathbf{T}}]^{-1}\dot{\vec{D}} - \dot{\vec{E}}(\psi))\,\mathrm{d}\Omega_p - \int_{\Gamma_p^t} \delta\vec{v}\cdot\bar{\vec{t}}\,\mathrm{d}\Gamma_p \tag{3.25c}$$

$$+\int_{\Gamma_u^\psi} \delta q_+\dot{\phi}\,\mathrm{d}\Gamma_p + \int_{\Gamma_u^\psi} \delta\phi\dot{q}_+\,\mathrm{d}\Gamma_p \tag{3.25d}$$

$$-\int_{\Gamma_u^\psi} \delta q_+\psi_+\,\mathrm{d}\Gamma_p - \int_{\Gamma_u^\psi} \delta\psi_+ q_+\,\mathrm{d}\Gamma_p \tag{3.25e}$$

$$+\,\delta\phi\frac{\phi}{R} \;=\; 0 \qquad \forall\;\delta\vec{v},\;\delta\psi,\;\delta\phi,\;\delta q,\;\delta\mathbf{T},\;\delta\vec{D}. \tag{3.25f}$$

Equation (3.25a) corresponds to the weak form of the momentum conservation and Gauss' law. Equations (3.25b) and the first integral in Eq. (3.25c) represent the weak form of the field Eqs. (3.4) and (3.6), where the constitutive law is fulfilled exactly on an element level, leading to a mixed-hybrid formulation. It is worth remarking that the electrical boundary integrals are obtained by considering Eq. (3.14) as a constraint to enforce equipotentiality condition of the top electrode and considering Eq. (3.19) as a constraint to enable the coupling between the circuit and the electrodes.

The mixed formulation described in Eq. 3.25 is similar to the variational form presented in Sze and Pan [48]. The point of departure in this work is the consideration of velocities and electric potential rate instead of displacement and electric potential in Eq. 3.25. This consideration also lends itself to a natural resolution of the equipotential condition. Another efficient way of considering the equipotential condition is presented in [69]. Once again, the point of departure is due to the consideration of the primary variables in rate formulation.

Elastic Structure For the linear elastic structure at small deformations, the weak form is obtained using the same basic principle and expressed as

$$\int_{\Omega_s} \delta\vec{v}\cdot(\rho\dot{\vec{v}} - \vec{f})\,\mathrm{d}\Omega_s + \int_{\Omega_s} \dot{\mathbf{S}}(\delta\vec{v}) : \mathbf{T}\,\mathrm{d}\Omega_s \tag{3.26a}$$

$$+\sum_e \int_{\Omega_s^e} \delta\mathbf{T} : ([s^{\vec{D}}]\dot{\mathbf{T}} - \dot{\mathbf{S}}(\vec{v}))\,\mathrm{d}\Omega_s \tag{3.26b}$$

$$-\int_{\Gamma_s^t} \delta\vec{v}\cdot\bar{\vec{t}}\,\mathrm{d}\Gamma_s \;=\; 0 \qquad \forall\;\delta\vec{v},\;\delta\mathbf{T}. \tag{3.26c}$$

Equations (3.25) and (3.26), together, constitute the monolithic integral form of the coupled energy harvesting problem. It should be noted that Eq. (3.26) is valid only if the elastic substrate Ω_s is a conducting material because both the electric field and electric displacement will vanish within a conductor. If Ω_s is a dielectric material, only the coupling coefficient will vanish, but the electric field will be present. Also, if there are many piezoelectric layers present, all the electrodes glued to the conducting part of Ω_s must be electrically connected in such a way that they share the same potential. Otherwise, they must be located far enough that the electrical field in Ω_s is of the same order of magnitude as in Ω_p [44].

3.3.2 Finite Element Discretization

Three-dimensional volumetric elements are employed to discretize Ω_p and Ω_s. Within an element, the geometry and the continuous field variables are interpolated from their nodal values using standard tensor product interpolation functions. For the piezoelectric layer, velocities and electric potential rate are defined as the nodal degrees of freedom (d.o.f.s.) of the elements discretizing Ω_p. This ensures zeroth-order continuity of the velocities ($\vec{v}$) and electric potential rate (ψ) at the elements' interface. For the elastic structure, only the velocities are defined as the nodal degrees of freedom of the elements discretizing Ω_s, thereby satisfying Eq. (3.9). There is no continuity requirement on the other two variables, namely the assumed stresses and dielectric displacements. At the interface between Ω_p and Ω_s, the nodes of the elements discretizing each of the domains must coincide. The interpolation functions are expressed as follows

$$\vec{x}^e = \mathbf{N}_x \hat{\vec{x}}^e, \quad \vec{v}^e = \mathbf{N}_v \hat{\vec{v}}^e, \quad \psi^e = \mathbf{N}_\psi \hat{\vec{\psi}}^e, \tag{3.27}$$

where $\hat{\vec{x}}^e, \hat{\vec{v}}^e$ and $\hat{\vec{\psi}}^e$ are the vectors of nodal co-ordinates, nodal velocities and nodal potential rate respectively. $\mathbf{N}_x$ is the coordinate interpolation matrix, $\mathbf{N}_v$ is the velocity interpolation matrix, and $\mathbf{N}_\psi$ is the potential rate interpolation matrix. Because the stress tensor $\mathbf{T}$ and the strain tensor $\mathbf{S}$ are symmetric, they can conveniently be expressed as vectors of six components using *Voigt* notation as $\vec{T} = \{t_{xx},\ t_{yy},\ t_{zz},\ t_{yz},\ t_{xz}\ t_{xy}\}^\top$ and $\vec{S} = \{s_{xx},\ s_{yy},\ s_{zz},\ 2s_{yz},\ 2s_{xz}\ 2s_{xy}\}^\top$, respectively. Substituting Eq. (3.27) in Eqs. (3.4) and (3.6), the strain $\vec{S}$ and electric field $\vec{E}$ in the element can be expressed as

$$\vec{S}^e = \mathbf{B}_v \hat{\vec{v}}^e, \quad \vec{E}^e = -\mathbf{B}_\psi \hat{\vec{\psi}}^e, \tag{3.28}$$

where $\mathbf{B}_v$ and $\mathbf{B}_\psi$ are the matrices containing the global spatial derivatives of the velocity shape functions and electric potential rate shape functions respectively. The assumed stresses and electric displacements are defined only inside the elements, and they are discontinuous at the element edge. The shape functions for the assumed stresses and electric displacements are the same as the functions employed in [48] and are expressed within an element as

$$\vec{T}^e = \mathbf{N}_t \hat{\vec{T}}^e, \quad \vec{D}^e = \mathbf{N}_d \hat{\vec{\beta}}^e, \tag{3.29}$$

where $\mathbf{N}_t$ is the stress shape function matrix, $\hat{\vec{T}}^e$ is the vector of local stress components, $\mathbf{N}_d$ is the electric displacement shape function matrix, and $\hat{\vec{\beta}}^e$ is the vector of local electric displacement components. For a typical isoparametric hexahedral element with eight nodes, 18 stress components and 7 electric displacement components are needed to secure proper element rank.

Isoparametric surface elements are employed to discretize Γ_u^ψ with electric charge (q) and electric potential (ψ) as nodal degrees of freedom. The interpolation of the electric charge is expressed as

$$q^e = \mathbf{N}_q \hat{\vec{q}}^e. \tag{3.30}$$

At the piezoelectric layer–electrode interface, the top nodes of the volumetric elements discretizing Ω_p must coincide with nodes of the surface elements discretizing (Γ_u^ψ) to couple the electrode and the piezoelectric patch. We are now left with the global electric potential (ϕ). As mentioned earlier, ϕ is spatially constant and varies only with time. It is coupled to the local potential rate (ψ) variables at the nodes of the elements discretizing (Γ_u^ψ) through electric charge (q). This much is evident from the way the weak form is formulated. Thus, the shape function $\mathbf{N}_\phi$ for ϕ is identity and expressed as $\phi = 1 \cdot \hat{\phi}$.

3.3.3 Discrete Equation of Motion and Dynamic Condensation to Rational Eigenvalue Problem

Discretization of the mixed weak form expressed by Eq. (3.25) and Eq. (3.26) using the above introduced finite element ansatz functions, leads to the semi-discrete electromechanical matrix equation

$$\begin{bmatrix} \mathbf{M}_{vv} & 0 & 0 & 0 & 0 & 0 \\ 0 & 0 & 0 & 0 & 0 & 0 \\ 0 & 0 & 0 & \mathbf{F}_{q\phi} & 0 & 0 \\ 0 & 0 & \mathbf{F}_{\phi q} & 0 & 0 & 0 \\ 0 & 0 & 0 & 0 & \mathbf{F}_{tt} & \mathbf{F}_{td} \\ 0 & 0 & 0 & 0 & \mathbf{F}_{dt} & \mathbf{F}_{dd} \end{bmatrix} \begin{Bmatrix} \hat{\vec{v}} \\ \hat{\vec{\psi}} \\ \hat{\vec{q}} \\ \hat{\phi} \\ \hat{\vec{T}}^e \\ \hat{\vec{\beta}}^e \end{Bmatrix}^{\bullet} + \begin{bmatrix} 0 & 0 & 0 & 0 & \mathbf{K}_{vt} & 0 \\ 0 & 0 & \mathbf{K}_{\psi q} & 0 & 0 & \mathbf{K}_{\psi d} \\ 0 & \mathbf{K}_{q\psi} & 0 & 0 & 0 & 0 \\ 0 & 0 & 0 & \mathbf{K}_{\phi\phi} & 0 & 0 \\ \mathbf{K}_{tv} & 0 & 0 & 0 & 0 & 0 \\ 0 & \mathbf{K}_{d\psi} & 0 & 0 & 0 & 0 \end{bmatrix} \begin{Bmatrix} \hat{\vec{v}} \\ \hat{\vec{\psi}} \\ \hat{\vec{q}} \\ \hat{\phi} \\ \hat{\vec{T}}^e \\ \hat{\vec{\beta}}^e \end{Bmatrix} = \begin{Bmatrix} \vec{f}_v(t) \\ \vec{0} \\ \vec{0} \\ 0 \\ \vec{0} \\ \vec{0} \end{Bmatrix} \tag{3.31}$$

where $\hat{\vec{T}}^e$ and $\hat{\vec{\beta}}^e$ are element-local unknowns. The entries in the above sub-matrices and sub-vectors result from assembly of finite element contributions (indicated by symbol A)

$$\mathbf{M}_{vv} = \mathop{\mathsf{A}}_{e} \mathbf{M}_{vv}^e \quad \text{with} \quad \mathbf{M}_{vv}^e = \int_{\Omega_e} \rho \mathbf{N}_v^{e\top} \mathbf{N}_v^e \, \mathrm{d}\Omega, \tag{3.32a}$$

$$\mathbf{F}_{q\phi} = \mathop{\mathsf{A}}_{e} \mathbf{F}_{q\phi}^e \quad \text{with} \quad \mathbf{F}_{q\phi}^e = \int_{\Omega_e} \mathbf{N}_q^{e\top} \mathbf{N}_\phi^e \mathrm{d}\Omega \quad \text{and} \quad \mathbf{F}_{\phi q} = \mathbf{F}_{q\phi}^\top, \tag{3.32b}$$

$$\mathbf{F}_{td} = \mathop{\mathsf{A}}_{e} \mathbf{F}_{td}^e \quad \text{with} \quad \mathbf{F}_{td}^e = \int_{\Omega_e} \mathbf{N}_t^\top [g]^\top \mathbf{N}_d \, \mathrm{d}\Omega \quad \text{and} \quad \mathbf{F}_{dt} = \mathbf{F}_{td}^\top, \tag{3.32c}$$

$$\mathbf{F}_{tt} = \mathop{\mathsf{A}}_{e} \mathbf{F}_{tt}^e \quad \text{with} \quad \mathbf{F}_{tt}^e = \int_{\Omega_e} \mathbf{N}_t^{e\top} [s^{\vec{D}}] \mathbf{N}_t^e \, \mathrm{d}\Omega, \tag{3.32d}$$

$$\mathbf{F}_{dd} = \mathop{\mathsf{A}}_{e} \mathbf{F}_{dd}^e \quad \text{with} \quad \mathbf{F}_{dd}^e = \int_{\Omega_e} \mathbf{N}_d^{e\top} [\varepsilon^{\mathbf{T}}] \mathbf{N}_d^e \, \mathrm{d}\Omega, \tag{3.32e}$$

$$\mathbf{K}_{vt} = \mathop{\mathsf{A}}_{e} \mathbf{K}_{vt}^e \quad \text{with} \quad \mathbf{K}_{vt}^e = \int_{\Omega_e} \mathbf{B}_v^{e\top} \mathbf{N}_t^e \, \mathrm{d}\Omega \quad \text{and} \quad \mathbf{K}_{tv} = -\mathbf{K}_{vt}^\top, \tag{3.32f}$$

$$\mathbf{K}_{\psi d} = \mathop{\mathsf{A}}_{e} \mathbf{K}_{vt}^e \quad \text{with} \quad \mathbf{K}_{vt}^e = \int_{\Omega_e} \mathbf{B}_\psi^{e\top} \mathbf{N}_d^e \, \mathrm{d}\Omega \quad \text{and} \quad \mathbf{K}_{d\psi} = -\mathbf{K}_{\psi d}^\top, \tag{3.32g}$$

$$\mathbf{K}_{\psi q} = \mathop{\mathsf{A}}_{e} \mathbf{K}_{\psi q}^e \quad \text{with} \quad \mathbf{K}_{\psi q}^e = -\int_{\Omega_e} \mathbf{N}_\psi^{e\top} \mathbf{N}_q^e \, \mathrm{d}\Omega \quad \text{and} \quad \mathbf{K}_{q\psi} = \mathbf{K}_{\psi d}^\top, \tag{3.32h}$$

$$\mathbf{K}_{\phi\phi} = \mathbf{N}_\phi^{e\top} \frac{1}{R} \mathbf{N}_\phi^e, \tag{3.32i}$$

$$\vec{f}_v(t) = \mathop{\mathsf{A}}_{e} \vec{f}_v^e(t) \quad \text{with} \quad \vec{f}_v^e(t) = \int_{\Omega} \mathbf{N}_v^{e\top} \vec{f}(t) \, \mathrm{d}\Omega + \int_{\Gamma_e^t} \mathbf{N}_v^{e\top} \vec{\bar{t}}(t) \, \mathrm{d}\Gamma. \tag{3.32j}$$

Due to the local character of the assumed stress and dielectric displacement fields, the associated degrees of freedom can be condensed dynamically on the level of those finite elements describing the piezoelectric subdomain. Such a procedure considerably reduces the total number of degrees of freedom in the system of linear equations that is produced as a result of the assembly of all discrete (condensed) finite element contributions.

The process of per-element dynamic condensation for piezoelectric finite elements is based on the generic ansatz

$$\hat{\vec{x}}(t) = \tilde{\vec{x}} \cdot e^{\lambda t} \tag{3.33}$$

and allows to rewrite the respective parts in the homogeneous limit of the equation of motion (3.31) in the form

$$\begin{bmatrix} \lambda \mathbf{M}^e_{vv} & 0 & \mathbf{K}^e_{vt} & 0 \\ 0 & 0 & 0 & \mathbf{K}^e_{\psi d} \\ \mathbf{K}^e_{tv} & 0 & \lambda \mathbf{F}^e_{tt} & \lambda \mathbf{F}^e_{td} \\ 0 & \mathbf{K}^e_{d\psi} & \lambda \mathbf{F}^e_{dt} & \lambda \mathbf{F}^e_{dd} \end{bmatrix} \begin{Bmatrix} \tilde{\vec{v}}^e \\ \tilde{\vec{\psi}}^e \\ \tilde{\vec{T}}^e \\ \tilde{\vec{\beta}}^e \end{Bmatrix} = \vec{0}. \tag{3.34}$$

Assumed stresses and electrical displacements can now be eliminated using the Schur complement method on the element level. The condensed element matrix representation of the elements discretizing Ω_p is then given by

$$\left(\lambda \begin{bmatrix} \mathbf{M}^e_{vv} & 0 \\ 0 & 0 \end{bmatrix} - \frac{1}{\lambda} \mathbf{G}^e \right) \begin{Bmatrix} \tilde{\vec{v}}^e \\ \tilde{\vec{\psi}}^e \end{Bmatrix} = \vec{0}, \tag{3.35}$$

where the hybridized stiffness matrix $\mathbf{G}^e$ is given by

$$\mathbf{G}^e = \begin{bmatrix} \mathbf{K}^e_{vt} & 0 \\ 0 & \mathbf{K}^e_{\psi d} \end{bmatrix} \times \begin{bmatrix} \mathbf{F}^e_{tt} & \mathbf{F}^e_{td} \\ \mathbf{F}^e_{dt} & \mathbf{F}^e_{dd} \end{bmatrix}^{-1} \times \begin{bmatrix} \mathbf{K}^e_{tv} & 0 \\ 0 & \mathbf{K}^e_{d\psi} \end{bmatrix} \tag{3.36}$$

and these can be computed on the element level at reasonable cost. The global set of equations of motion for the entire assembled homogeneous problem is then obtained as

$$\left[\lambda \mathbf{M} + \mathbf{C} - \frac{1}{\lambda} \mathbf{H} \right] \tilde{\vec{\alpha}} = \vec{0}, \tag{3.37}$$

where

$$\mathbf{M} = \begin{bmatrix} \mathbf{M}_{vv} & 0 & 0 & 0 \\ 0 & 0 & 0 & 0 \\ 0 & 0 & 0 & \mathbf{F}_{q\phi} \\ 0 & 0 & \mathbf{F}_{\phi q} & 0 \end{bmatrix}, \ \mathbf{C} = \begin{bmatrix} 0 & 0 & 0 & 0 \\ 0 & 0 & \mathbf{K}_{\psi q} & 0 \\ 0 & \mathbf{K}_{q\psi} & 0 & 0 \\ 0 & 0 & 0 & \mathbf{K}_{\phi\phi} \end{bmatrix}, \ \tilde{\vec{\alpha}} = \begin{Bmatrix} \tilde{\vec{v}} \\ \tilde{\vec{\psi}} \\ \tilde{\vec{q}} \\ \tilde{\phi} \end{Bmatrix}, \ \mathbf{H} = \begin{bmatrix} \multicolumn{2}{c}{\multirow{2}{*}{$\mathbf{G}$}} & 0 & 0 \\ & & 0 & 0 \\ 0 & 0 & 0 & 0 \\ 0 & 0 & 0 & 0 \end{bmatrix} \tag{3.38a}$$

in which $\mathbf{G} = \underset{e}{\mathsf{A}}\, \mathbf{G}^e$ is obtained by assembly of element matrix contributions.

Equation (3.37) is a pesudo-rational eigenvalue problem, and the eigenvalues and eigenvectors are obtained by transformation into a first order system. The resulting sparse first order eigenproblem is solved with the implicitly restarted Arnoldi method. The eigenvalues ($\lambda_r = -\delta_r \pm i\omega_r$) are obtained as complex-conjugate pairs with real and imaginary part. The main advantage of the formulation is that eigenvalues and eigenmodes can be obtained not just for the short-circuit and open-circuit configurations but for any finite value of resistance.

The structural damping of a desired mode is achieved using mass proportional damping and given by

$$\tilde{\mathbf{D}}_{vv} = \gamma_r \mathbf{M}_{vv}, \tag{3.39}$$

where γ_r is the modal mass-proportional damping coefficient calculated from experimentally obtained modal damping ratio (ζ_r) using the formula

$$\gamma_r = 2\zeta_r \omega_r, \tag{3.40}$$

where ω_r is the natural frequency of the mode considered. $\tilde{\mathbf{D}}_{vv}$ is subsequently incorporated in the damping matrix given in Eq. (3.37) as

$$\mathbf{C} = \begin{bmatrix} \tilde{\mathbf{D}}_{vv} & 0 & 0 & 0 \\ 0 & 0 & \mathbf{K}_{\psi q} & 0 \\ 0 & \mathbf{K}_{q\psi} & 0 & 0 \\ 0 & 0 & 0 & \mathbf{K}_{\phi\phi} \end{bmatrix}. \tag{3.41}$$

Equation (3.41) represents the damping matrix which accounts for the damping effect due to the attached circuit and the damping inherent to the structure. This damping formulation can be extended to include strain-rate damping as well.

3.4 Time Domain Analysis

This section presents the derivation of the weak form of the model equations given in Sect. 3.2 in a space–time finite element setting, along with the discretization procedure, for the time-domain analysis of the coupled problem.

Traditional finite element methods for time-dependent problems are semi-discrete formulations, where finite elements are used for spatial discretization of the problem to reduce the partial differential equations to ordinary differential equations in time. The ordinary differential equations in time are then discretized by schemes like finite difference methods. Semi-discrete discretization leads to structured space-time meshes [68]. Space-time finite element procedures, in contrast to traditional semi-discrete formulations, enable consistent discretization of the space and time domains leading to a uniform discretization of the model equations in their integral form and facilitates unstructured space-time meshes. Moreover, simultaneous solution procedures provide significant advantages for strongly coupled problems by ensuring stability and accelerating the convergence of the strongly coupled problem [7].

The underlying idea behind the space-time finite element method is the inclusion of the temporal axis where a space-time domain Q is subdivided into N time slabs as $Q_n = \Omega_n \times [t_n, t_{n+1}]$ (Fig. 3.2. The time slabs are solved successively, and within each time step the unknown fields are solved simultaneously. The time integration is performed by discontinuous Galerkin method (DG method). The discontinuous approximation of the unknown fields in time leads to additional jump terms in the weak form, because at any time instant t_n the energy has to be equal at the end of the previous time slab at t_n^- and at the beginning of the next time step t_n^+. The DG method is an implicit time integration scheme. The time integration scheme for first order equations is A-stable and third order accurate if the temporal interpolation is linear . For references, see [7, 62, 68, 70–72].

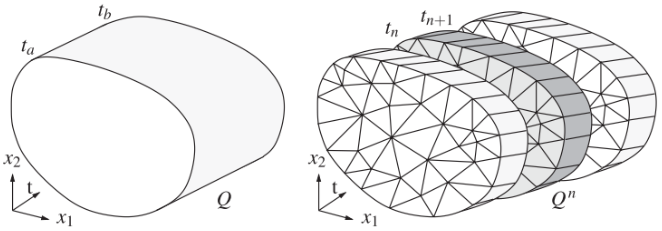

Figure 3.2: Continuous space-time domain discretized using space-time finite elements

3.4.1 Weak Form

Piezoelectric Layer The weak form for the piezoelectric layer—including the electrodes and circuit—is once again expressed in terms of the same six unknown field variables as in the case of frequency domain analysis but in a space–time setting. The Galerkin weighted residual form of the model Eqs. (3.1)–(3.19), within the space-time slab Q_n including the boundaries $P_n = \Gamma_n \times [t_n, t_{n+1}]$, is given as

$$
\begin{aligned}
&\int_{Q_n} \delta\vec{v} \cdot (\rho\dot{\vec{v}} - \vec{f})\, \mathrm{d}Q + \int_{Q_n} \delta\vec{v} \cdot \rho\gamma_r\vec{v}\, \mathrm{d}Q + \int_{Q_n} \dot{\mathbf{S}}(\delta\vec{v}) : \mathbf{T}\, \mathrm{d}Q + \int_{Q_n} \dot{\vec{E}}(\delta\psi) \cdot \vec{D}\, \mathrm{d}Q && \text{(3.42a)}\\
&+ \sum_e \int_{Q_n^e} \delta\mathbf{T} : ([s^{\vec{D}}]\dot{\mathbf{T}} + [g]^\top \dot{\vec{D}} - \dot{\mathbf{S}}(\vec{v}))\, \mathrm{d}Q && \text{(3.42b)}\\
&+ \sum_e \int_{Q_n^e} \delta\vec{D} \cdot ([g]\dot{\mathbf{T}} + [\varepsilon^{\mathbf{T}}]^{-1}\dot{\vec{D}} - \dot{\vec{E}}(\psi))\, \mathrm{d}Q && \text{(3.42c)}\\
&+ \int_{\Omega_n} \delta\vec{v} \cdot \Big(\rho\big(\vec{v}(t_n^+) - \vec{v}(t_n^-)\big)\Big)\mathrm{d}\Omega + \sum_e \int_{\Omega_n^e} \delta\mathbf{T} : \Big([s^{\vec{D}}]\big(\mathbf{T}(t_n^+) - \mathbf{T}(t_n^-)\big)\Big)\mathrm{d}\Omega && \text{(3.42d)}\\
&+ \sum_e \int_{\Omega_n^e} \delta\mathbf{T} : \Big([g]^\top\big(\vec{D}(t_n^+) - \vec{D}(t_n^-)\big)\Big)\mathrm{d}\Omega + \sum_e \int_{\Omega_n^e} \delta\vec{D} \cdot \Big([g]\big(\mathbf{T}(t_n^+) - \mathbf{T}(t_n^-)\big)\Big)\mathrm{d}\Omega && \text{(3.42e)}\\
&+ \sum_e \int_{\Omega_n^e} \delta\vec{D} \cdot \Big([\varepsilon^{\mathbf{T}}]^{-1}\big(\vec{D}(t_n^+) - \vec{D}(t_n^-)\big)\Big)\mathrm{d}\Omega - \int_{P_n^t} \delta\vec{v} \cdot \bar{\vec{t}}\,\mathrm{d}P && \text{(3.42f)}\\
&+ \int_{P_{n,u}^\psi} \delta q_+ \dot{\phi}\, \mathrm{d}P + \int_{P_{n,u}^\psi} \delta\phi \dot{q}_+\, \mathrm{d}P && \text{(3.42g)}\\
&- \int_{P_{n,u}^\psi} \delta q_+ \psi_+\, \mathrm{d}P - \int_{P_{n,u}^\psi} \delta\psi_+ q_+\, \mathrm{d}P && \text{(3.42h)}\\
&+ \int_{\Gamma_{n,u}^\psi} \delta q_+\big(\phi(t_n^+) - \phi(t_n^-)\big)\mathrm{d}\Gamma + \int_{\Gamma_{n,u}^\psi} \delta\phi\big(q_+(t_n^+) - q_+(t_n^-)\big)\mathrm{d}\Gamma && \text{(3.42i)}\\
&+ \delta\phi\frac{\phi}{R} = 0 \qquad \forall\ \delta\vec{v},\ \delta\psi,\ \delta\phi,\ \delta q,\ \delta\mathbf{T},\ \delta\vec{D}. && \text{(3.42j)}
\end{aligned}
$$

Equation (3.42) is very similar to the integral form given in Eq. (3.25). The additional jump terms present in Eqs. (3.42d)–(3.42f) and (3.42i) ensure the transfer of time derivatives from the previous time slab end at t_n^- to the current time slab at t_n^+.

Elastic Structure For the elastic structure, the Galerkin weighted residual form reads as

$$
\begin{aligned}
&\int_{Q_n} \delta\vec{v} \cdot (\rho\dot{\vec{v}} - \vec{f})\, \mathrm{d}Q + \int_{Q_n} \delta\vec{v} \cdot \rho\gamma_r\vec{v}\, \mathrm{d}Q && \text{(3.43a)}\\
&+ \int_{Q_n} \dot{\mathbf{S}}(\delta\vec{v}) : \mathbf{T}\, \mathrm{d}Q + \sum_e \int_{Q_n^e} \delta\mathbf{T} : ([s]\dot{\mathbf{T}} - \dot{\mathbf{S}}(\vec{v}))\, \mathrm{d}Q && \text{(3.43b)}\\
&+ \int_{\Omega_n^e} \delta\vec{v} \cdot \Big(\rho\big(\vec{v}(t_n^+) - \vec{v}(t_n^-)\big)\Big)\mathrm{d}\Omega + \sum_e \int_{\Omega_n} \delta\mathbf{T} : \Big([s]\big(\mathbf{T}(t_n^+) - \mathbf{T}(t_n^-)\big)\Big)\mathrm{d}\Omega && \text{(3.43c)}\\
&- \int_{P_n^t} \delta\vec{v} \cdot \bar{\vec{t}}\,\mathrm{d}P = 0 \qquad \forall\ \delta\vec{v},\ \delta\mathbf{T}. && \text{(3.43d)}
\end{aligned}
$$

Equations (3.42) and (3.43), together, represent the monolithic space–time integral form of the coupled problem introduced in Sect. 3.2. It is worth mentioning that the second integral in Eqs.(3.42a) and (3.43a) contributes to the mechanical damping of a particular mode, and γ_r is the modal mass-proportional damping coefficient calculated based on the experimentally obtained modal damping ratio (Eq.3.40).

3.4.2 Space-Time Finite Element Discretization

For the space-time finite element discretization, we employ the same types of elements as we employed for the discretization in frequency domain analysis. All the conditions regarding the continuity of the assumed field variables along the interfaces remain unchanged. The difference here is the discretization of the time axis. Typical shape functions used in spatial finite elements (Eqs. (3.27)–(3.30)) will have additional temporal components in space-time discretization. For an arbitrary volumetric element, the spatial and temporal components of an interpolation function can be expressed as

$$N_i^t = N_i T^t = N_i(\xi, \eta, \zeta) T^\upsilon(\theta), \tag{3.44}$$

where $i = 1, 2, ...n$ refers to the number of nodes, and $\upsilon = 1, 2, ...$ refers to the temporal division of the time slab. Here, $\xi, \eta, \zeta \in [-1, +1]$ are the natural spatial coordinates, and $\theta \in [-1, +1]$ is the natural temporal coordinate. Assuming linear interpolation in time, the temporal interpolation function can explicitly be expressed as

$$T^1(\theta) = \frac{1}{2}(1 - \theta), \quad T^2(\theta) = \frac{1}{2}(1 + \theta). \tag{3.45}$$

It is convenient to express time derivative of an unknown field by taking the derivative of (3.45) which is given by

$$T^1_{,\theta} = -\frac{1}{2}, \quad T^2_{,\theta} = +\frac{1}{2}. \tag{3.46}$$

Within an element, Eq. (3.27) can now be expressed as

$$\vec{x}^e = [T^1 \mathbf{N}_x \quad T^2 \mathbf{N}_x] \hat{\vec{x}}^e, \quad t^e = T^1 t^1 + T^2 t^2, \tag{3.47a}$$

$$\vec{v}^e = [T^1 \mathbf{N}_v \quad T^2 \mathbf{N}_v] \hat{\vec{v}}^e, \quad \psi^e = [T^1 \mathbf{N}_\psi \quad T^2 \mathbf{N}_\psi] \hat{\vec{\psi}}^e, \tag{3.47b}$$

where t is the temporal coordinate. The spatially discontinuous assumed field variables given in Eq. (3.29), namely the stresses and dielectric displacements are interpolated in a similar way as

$$\vec{T}^e = [T^1 \mathbf{N}_t \quad T^2 \mathbf{N}_t] \hat{\vec{T}}^e, \quad \vec{D}^e = [T^1 \mathbf{N}_d \quad T^2 \mathbf{N}_d] \hat{\vec{\beta}}^e. \tag{3.48}$$

Whereas an isoparametric hexahedral element with eight nodes has 18 stress components and 7 dielectric displacement components in spatial discretization (Sect. 3.3.2), there are 36 stress components and 14 dielectric displacement components in space–time discretization framework, assuming linear interpolation in time. The same discretization principle applies for other unknown field variables too.

The interpolation of electric charge degrees of freedom and the global electric potential is given by

$$q^e = [T^1 \mathbf{N}_q \quad T^2 \mathbf{N}_q] \hat{\vec{q}}^e, \quad \phi = [T^1 \times 1 \quad T^2 \times 1] \hat{\phi}, \tag{3.49}$$

where the spatially constant global electric potential has only two components in time. The derivation here is kept short for the sake of brevity. More detailed derivation can be found in [72].

3.4.3 Solution Procedure

The space-time discretization of a specific time slab Q_n, applied to the weak form of the coupled system given in Eqs. (3.42)–(3.43), leads to a system of coupled linear algebraic equations given by

$$\mathbf{A} \hat{\vec{x}} = \vec{f}(t) \qquad \text{with} \quad \mathbf{A} = \mathop{\mathsf{A}}_{e} \mathbf{A}^e \quad \text{and} \quad \hat{\vec{x}} = \{\hat{\vec{v}}, \hat{\vec{\psi}}, \hat{\vec{q}}, \hat{\phi}\}^\top \tag{3.50}$$

where $\mathbf{A}$ is the global algebraic system matrix, $\hat{\vec{x}}$ is the vector of global unknowns, and $\vec{f}$ is the force vector. Here, the spatially discontinuous mechanical stresses and electrical displacements are statically condensed on the element level, such that element degree of freedom $\hat{\vec{T}}^e$ and $\hat{\vec{\beta}}^e$ are not explicitly present in the final discrete system.

Equation (3.50) is the monolithic algebraic description of the coupled electromechanical problem. The solution to the unknown fields is obtained simultaneously using standard solution procedures.

3.5 Numerical Examples

Two numerical examples are considered in this section. In the first example, the simulation results are compared with the results from the analytical model proposed by Erturk and Inman [36] for a piezoelectric bimorph harvester with series connection of the piezoelectric layers. It is worth mentioning here that this analytical model is a distributed parameter model based on the Euler-Bernoulli beam assumption for which a closed-form solution is available. The numerical model is based on three-dimensional continuum mechanics modeling approach. First, the steady-state electromechanical frequency response functions (FRFs) obtained from the frequency domain analysis—relating the voltage, power and tip velocity outputs to base excitation—are compared with the FRFs in the literature. The steady-state values from the frequency domain analysis are then compared with the results from the time domain analysis when the harvester is excited at certain resonance frequencies. All the comparisons pertain to the first bending mode of the harvester. The second example is the case of a unimorph harvester considered to demonstrate the influence of electrode coverage on the power output of the harvester.

3.5.1 Bimorph Harvester: Series Configuration

The geometric and material properties of the bimorph harvester with tip mass as considered in [36] are given in Table 3.1. In order to apply our formulation, the permittivity $\varepsilon_{33}^{\mathbf{S}}$ ($\varepsilon_0 = 8.854$ pFm^{-1}) and the piezoelectric coupling coefficient d_{31} as given in Table 3.1 have to be reformulated to the form given in Eqs. (3.1) and (3.2).

Table 3.1: Geometric and material properties of the energy harvester

Quantity	Dimension	Value
Length of the beam	l (mm)	50.8
Width of the beam	b (mm)	31.8
Thickness of the piezo. patch (PZT-5A)	h_p (mm)	0.26 (each)
Thickness of the substructure	h_s (mm)	0.14
Young's modulus of the substructure (brass)	Y_s (G Pa)	105
Young's modulus of PZT-5A	Y_p (G Pa)	66
Mass density of the substructure (brass)	ρ_s $\left(\mathrm{Kg\,m^{-3}}\right)$	9000
Mass density of PZT-5A	ρ_p $\left(\mathrm{Kg\,m^{-3}}\right)$	7800
Piezoelectric displacement coefficient	d_{31} $\left(\mathrm{p\,m\,V^{-1}}\right)$	-190
Permittivity	$\varepsilon_{33}^{\mathbf{S}}$ $\left(\mathrm{F\,m^{-1}}\right)$	$1500\,\varepsilon_0$
Modal damping coefficient	γ_r $\left(\mathrm{rad\ ms^{-1}}\right)$	0.0156
Tip mass	M_t (g)	12

$$[\varepsilon^{\mathbf{T}}] = [\varepsilon^{\mathbf{S}}] + [d][c^{\vec{E}}][d]^{\top}, \tag{3.51}$$

$$[\varepsilon^{\mathbf{T}}]^{-1} = ([\varepsilon^{\mathbf{S}}] + [d][c^{\vec{E}}][d]^{\top})^{-1}. \tag{3.52}$$

where $[c^{\vec{E}}]$ is the Young's modulus Y_p of the piezoelectric material measured at constant electric field as given in Table 3.1. The compliance matrix at constant dielectric displacement is obtained from the table values as follows

$$[s^{\vec{D}}] = [c^{\vec{E}}]^{-1} - ([d]^\top [\varepsilon^{\mathbf{T}}]^{-1}[d]), \tag{3.53}$$

and the piezoelectric voltage coefficient derived from displacement coefficient is given by

$$[g] = [\varepsilon^{\mathbf{T}}]^{-1}[d]. \tag{3.54}$$

The finite element discretization, as explained for both frequency and time domain analysis, is now applied to the harvester configuration. The elastic substructure (brass) is discretized by isoparametric hexahedral elements with velocities as nodal degrees of freedom and mechanical stresses as element level degrees of freedom. The interpolation of velocity components is piecewise trilinear in space, leading to 24 velocity components for spatial discretization and 48 velocity components for space-time discretization (piecewise linear in space and discontinuously linear interpolation in time). The interpolation function for stresses is discontinuous in space and time. The piezoelectric layers are discretized by isoparametric hexahedral elements with velocities and electric potential rate as nodal degrees of freedom, and mechanical stresses and electric displacements as element level degrees of freedom. The interpolation of electric potential is piecewise trilinear in space and linearly discontinuous in time, leading to 8 potential rate components for spatial discretization and 16 potential rate components for space-time discretization. The interpolation function for electric displacements, similar to mechanical stresses, is discontinuous in space and time. The electrodes are discretized with isoparametric quadrilateral elements, and the virtual node enables the coupling of the circuit to the bimorph harvester. The sign of the piezoelectric coupling coefficient in the bottom layer is opposite to that of the top layer to enable series connection. The electric potential rate (ψ) degrees of freedom in the nodes of the bottom elements are set to zero (grounded) and the top surface elements (electrodes) are coupled to the virtual node (circuit). The substrate layer is a conductor with no electric field present. This is achieved in the finite element model by setting the (ψ) degrees of freedom s at the top interface between the substructure and the piezoelectric layer equal to the (ψ) degrees of freedom in the bottom interface between the substructure and the piezoelectric layer. This constraint is enforced here with the help of Lagrange multipliers.

For harvesters subjected to base excitation, the effective force on the harvester is due to it's inertia. Hence, a harmonic excitation is imposed on the transverse velocity degrees of freedom on the fixed end of the cantilever as

$$\hat{\vec{f}}(t) = (\tilde{\vec{p}} - i\tilde{\vec{q}})e^{\Omega t}. \tag{3.55}$$

To replicate the scenario reported in the literature, the harvester is accelerated at $1g$ ($g = 9.81$ m/s^2).

The comparison of numerically obtained voltage FRF with the FRF obtained analytically [36] for three different values of load resistance is given in Fig. 3.3(a). For the harvester properties considered in this example, 1 kΩ resistive load is very close to the short-circuit condition ($R \to 0$) and 470 kΩ is close to the open-circuit condition ($R \to \infty$). These resistance values may vary for other harvester configurations. It can be observed from the figure that voltage increases monotonically with increasing load resistance along with a shift in resonance frequency. The numerical model predicts a maximum voltage of 1.56 V at 46.2 Hz for the short-circuit condition and predicts a maximum voltage of 92.3 V at 48.5 Hz for the open-circuit condition. The analytical model predicts the short and open-circuit frequencies to be 45.7 Hz and 48.2 Hz respectively. In the analytical model, the resonance frequency at the short-circuit condition is obtained from an electrically uncoupled equation, and the resonance frequencies for other load resistances are inferred from the voltage or vibration FRF. In the monolithic numerical model, the resonance frequency for any value of load resistance can directly be obtained by solving the rational eigenvalue problem in Eq. (3.37) without the need to infer these values from the FRFs. Figs. 3.3(b), 3.3(c) and 3.3(d) show the evolution of velocity with time for the same three values of resistance when the harvester is excited at the respective resonant frequencies. It can be observed from the figures that the steady-state time domain results for the voltage output are consistent with the FRF obtained from the frequency domain analysis. The numerical results are quite close to the analytical results obtained with Euler-Bernoulli beam model and also experimental results reported in [36]. The differences in the resonance frequencies in the comparison could be attributed to the different modeling approaches.

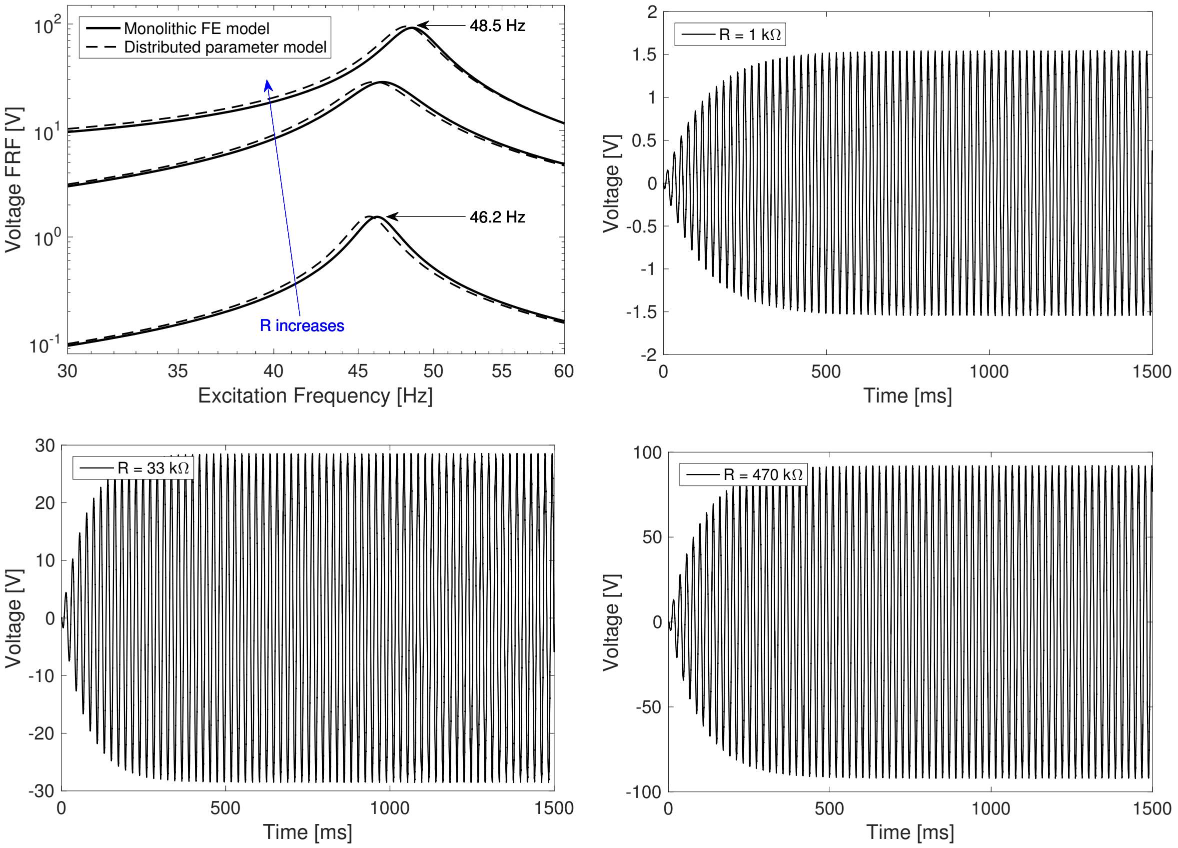

Figure 3.3: **a** Comparison of the finite element and distributed parameter voltage FRFs for three different values of load resistance–series connection, **b** voltage versus time (1 kΩ), **c** voltage versus time (33 kΩ) and **d** voltage versus time (470 kΩ)

Figure 3.4(a) compares the power FRFs obtained from the finite element model and the distributed parameter model for the same three resistive loads. Unlike the voltage output, the power output neither increases nor decreases monotonically for increasing resistive loads but the values intersect with each other. The time evolution of the power output is given in Figs. 3.4(b), 3.4(c) and Fig. 3.4(d).

The influence of different resistive loads on the vibration amplitude of the harvester can be observed in 3.5(a). The tip displacement amplitude is damped with changing load resistance for excitation below the short-circuit frequency, but the amplitude increases with changing load resistance near the open-circuit frequency. This is a strong indication that the influence of resistive loads on the vibration characteristics of the harvester is much more complex than a mere viscous damping effect. In other words, it cannot be said that higher values of resistive loads will increasingly damp the structural vibrations. This behavior is also captured with the time domain formulation and can be seen in Figs. 3.5(b), 3.5(c) and 3.5(d).

3.5.1.1 Electric Potential: Quadratic Approximation

In the model proposed in [36], the electrical field is assumed to be uniform in the thickness direction with linear approximation of the electric potential. The same assumption is found in many conventional

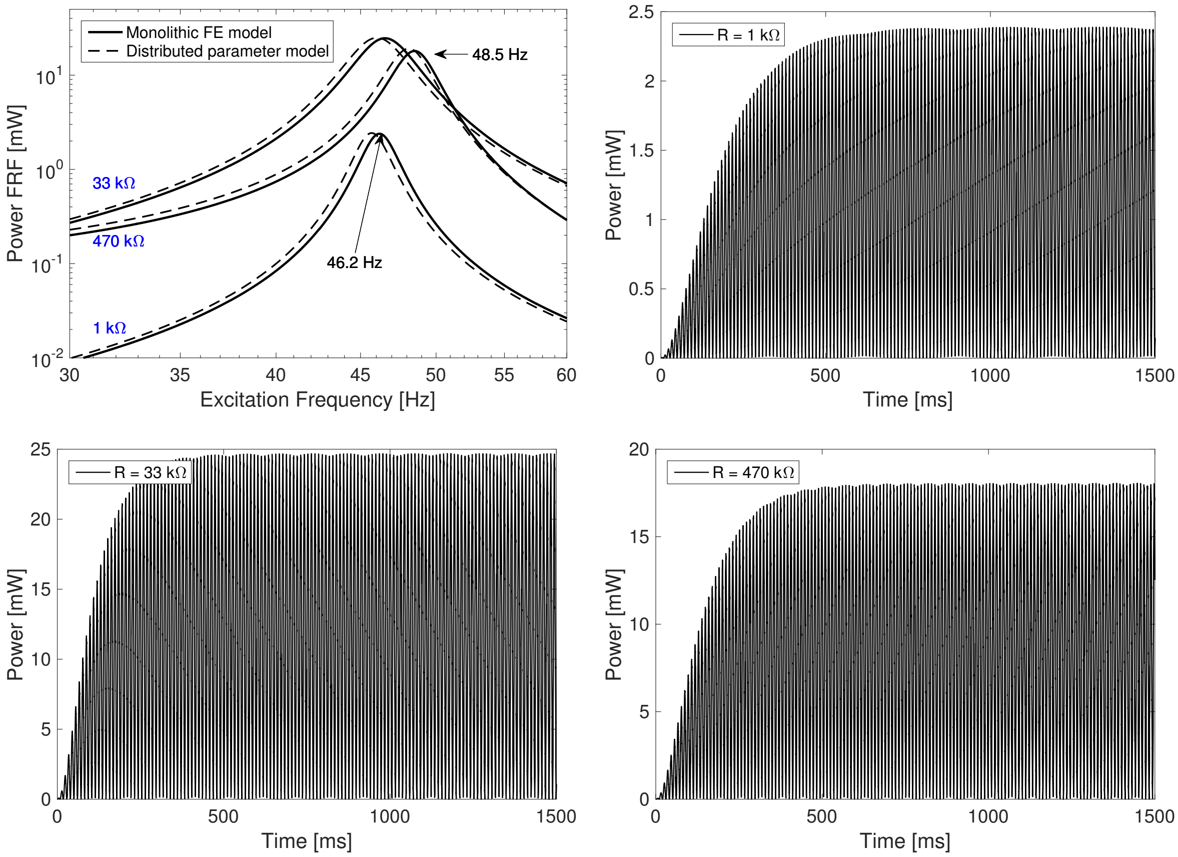

Figure 3.4: **a**Comparison of the finite element and distributed parameter power FRFs for three different values of load resistance–series connection, **b** power versus time (1 kΩ), **c** power versus time (33 kΩ) and **d** power vs time (470 kΩ)

models [11, 33] as well. The electromechanical coupling is only partial if the potential is assumed to vary linearly through the thickness [39]. Yang [51] investigated the bending of a plate with piezoelectric actuators and showed that a quadratic approximation of electric potential is necessary in bending related problems. Sze and Yang presented a finite element formulation with assumed electric displacement to overcome the effect of linear interpolation of electric potential [73]. In our finite element model, quadratic approximation of the electric potential in the thickness direction is achieved by increasing the density of the mesh.

To illustrate why quadratic approximation is necessary, let us consider the short-circuit condition of the bimorph harvester (1 kΩ). Two simulations are performed by varying the number of elements discretizing the thickness direction of the harvester as shown in Table 3.2. The number of elements in the length and width directions are kept the same. Both the simulations are performed for a time period of 80 ms with 200 time steps. Fig. 3.6 shows the voltage output of the first simulation. It can be observed that the potential varies quadratically through the thickness. In the bottom piezoelectric layer, the potential varies from 0 V at the bottom (due to electrical Dirichlet boundary condition), reaches a peak of almost 10 V and reduces to near zero at the interfaces. The same trend can be observed in the top piezoelectric layer indicating that the electrical field is not uniform through the thickness of the piezoelectric patches. Fig. 3.7 shows the voltage output for the second simulation performed with one element per piezoelectric layer. As expected, one element per piezoelectric patch cannot capture the quadratic variation of the potential through the thickness.

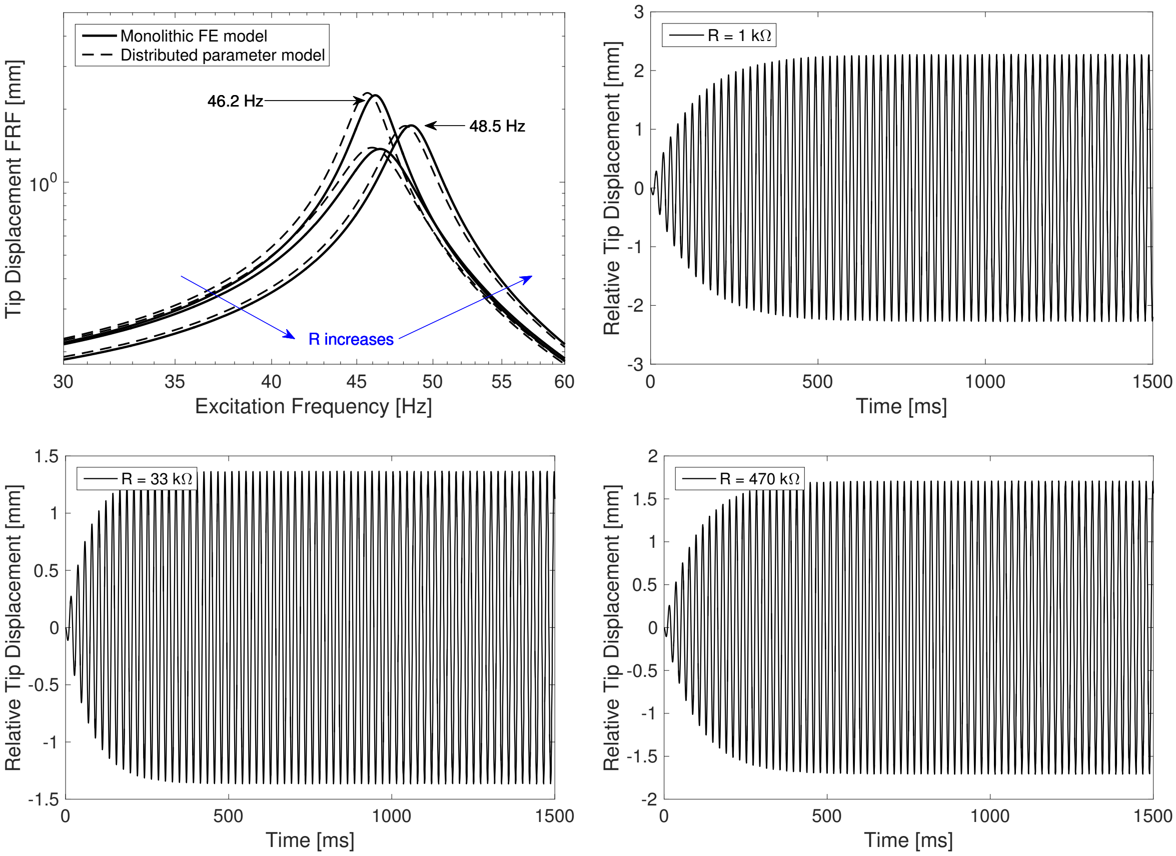

Figure 3.5: **a** Comparison of the finite element and distributed parameter tip displacement FRFs for three different values of load resistance–series connection, **b** tip displacement versus time (1 kΩ), **c** tip displacement versus time (33 kΩ), **d** tip displacement versus time (470 kΩ)

The quadratic distribution of the electric potential in the thickness direction is due to the strongly coupled nature of the problem. In this short-circuit scenario, we are basically forcing the voltage output across the top and bottom electrodes to be zero. Both in experiments and in simulations, assuming zero resistance is impossible. Hence, there will be very low voltage output across the top electrode of the harvester (the voltage in the bottom electrode is exactly zero). When the harvester is excited, some voltage will be induced in the harvester due to the electromechanical coupling. This induced voltage can only be captured if the potential is approximated quadratically. Nevertheless, the global responses from both the simulations are found to be the same. In other words, the global voltage output, power output, and the vibration response of the harvester did not significantly change irrespective of how the potential was approximated through the thickness of the piezoelectric layers. It can be hypothesized that for thin harvesters both approximations will yield the same global response, but only quadratic approximation can capture local responses accurately. Similar conclusion was reached by Wang [41]. He presented a finite element model with each element divided in a number of finite sub-layers and a linear through-the-thickness approximation of the potential in each sublayer. In [41], the potential along the length of each sublayer was assumed to be the same (equipotential condition). Equipotential condition is imposed by the presence of conducting electrodes, and the constraint is not justified in the absence of conducting electrodes.

Table 3.2: Mesh density for two simulations

Elements	Simulation 1	Simulation 2
Number of elements (length)	25	25
Number of elements (height) (PZT-5A)	6	1
Number of elements (height) (brass)	3	3
Number of elements (width)	1	1

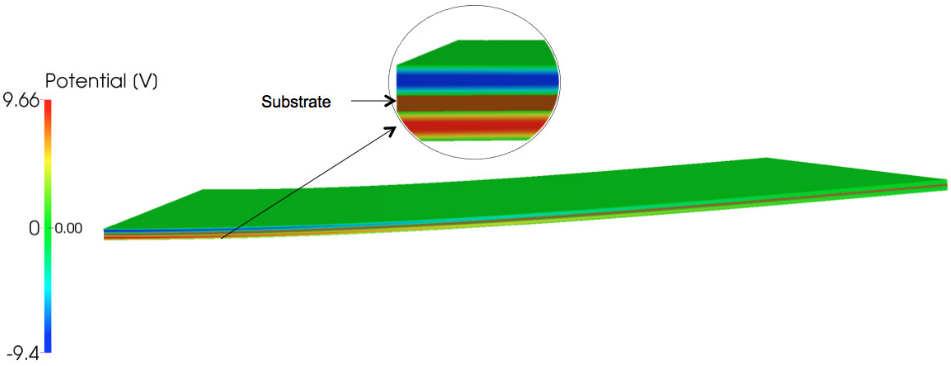

Figure 3.6: Simulation 1: Quadratic variation of electric potential through the thickness

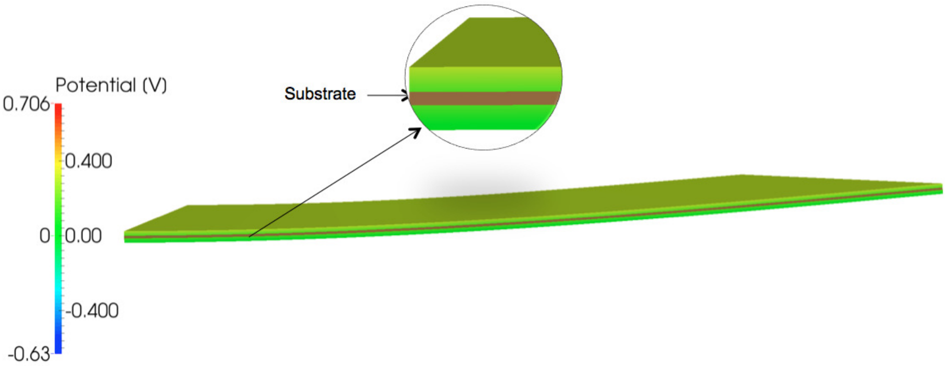

Figure 3.7: Simulation 2: Linear variation of electric potential through the thickness

3.5.2 Unimorph Harvester: Effect of Electrode Configuration

The dynamic strain distribution over the length of an energy harvester influences the electric displacement field induced in the harvester. According to Gauss' law, the total charge on the electrode area is the integral of the electric displacement over the area of the conducting electrode covering the piezoelectric patch. Thus, the strain distribution influences the total charge collected on the electrodes. When a cantilevered energy harvester vibrates in a mode other than the first mode, the dynamic strain distribution changes sign over certain points (strain nodes). Erturk et al. [22] experimentally demonstrated that covering the strain nodes with continuous electrodes will drastically reduce the electrical outputs of a harvester and suggested using segmented electrodes to mitigate the effects. Friswell and Adhikari [20] investigated the effects of electrode topology on a unimorph harvester vibrating in the first mode and connected to a load resistance of 100 kΩ. In their study the power output increased 115% when the electrode covered approximately half the piezoelectric material.

In this example we examine the effect of electrode configuration on energy harvested from a cantilevered unimorph harvester without proof mass. The properties of the harvester, as given in [34], are listed in Table 3.3. For this harvester configuration, 100 Ω is close to the short-circuit condition and 10^6 Ω is close to the open-circuit condition. Equation (3.37) predicts the first two natural frequencies of the harvester at the short-circuit condition to be 48.07 Hz and 302.03 Hz respectively. The first two natural frequencies at the open-circuit condition are predicted to be 49.0 Hz and 304.15 Hz respectively. These frequencies are calculated assuming that the electrode is fully covering the piezoelectric layer. The proportional damping coefficient for the first mode is determined to be 0.006040 rad ms^{-1} from the damping ratio given in [34]. The harvester is accelerated at $1g$ ($g = 9.81$ $\mathrm{m/s^2}$)

Table 3.3: Geometric and material properties of the unimorph EHD

Quantity	Dimension	Value
Length of the beam	l (mm)	100
Width of the beam	b (mm)	20
Thickness of the piezo. patch (PZT-5A)	h_p (mm)	0.4
Thickness of the substructure	h_s (mm)	0.5
Young's modulus of the substructure (brass)	Y_s (GPa)	100
Young's modulus of PZT-5A	Y_p (GPa)	66
Mass density of the substructure (brass)	ρ_s $\left(\mathrm{Kgm^{-3}}\right)$	7165
Mass density of PZT-5A	ρ_p $\left(\mathrm{Kgm^{-3}}\right)$	7800
Piezoelectric displacement coefficient	d_{31} $\left(\mathrm{pmV^{-1}}\right)$	−190
Permittivity	$\varepsilon_{33}^{\mathbf{S}}$ $\left(\mathrm{nFm^{-1}}\right)$	15.93

To asses the effects of the electrode length on the power generated when the harvester is vibrating in the first mode, the length of the electrode is increased from the clamped end of the harvester. In the numerical model, change in electrode length is implemented by discretizing the electrode with surface elements only to the extent of the electrode coverage. Consequently, the equipotential condition is valid only to the extent of the electrode coverage over the piezoelectric layer. For each change in the length of the electrode, the harvester is tested for a range of resistive loads (between 100 Ω and 10^6 Ω). For each resistive load, the harvester is excited at its resonance frequency calculated from Eq. (3.37) for that particular load and assuming full coverage of the electrode. The result of this investigation is shown in Fig. 3.8.

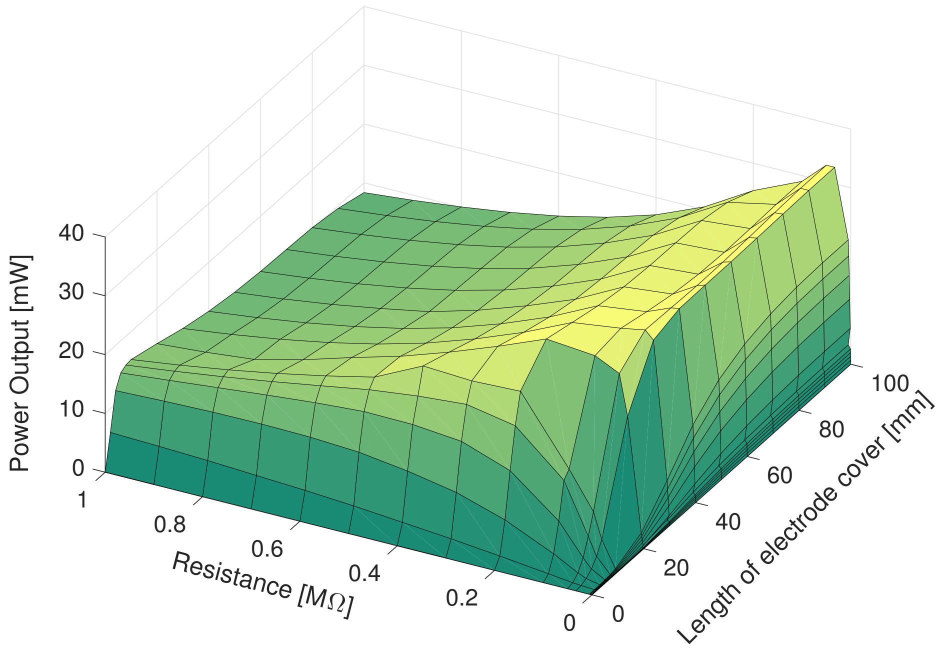

Figure 3.8: Influence of electrode length on the power dissipated. The length of the electrode is increased from the clamped end

The simulation results indicate that for low resistive loads, maximum power output is obtained when the electrode covers the piezoelectric layer completely. For the range of resistances considered in this example, a maximum power output of 32.81 mW is achieved for a resistive load of 50 kΩ when the electrode is fully covering the piezoelectric layer. However, when the resistive load is increased beyond a certain extent, shortening the electrode length improves the power generated. For the open-circuit condition, the numerical model predicts 8.3 mW power output when the electrode is fully covering the piezoelectric layer. The power output increases to 15.2 mW when the electrode covers only 20 mm from the clamped end, suggesting an increase of 83% in the power generated.

It is pertinent to mention that changing the electrode length will affect the dynamics of the structure. Let's take the resistive load of 10 kΩ for example. When the electrode is fully covering the piezoelectric layer, the numerical model predicts the first resonance frequency of the harvester to be 48.13 Hz. However, when the electrode covers only 10 mm of the harvester the frequency changes to 49.07 Hz. Although this change is not accounted for in Fig. 3.8 for fair comparison, one must be aware that the resonance frequency changes with the change in the electrode configuration. Fig. 3.9 shows the change in the first two resonant frequencies of the harvester with the change in electrode length for the 10 kΩ resistive load.

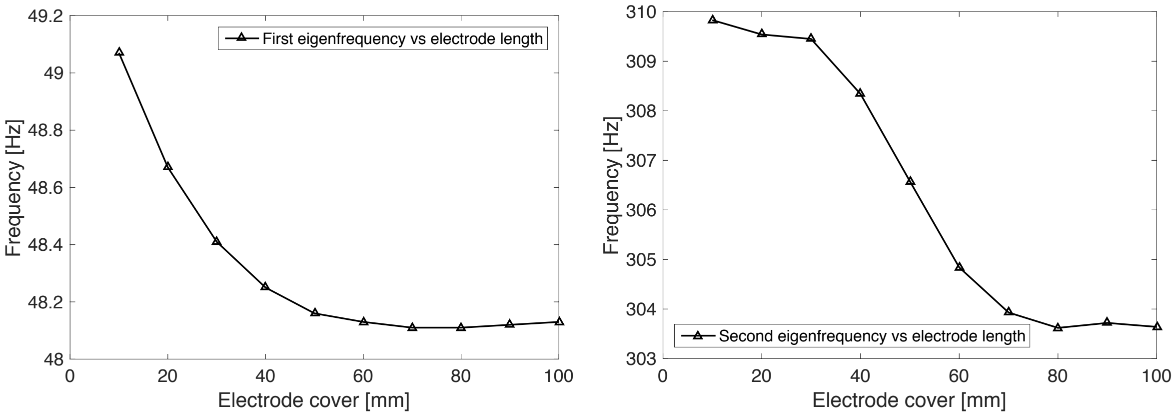

Figure 3.9: **a** Change in the first resonant frequency with change in the electrode length for 10 kΩ and **b** change in the second resonant frequency with change in the electrode length for 10 kΩ

Accounting for this change in frequencies will not affect the general trend presented in Fig. 3.8. However, for the resistive loads considered, the power output obtained at shorter electrode lengths will be higher due to the increase in resonance frequencies at shorter lengths.

Remark Shortening the length of the electrode cover is distinctly different from shortening the length of the piezoelectric layer. Shortening the length of the piezoelectric layer will affect significantly the natural frequencies of an energy harvester. In the example considered, the piezoelectric layer length is a constant 100 mm for all the simulations performed. Only the electrode length is varied in order to simplify the numerical investigation.

3.5.2.1 Effect of Strain Node

To demonstrate the effect of strain node on the power output of the harvester, we now consider the second bending mode of the unimorph harvester. For cantilevered beams, a vibration mode r has $r-1$ strain nodes. Hence, the first bending vibration mode of the unimorph harvester has no strain nodes, and the second bending vibration mode of the harvester has one strain node. The position of the strain node over the length of a cantilevered beam without proof mass, for the second vibration mode, is $0.2165l$ [22]. Hence, the second bending mode of the harvester has one strain node at 21.65 mm from the clamped end.

Simulations are performed for three different electrode configurations. In the first configuration, the electrode covers the patch completely. In the second configuration, the electrode covers the first 20 mm of the structure, just short of the strain node. In the third configuration, the electrode cover extends from 25 mm till the end of the structure ($25 \leq x \leq 100$). In all three simulations, a resistive load of 10 kΩ is considered. The second resonant frequency of the harvester—assuming full coverage of the electrode—for the 10 kΩ resistive load is 303.64 Hz (Fig. 3.9(b)), and the harvester is excited at this frequency in all three simulations. The proportional damping coefficient for the second vibration mode is 0.0496 rad ms^{-1} based on the damping ratio value in in [22].

Figure 3.10 shows that a steady-state voltage of 2.48 V is obtained, from the second vibration mode of the harvester, for the first configuration. The maximum power output (V^2/R) obtained for the first configuration is 0.6201 mW.

Figure 3.10: Steady-state voltage output for full coverage of the electrode

A steady-state voltage of 1.41 V is obtained for the second configuration as shown in Fig. 3.11, and the maximum power output obtained for this configuration is approximately 0.21 mW. Unlike the first configuration, the equipotential condition in this configuration exists only for the first 20 mm of the beam. Only the region covered by the electrode contributes to the power output. This is the reason why assuming equipotential condition in the absence of conducting electrodes is not justified.

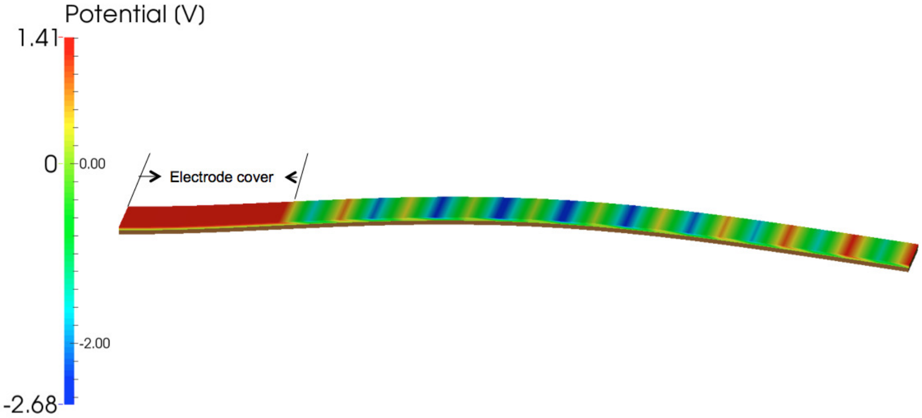

Figure 3.11: Steady-state voltage output for 20 mm coverage of the electrode

For the last configuration, where the electrode covers the region $25 \leq x \leq 100$, Fig. 3.12 shows that the steady-state voltage is 2.69 V. The maximum power output for the third configuration is 0.73 mW.

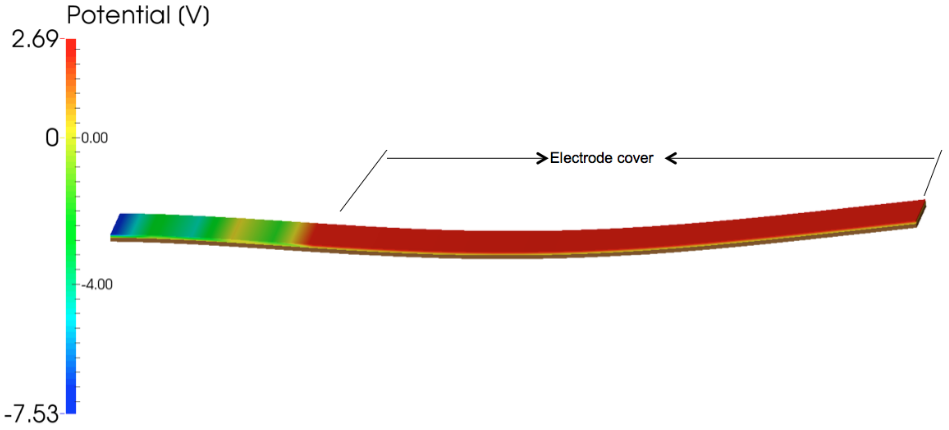

Figure 3.12: Steady-state voltage output for 75 mm coverage of the electrode (75 mm from the free end)

From the results it is clear that the third configuration yields the highest power output among the three configurations considered—a 15% increase in power output compared to the first configuration and a 247% increase compared to the second configuration. The reason is obvious. As the dynamic strain distribution changes sign at the strain node, full coverage of the electrode will lead to a reduction in the total charge obtained due to the cancellation of the positive and negative areas under the curve when integrating the dielectric displacement over the electrode area. Thus, in the first configuration only a small portion of the electrode area contributes towards the electrical outputs, whereas in the third configuration 75% of the electrode area contributes towards the electrical outputs. The power output can further be increased by combining configurations two and three (segmenting the electrode at the strain node). Since the frequency of excitation (303.64 Hz) is kept constant in all three simulations, only the first configuration is excited at resonance. The other two configurations are excited near their resonance frequencies due the the change in resonance frequencies with change in electrode length.

3.6 Summary and Conclusions

A monolithic mixed-hybrid finite element model is proposed to model piezoelectric energy harvesting devices. Both time domain and frequency domain analyses based on the monolithic model are presented. One of the significant advantages of the proposed model is that it enables to calculate the natural frequencies of a given harvester for any finite value of resistive load. The numerical results are compared with the analytical results reported in the literature for a bimorph harvester with tip mass and series connection of piezoelectric layers. Through the bimorph example it is shown that the nonlinear induced potential can be accurately captured by increasing the number of elements in the thickness direction. The nonlinear induced potential, at least of the short-circuit condition considered, is insignificant and the global responses can be predicted by linear through-the-thickness approximation of the electric potential. To demonstrate the influence of electrode configuration on the power output of an harvester, a unimorph energy harvester is considered. Results indicate that shortening the electrode length improves the power output for higher resistive loads, whereas the power output for low resistive loads is maximum when the electrodes are fully covering the piezoelectric patch. The effect of strain node on the power output is also demonstrated for the unimorph harvester.

The proposed numerical model is not restricted by the considerations of the geometry of a harvester and can be used to model energy harvesters with complex geometries. Energy harvesting from piezoelectric materials is very similar to using piezoelectric materials for structural damping. Hence, the proposed model can also be used for piezoelectric shunt damping applications without any major changes to the formulation. The choice of structural velocities for the mechanical part and electric potential rate for the electrical part, as primary assumed field variables, may seem offbeat at first glance. The overarching goal, although not touched upon here, is to include fluid domain in the monolithic model proposed here. In this context, the choice of velocity as the assumed variable seems only natural as this enables native coupling of the formulation with the fluid domain. The idea was first proposed by the authors in [62].

Chapter 4

Analysis of Flow-Driven Piezoelectric Energy Harvesters

Abstract

This chapter presents a monolithic finite element solution approach for fluid-structure interaction problems in the context of flow-driven piezoelectric energy harvesting. Flow-driven piezoelectric energy harvesting is a strongly coupled multiphysics phenomenon that involves complex three-way interaction between the fluid flow, the electromechanical effect of the piezoelectric material and the controlling electrical circuit. High fidelity computational solution approaches are essential for the analysis of flow-driven energy harvesters in order to capture the main physical aspects of the coupled problem and to accurately predict the power output of a harvester. There are some phenomenological and numerical models for flow-driven harvesters reported in the literature; however, a fully three-dimensional strongly coupled model has not yet been developed, especially in the context of flow-driven energy harvesting. A monolithic numerical solution method that provides consistent and simultaneous solution to all physical fields, while taking into account the three-way coupling of the fields, is presented in this chapter. The approximate solution is based on a mixed-hybrid three-dimensional space-time finite element formulation with static condensation of the auxiliary fields. Discontinuous Galerkin method (DG method) is utilized for integrating the monolithic model in time. The proposed solution scheme is illustrated in the example of a lid driven cavity with a flexible piezoelectric bottom wall.

4.1 Introduction

Flow in and around engineering structures may elicit various responses from the structures, such as vortex-induced vibrations, flutter, and galloping. These responses may become dangerous and destructive. In many civil engineering applications, methods are often sought to avoid these dangerous interactions of a structure with the surrounding fluid. The perspective in flow-driven energy harvesting is to use the available flow energy through controlled hydro or aeroelasticity phenomena and harness potentially harmful fluctuations to provide power supply to low power electronic devices. In flow-driven piezoelectric energy harvesting, the dynamic strain induced in the piezoelectric material by the kinetic energy of the fluid is transformed into electrical energy through direct piezoelectric effect.

Recent surveys [1, 52–54] on energy harvesting from piezoelectric material show that studies have predominantly focused on harvesting energy from vibrations of the structure to which the piezoelectric harvester is attached. Experimental and theoretical studies on piezoelectric energy harvesting from the kinetic energy of fluid is limited. Allen and Smits [24] experimentally studied the behavior of slender piezoelectric eel-like strips placed behind a bluff body. Their study was continued by Techet et at. [25], where multiple eels made of PVDF were stacked vertically behind a single bluff body to study the energy harvesting capabilities of the piezoelectric strips. A similar study on energy harvesting eels placed in the wake of a bluff body was carried out by Taylor et al. [26]. Kármán vortex sheets generated by bluff bodies placed in wind flows have also been utilized to study energy harvesting capabilities of piezoelectric energy harvesters. Wind energy can be used to create flapping of flag-like membranes with piezoelectric materials in a unimorph or bimorph configuration. Robbins et al. [28] performed experiments for generating electrical energy from piezoelectric materials placed in wind flow. Erturk et al. [4] conducted experiments on energy harvesting from flow-excited morphing airfoils. In a similar study, Anton and Inman [31] investigated the possibility of harvesting vibration energy and solar energy from a mini unmanned air vehicle (UAV). They reported that the piezoelectric patches were able to harvest enough power to fully charge a small battery when the volume of the piezoelectric material was increased. The above mentioned references are some of the frequently cited experimental studies on flow-induced energy harvesting.

On the mathematical modeling front, a variety of modeling approaches have been proposed to analyze piezoelectric energy harvesters placed in wind flow. Erturk et al. [55] presented a mathematical model for analyzing energy harvesting potential of piezoaeroelastic systems. They presented a frequency domain analysis of wing-based piezoaeroelastic harvester. De Marqui et al. [56] presented a time domain piezoaeroelastic model for airflow excitation of cantilever plates representing wing-like structures with embedded piezoelectric material for continuous and segmented electrode configurations. Their piezoaeroelastic model was a combination of electromechanically coupled finite element model [42] and an unsteady vortex-lattice aerodynamic model. These modeling approaches are application specific. For example, the model proposed in [55] is a lumped parameter wing-section model and can be used to analyze power output of a harvester placed on the wing section of an unmanned air vehicle. Akaydin et al. [58] explored energy harvesting from unsteady turbulent flow using piezoelectric materials, where the action of turbulent boundary layers and wakes of circular cylinders at high Reynolds number on piezoelectric cantilever beams was investigated. They used FLUENT software to analyze the three-way interaction accounting for the aerodynamics, structural vibration, and the electrical response of the piezoelectric material. Navier-Stokes equation was used to model the incompressible flow field, and the piezoelectric beam was modeled as a single degree of freedom system. SDOF models are limited to a single vibration mode and cannot accurately predict the power output of a harvester [34]. Mehmood et al. [6] presented a numerical model, where the governing equations were solved simultaneously and the coupling was based on Hamming fourth-order predictor-corrector technique. More recently Amini et al. [59] presented a more comprehensive numerical model for analyzing piezoelectric energy harvesting from fluid-structure interactions. Their numerical model was a combination of openFOAM solver for fluid domain and finite element method for the piezoelectric material. The finite element model was based on Euler–Bernoulli approximations with linear through-the-thickness approximation of the electric potential. The model was validated against the results from the model proposed by Akaydin et al. [58]. The model proposed in [59] is more comprehensive than the model proposed in [58].

Numerical modeling of piezoelectric energy harvesting from fluid flow is still a very challenging task due to the strongly coupled three-way information exchange between the different domains; in order to solve for the deformation of the structure and the power generated for a given load resistance, the loading from the fluid flow must first be determined. However, the fluid loads cannot be determined without the information of the structural deformation and the influence of the electric load on this deformation. The models proposed by both Akaydin et al. [58] and Amini et al. [59] follow a partitioned approach with different discretization schemes for the fluid domain and the piezoelectric structure. In partitioned approaches, strong coupling can be achieved by iterated solution of the subsystems with additional computational effort. In [58], the authors themselves suggested strongly coupled three-dimensional approach as an improvement to their proposed model.

This research work proposes a simultaneous solution to the coupled system, where the deformation of the structure, fluid flow, and the electrical outputs are solved simultaneously in time. Simultaneous solution methods are preferable for strongly coupled problems to ensure stability and accelerated convergence [7]. In this approach, the weak form of the governing equations of the fluid, the piezoelectric structure and the electrical circuit is formulated as a single equation and solved simultaneously, along with the fluid mesh movement within a single iteration loop. The coupled system is uniformly discretized by time-discontinuous stabilized three-dimensional space-time finite elements, leading to a monolithic solution framework. The 3D continuum approach enables application of piezoelectric constitutive laws without any simplifying assumptions, leading to an exact fulfillment of Gauss law for bending problems. Three-dimensional modeling approach also enables modeling of anisotropic behavior of materials and modeling of coupled bending-torsion harvesters. The ability of the proposed formulation to model flow-driven piezoelectric harvesters is illustrated through the example of a driven cavity with flexible piezoelectric bottom wall.

4.2 Model Equations

The strong form of equations governing the behavior of a generic flow-driven piezoelectric energy harvester are given in this section. The coupled system consists of a piezoelectric unimorph structure placed in a flow field and a resistive load coupled to the electrodes covering the top and bottom surfaces of the piezoelectric layer. The flow field is viscous and incompressible and described using the balance equations. The equations of the flow field are time-dependent and accommodates moving boundaries resulting from structural deformations. The behavior of the piezoelectric structure is materially and geometrically linear.

Fluid Dynamics The balance equations consisting of momentum balance and continuity equation are described using an Eulerian framework in the moving space-time domain $Q_f = \Omega_f \times [t_a, t_b]$. The momentum balance equation is given by

$$\rho(\frac{\partial \vec{v}}{\partial t} + \vec{v} \cdot \nabla \vec{v}) - \nabla \cdot \mathbf{T} - \vec{f} \ = \vec{0} \quad \text{in} \quad Q_f, \tag{4.1}$$

and the incompressibility constraint on the velocity field is given by

$$\nabla \cdot \vec{v} \ = 0 \quad \text{in} \quad Q_f, \tag{4.2}$$

where $\vec{v}$ is the velocity of the fluid, $\vec{f}$ is the body force, ρ is the density of the fluid, and $\mathbf{T}$ is the Cauchy stress tensor. The constitutive relation is expressed as

$$\mathbf{T} - 2\mu \mathbf{D}(\vec{v}) + p\mathbf{I} \ = \mathbf{0} \quad \text{in} \quad Q_f, \tag{4.3}$$

where μ is the viscosity of the fluid, p is the hydrostatic pressure, and $\mathbf{D}$ is the linear strain rate tensor given by

$$\mathbf{D}(\vec{v}) - \frac{1}{2}(\nabla \vec{v} + (\nabla \vec{v})^\top) \ = \mathbf{0} \quad \text{in} \quad Q_f. \tag{4.4}$$

Dirichlet and Neumann boundary conditions

$$\vec{v} - \bar{\vec{v}} \ = 0 \quad \text{on} \quad P_f^v \qquad \text{and} \qquad \vec{t} - \bar{\vec{t}} \ = 0 \quad \text{on} \quad P_f^t, \tag{4.5}$$

are defined on the space-time boundary $P_f = \Gamma_f \times [t_a, t_b]$ of the fluid domain, where $\bar{\vec{v}}$ and $\bar{\vec{t}}$ are velocities and tractions, respectively, imposed on boundary subsets. The divergence-free velocity state at time $t = 0$ is defined by the initial condition

$$\vec{v}(t = 0) = \vec{v}_i \quad \text{with} \quad \nabla \cdot \vec{v}_i = 0 \quad \text{on} \quad \Omega_f. \tag{4.6}$$

Piezoelectric Structure For the piezoelectric structure occupying a space-time domain $Q_p = \Omega_p \times [t_a, t_b]$, the rate form of the direct and inverse constitutive equations may be expressed as

$$\dot{\mathbf{S}} - [s^{\vec{D}}]\dot{\mathbf{T}} - [g]^\top \dot{\vec{D}} = \mathbf{0} \quad \text{in} \quad Q_p, \tag{4.7}$$

$$\dot{\vec{E}} - [g]\dot{\mathbf{T}} - [\varepsilon^{\mathbf{T}}]^{-1}\dot{\vec{D}} = \vec{0} \quad \text{in} \quad Q_p, \tag{4.8}$$

where $\mathbf{T}$ is the Cauchy stress tensor, $\mathbf{S}$ is the strain tensor, $\vec{E}$ is the electric field vector, $\vec{D}$ is the vector of electrical displacements, $[s^{\vec{D}}]$ is the elastic compliance matrix measured at constant electrical displacement, $[g]$ is the matrix of piezoelectric coupling coefficients in strain-voltage form, and $[\varepsilon^{\mathbf{T}}]$ is the dielectric matrix measured at constant stress. $\mathbf{S}$ and $\vec{E}$ are energy conjugates of $\mathbf{T}$ and $\vec{D}$, respectively.

The conservation of linear momentum of the piezoelectric structure for small deformations is expressed as

$$\rho\dot{\vec{v}} - \nabla\cdot\mathbf{T} - \vec{f} = \vec{0} \quad \text{in} \quad \Omega_p, \tag{4.9}$$

where ρ denotes the mass density of the piezoelectric structure, $\vec{v}$ denotes the vector of piezoelectric structural velocities, and $\vec{f}$ the vector of body forces. The gradient relation between the linear strain rate tensor and the velocity is expressed as

$$\dot{\mathbf{S}} - \frac{1}{2}[\nabla\vec{v} + (\nabla\vec{v})^{\top}] = \mathbf{0} \quad \text{in} \quad \Omega_p. \tag{4.10}$$

The fundamental equations describing the electrostatic behavior of the piezoelectric structure is given by

$$\nabla\cdot\vec{D} = 0 \quad \text{in} \quad \Omega_p, \tag{4.11}$$

$$\dot{\vec{E}} + \nabla\psi = \vec{0} \quad \text{in} \quad \Omega_p, \tag{4.12}$$

where Eq. (4.11) is the differential form of Gauss' law and Eq. (4.12) describes the gradient relation between the electric field rate $\dot{\vec{E}}$ and the electric potential rate ψ. The mechanical Dirichlet and Neumann boundary conditions

$$\vec{v} - \bar{\vec{v}} = 0 \quad \text{on} \quad P_p^v \qquad \text{and} \qquad \mathbf{T}\cdot\vec{n} - \bar{\vec{t}} = 0 \quad \text{on} \quad P_p^t, \tag{4.13}$$

are defined on the space-time boundary $P_p = \Gamma_p \times [t_a, t_b]$ of the piezoelectric structure, where $\bar{\vec{v}}$ and $\bar{\vec{t}}$ are velocities and tractions, respectively, imposed on boundary subsets.

Electrodes Piezoelectric materials are typically covered on their top and bottom surfaces with conducting electrodes as they are essential for applying electrical boundary conditions. Electric charges are collected on the electrodes, and electric voltage can be applied only through the electrodes. The electrodes are equipotential surfaces and very thin compared to the thickness of the piezoelectric layer. Let the electroded part of the boundary P_p of the piezoelectric structure considered here be P_p^{ψ} and the non-electroded part of the boundary P_p be P_p^q. The electrical Dirichlet boundary conditions imposed on the electroded part are given by

$$\psi_+ - \psi = 0 \quad \text{on} \quad P_u^{\psi}, \tag{4.14}$$

$$\psi_- - \psi = 0 \quad \text{on} \quad P_l^{\psi}, \tag{4.15}$$

where P_u^{ψ} and P_l^{ψ} denote the upper and lower electrode boundaries, respectively. Also, ψ_+ and ψ_- denote the electric potential rate imposed on the upper and lower electrodes, respectively. The electrical Neumann boundary condition, applied on the non-electroded part of the piezoelectric structure is expressed as

$$\vec{D}\cdot\vec{n} + \bar{q} = 0 \quad \text{on} \quad P_p^q, \tag{4.16}$$

where $\bar{q}$ is the free charge density per unit surface area. We assume the free charge density in this case to be zero on the non-electroded surfaces. The mechanical effects on the electrodes can be neglected because of their relatively small thickness. The spatially constant time-dependent electric potential developed between the upper and lower electrodes due to the strains developed in the piezoelectric layer can be expressed as

$$\dot{\phi} = \psi_+ - \psi_- \quad \text{on} \quad P_p^\psi. \tag{4.17}$$

It is typical in piezoelectric energy harvesting applications to set the potential in one of the electrodes to zero (ground) and let the other electrode unconstrained for floating potential to develop. If we consider the electrode covering the bottom surface to be grounded, Eq. (4.15) may be expressed as

$$\psi_- = \psi \ \ = 0 \quad \text{on} \quad P_l^\psi. \tag{4.18}$$

The total free electric charge Q_e on the electrodes P_u^ψ and P_l^ψ can be expressed as

$$Q_e = \int_{P_u^\psi} q_+ \, \mathrm{d}P = -\int_{P_l^\psi} q_- \, \mathrm{d}P. \tag{4.19}$$

Electrode-Circuit Coupling As mentioned earlier, we consider a resistive load coupled to the electrodes of the piezoelectric structure. For a resistive circuit, Ohm's law relates the current through a conductor between two terminals and the voltage developed across as the two terminals

$$\phi - R \cdot I = 0, \tag{4.20}$$

where R is the resistance offered by the conductor. Since the resistive load is directly connected to the electrodes covering the piezoelectric layer, the potential developed across the electrodes is equal to the potential across the resistive circuit. Thus, the current flowing out of the upper electrode is given by

$$I = -\dot{Q}_e. \tag{4.21}$$

Substituting Eqs. (4.19) and (4.20) in Eq. (4.21), the coupling between the electrodes the circuit is obtained as

$$\frac{\phi}{R} + \int_{\Gamma_u^\psi} \dot{q}_+ \, \mathrm{d}\Gamma_p. \tag{4.22}$$

Elastic Structure For the linear elastic structure at small deformations occupying s space-time domain $Q_s = \Omega_s \times [t_a, t_b]$ with boundary $P_s = \Gamma_s \times [t_a, t_b]$, the governing equations are essentially the same as the governing equations for the piezoelectric layer but without the electrical variables. The equations can be summarized as

$$\dot{\mathbf{S}} - [s]\dot{\mathbf{T}} = \mathbf{0} \quad \text{in} \quad Q_s, \tag{4.23}$$

$$\rho\dot{\vec{v}} - \nabla \cdot \mathbf{T} - \vec{f} = \vec{0} \quad \text{in} \quad Q_s, \tag{4.24}$$

$$\dot{\mathbf{S}} - \frac{1}{2}[\nabla\vec{v} + (\nabla\vec{v})^\top] = \mathbf{0} \quad \text{in} \quad Q_s. \tag{4.25}$$

$$\vec{v} - \bar{\vec{v}} = \vec{0} \quad \text{on} \quad P_s^v, \tag{4.26}$$

$$\mathbf{T} \cdot \vec{n} - \bar{\vec{t}} = \vec{0} \quad \text{on} \quad P_s^t. \tag{4.27}$$

Here, $[s]$ is the elastic compliance matrix for the structure, ρ is the structural density, $\mathbf{T}$ is the Cauchy stress tensor, and $\mathbf{S}$ is the strain tensor.

Fluid-Elastic/Piezo Coupling The flow domain is coupled with the elastic structural domain along the space-time fluid-structure/piezo interface $P_c = \Sigma \times [t_a, t_b]$, where P_c is defined on the current configuration (Eulerian frame of reference). At this space-time boundary P_c, the continuity of the structural and fluid velocities must be enforced for geometrical conservation. This enforcement may be expressed as

$$\vec{v}_f - \vec{v}_{s/p} = \vec{0} \quad \text{on} \quad P_c. \tag{4.28}$$

Moreover, the momentum balance at the interface is fulfilled by ensuring that the fluid and the structural tractions are of the same magnitude and opposite in direction

$$\vec{t}_f + \vec{t}_{s/p} = \vec{0} \quad \text{on} \quad P_c. \tag{4.29}$$

4.3 Space-Time Weighted Residual Form and Discretization

4.3.1 Weighted Residual Formulation

The Galerkin weighted residual method is applied to the strong form Eqs. (4.1)–(4.29). The resulting weak formulation of the coupled system is formulated over a sequence of N space-time slabs $Q_n = \Omega_n \times [t_n, t_{n+1}]$, where Q_n is a space-time domain existing between the time intervals t_n and t_{n+1} as shown in Fig. 4.1(a). The time slabs are solved successively, and within each time step the unknown fields are solved simultaneously. The weak form is evaluated over a space-time domain Q_n, where the interpolation functions are continuous within the space-time slab but discontinuous from one time slab to another as shown in Fig. 4.1(b). The discontinuous approximation of the unknown fields in time leads to additional jump terms in the weak form, because at any time instant t_n the energy has to be equal at the end of previous time slab at t_n^- and at the beginning of the next time slab t_n^+. The DG method is an implicit time integration scheme. The time integration scheme for first order equations is A-stable and third order accurate if the temporal interpolation is linear. For references, see [7, 62, 68, 70–72].

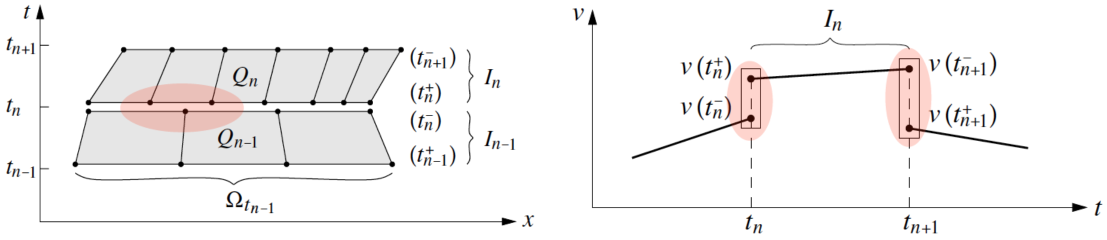

Figure 4.1: **a** Space-time domain and **b** time-discontinuous interpolation [7]

Fluid The stabilized space-time weighted residual formulation of the fluid domain in a space-time slab $Q_{f,n}$ with boundary $P_{f,n}$ is expressed as

$$\int_{Q_{f,n}} \delta\vec{v} \cdot \left(\rho\Big(\frac{\partial \vec{v}}{\partial t} + \vec{v} \cdot \nabla \vec{v}\Big) - \vec{f} \right) \mathrm{d}Q + \int_{Q_{f,n}} \mathbf{D} : 2\mu \mathbf{D} \; \mathrm{d}Q - \int_{Q_{f,n}} \nabla \cdot (\delta\vec{v}) p \; \mathrm{d}Q \tag{4.30a}$$

$$+ \int_{Q_{f,n}} \delta p \nabla \cdot \vec{v} \; \mathrm{d}Q + \int_{Q_{f,n}} \delta\vec{v}(t_n^+) \cdot \rho\big(\vec{v}(t_n^+) - \vec{v}(t_n^-)\big) \; \mathrm{d}Q \tag{4.30b}$$

$$+ \sum_e \int_{Q_{f,n}^e} \tau_M^F \frac{1}{\rho} \mathscr{D}(\delta\vec{v}, \delta p) \cdot \big(\mathscr{D}(\vec{v}, p) - \vec{f}\big) \; \mathrm{d}Q \tag{4.30c}$$

$$+ \sum_e \int_{Q_{f,n}^e} \tau_C^F \rho (\nabla \cdot \delta\vec{v}) \nabla \cdot \vec{v} \; \mathrm{d}Q \tag{4.30d}$$

$$- \int_{P_{f,n}} \delta\vec{v} \cdot \bar{\vec{t}} \, \mathrm{d}P = 0 \qquad \forall \; \delta\vec{v}, \delta p, \tag{4.30e}$$

where the differential operator

$$\mathscr{D}(\vec{v}, p) = \rho(\frac{\partial \vec{v}}{\partial t} + \vec{v} \cdot \nabla \vec{v}) - \nabla \cdot \mathbf{T} \tag{4.31}$$

refers to the strong form of momentum conservation equation (4.1) without the body force term. Equation (4.30) represents the weighted residual form of the momentum conservation. The constitutive relation for the fluid and the kinematics are fulfilled exactly in Eq. (4.30a). Equation (4.30b) is the weak form of the incompressibility constraint weighted with the fluid pressure. The last term in Eq. (4.30b) contains the jump terms required due to the discontinuous time integration, thereby ensuring the transfer of kinetic energy from end of previous time slab at t_n^- to the beginning of the next time slab t_n^+ at time t_n. Equations (4.30c) and (4.30d) are the stabilization parameters as described in Behr and Tezduyar [74]. The stabilization terms allow equal order approximations of velocities and pressure for incompressible fluid flow, and they suppress numerical oscillations in solutions to hyperbolic equations. The Neumann boundary condition is satisfied in the integral form in the last integral term, while the Dirichlet condition is applied a priori.

Piezoelectric Structure The weak form for the piezoelectric layer—including the electrodes and the circuit—is expressed in terms of six unknown field variables in a space-time setting. The Galerkin weighted residual form within the space-time slab $Q_{p,n}$ including the boundaries $P_{p,n} = \Gamma_n \times [t_n, t_{n+1}]$ is expressed as

$$\int_{Q_{p,n}} \delta\vec{v} \cdot (\rho\dot{\vec{v}} - \vec{f}) \, \mathrm{d}Q + \int_{Q_{p,n}} \delta\vec{v} \cdot \rho\gamma_r\vec{v} \, \mathrm{d}Q + \int_{Q_{p,n}} \dot{\mathbf{S}}(\delta\vec{v}) : \mathbf{T} \, \mathrm{d}Q + \int_{Q_{p,n}} \dot{\vec{E}}(\delta\psi) \cdot \vec{D} \, \mathrm{d}Q \tag{4.32a}$$

$$+ \sum_e \int_{Q^e_{p,n}} \delta\mathbf{T} : ([s^{\vec{D}}]\dot{\mathbf{T}} + [g]^\top \dot{\vec{D}} - \dot{\mathbf{S}}(\vec{v})) \, \mathrm{d}Q \tag{4.32b}$$

$$+ \sum_e \int_{Q^e_{p,n}} \delta\vec{D} \cdot ([g]\dot{\mathbf{T}} + [\varepsilon^{\mathbf{T}}]^{-1}\dot{\vec{D}} - \dot{\vec{E}}(\psi)) \, \mathrm{d}Q \tag{4.32c}$$

$$+ \int_{\Omega_{p,n}} \delta\vec{v} \cdot \Big(\rho\big(\vec{v}(t_n^+) - \vec{v}(t_n^-)\big)\Big)\mathrm{d}\Omega + \sum_e \int_{\Omega^e_{p,n}} \delta\mathbf{T} : \Big([s^{\vec{D}}]\big(\mathbf{T}(t_n^+) - \mathbf{T}(t_n^-)\big)\Big)\mathrm{d}\Omega \tag{4.32d}$$

$$+ \sum_e \int_{\Omega^e_{p,n}} \delta\mathbf{T} : \Big([g]^\top\big(\vec{D}(t_n^+) - \vec{D}(t_n^-)\big)\Big)\mathrm{d}\Omega + \sum_e \int_{\Omega^e_{p,n}} \delta\vec{D} \cdot \Big([g]\big(\mathbf{T}(t_n^+) - \mathbf{T}(t_n^-)\big)\Big)\mathrm{d}\Omega \tag{4.32e}$$

$$+ \sum_e \int_{\Omega^e_{p,n}} \delta\vec{D} \cdot \Big([\varepsilon^{\mathbf{T}}]^{-1}\big(\vec{D}(t_n^+) - \vec{D}(t_n^-)\big)\Big)\mathrm{d}\Omega - \int_{P_n^t} \delta\vec{v} \cdot \bar{\vec{t}} \, \mathrm{d}P \tag{4.32f}$$

$$+ \int_{P^\psi_{n,u}} \delta q_+ \dot{\phi} \, \mathrm{d}P + \int_{P^\psi_{n,u}} \delta\phi \dot{q}_+ \, \mathrm{d}P \tag{4.32g}$$

$$- \int_{P^\psi_{n,u}} \delta q_+ \psi_+ \, \mathrm{d}P - \int_{P^\psi_{n,u}} \delta\psi_+ q_+ \, \mathrm{d}P \tag{4.32h}$$

$$+ \int_{\Gamma^\psi_{n,u}} \delta q_+ \big(\phi(t_n^+) - \phi(t_n^-)\big)\mathrm{d}\Gamma + \int_{\Gamma^\psi_{n,u}} \delta\phi\big(q_+(t_n^+) - q_+(t_n^-)\big)\mathrm{d}\Gamma \tag{4.32i}$$

$$+ \delta\phi\frac{\phi}{R} = \ 0 \qquad \forall \ \delta\vec{v}, \ \delta\psi, \ \delta\phi, \ \delta q, \ \delta\mathbf{T}, \ \delta\vec{D}. \tag{4.32j}$$

Equation (4.32a) corresponds to the weak form of the momentum conservation and Gauss law. Equations (4.32b) and (4.32c) fulfill the piezoelectric constitutive equations on an element level, leading to a mixed-hybrid formulation. It is worth remarking that the electrical boundary integrals are obtained by considering Eq. (4.17) as a constraint to enforce equipotential condition of the top electrode and considering Eq. (4.22) as a constraint to enable coupling between the circuit and the electrodes.

Elastic Structure For the geometrically linear elastic structure, the weighted residual form within the space-time slab $Q_{s,n}$ including the boundaries $P_{s,n}$ can be obtained by eliminating the electrical degrees of freedom from the weak form given in Eq.(4.32). This reduction of Eq. (4.32) to represent the weak form of the elastic structure is valid only if the elastic structure is a conducting material, because both the electrical field and the electric displacements will vanish within a conductor. If the elastic structure is made of a dielectric material, only the piezoelectric coupling coefficient $[g]$ will vanish but the electric field will be present [44]. The weighted residual form for the elastic structure reads as

$$\int_{Q_{s,n}} \delta\vec{v}\cdot(\rho\dot{\vec{v}}-\vec{f})\;\mathrm{d}Q+\int_{Q_{s,n}} \delta\vec{v}\cdot\rho\gamma_r\vec{v}\;\mathrm{d}Q \tag{4.33a}$$

$$+\int_{Q_{s,n}} \dot{\mathbf{S}}(\delta\vec{v}):\mathbf{T}\;\mathrm{d}Q+\sum_e\int_{Q^e_{s,n}} \delta\mathbf{T}:([s]\dot{\mathbf{T}}-\dot{\mathbf{S}}(\vec{v}))\;\mathrm{d}Q \tag{4.33b}$$

$$+\int_{\Omega_{s,n}} \delta\vec{v}\cdot\Big(\rho\big(\vec{v}(t_n^+)-\vec{v}(t_n^-)\big)\Big)\mathrm{d}\Omega+\sum_e\int_{\Omega^e_{s,n}} \delta\mathbf{T}:\Big([s]\big(\mathbf{T}(t_n^+)-\mathbf{T}(t_n^-)\big)\Big)\mathrm{d}\Omega \tag{4.33c}$$

$$-\int_{P^t_{s,n}} \delta\vec{v}\cdot\bar{\vec{t}}\;\mathrm{d}P \;=\; 0 \qquad \forall\ \delta\vec{v},\ \delta\mathbf{T}. \tag{4.33d}$$

Fluid-Structure Coupling The coupling conditions in Eqs. (4.28) and (4.29) for momentum conservation and geometrical continuity on the interface are fulfilled by using interface tractions in the weighted residual form [7, 71]. The equality of structural velocities and fluid velocities at the interface is enforced by using fluid interface traction field as a Lagrange multiplier and can be expressed as

$$\int_{P_c} \delta\vec{t}_f\cdot(\vec{v}_f-\vec{v}_s)\;\mathrm{d}P-\int_{P_c} \delta\vec{v}_f\cdot\vec{t}_f\;\mathrm{d}P-\int_{P_c} \delta\vec{v}_s\cdot\vec{t}_f\;\mathrm{d}P. \tag{4.34}$$

If the fields for $\vec{v}_f$ and $\vec{v}_s$ are a priorly identical as a result of the chosen approximation, then direct coupling of fluid and structural velocity ensues, leading to an unconstrained formulation without interface traction $\vec{t}_f$ as Lagrange multiplier to enforce the equality. Such a native velocity coupling via a shared velocity approximation is straightforward if matching meshes are used at the interface.

4.3.2 Discretization

The space-time fine element approximation is constructed by dividing each space-time slab Q_n into a number of space-time elements Q_n^e, where $e = 1, 2, 3...(n_{el})$ refers to the number of elements. The number of space-time elements may be different from one time slab to another. In three-dimensional continuum approach, isoparametric elements are employed to discretize the coupled system consisting of the fluid, the piezoelectric, and the elastic structural domains. Within an element, the geometry and the unknown fields are approximated from their nodal values by employing standard shape functions. Shape functions in space-time discretization will have additional temporal components. For an arbitrary volumetric element, the spatial and temporal components of an interpolation function can be expressed as

$$N_i^t = N_i T^t = N_i(\xi,\eta,\zeta)T^v(\theta), \tag{4.35}$$

where $i = 1, 2, ...n$ refers to the number of nodes and $v = 1, 2, ...$ refers to the temporal divisions of the time slab. Here, $\xi, \eta, \zeta \in [-1, +1]$ are the natural spatial coordinates, and $\theta \in [-1, +1]$ is the natural temporal coordinate. In the space-time finite element method, time approximation follows the same procedure as space approximation using standard interpolation functions. Assuming linear interpolation in time, the temporal interpolation function can explicitly be expressed as

$$T^1(\theta)=\frac{1}{2}(1-\theta),\quad T^2(\theta)=\frac{1}{2}(1+\theta). \tag{4.36}$$

It is convenient to express time derivative of an unknown field by taking the derivative of (4.36) which is given by

$$T^1_{,\theta} = -\frac{1}{2}, \quad T^2_{,\theta} = +\frac{1}{2}. \tag{4.37}$$

Thus, within an element the geometry and the continuous field variables are interpolated from their nodal values using standard tensor product space-time interpolation functions as

$$\vec{x}^e = [T^1\mathbf{N}_x \quad T^2\mathbf{N}_x]\hat{\vec{x}}^e, \quad t^e = T^1 t^1 + T^2 t^2, \tag{4.38a}$$

$$\vec{v}^e = [T^1\mathbf{N}_v \quad T^2\mathbf{N}_v]\hat{\vec{v}}^e, \quad \psi^e = [T^1\mathbf{N}_\psi \quad T^2\mathbf{N}_\psi]\hat{\vec{\psi}}^e, \tag{4.38b}$$

$$p^e = [T^1\mathbf{N}_p \quad T^2\mathbf{N}_p]\hat{\vec{p}}^e, \tag{4.38c}$$

where $\hat{\vec{x}}^e$,$\hat{\vec{v}}^e$,$\hat{\vec{\psi}}^e$, and $\hat{\vec{p}}^e$ are the vectors of nodal coordinates, nodal velocities, nodal potential rate, and nodal pressure, respectively. $\mathbf{N}_x$ is the coordinate interpolation matrix, $\mathbf{N}_v$ is the velocity interpolation matrix, $\mathbf{N}_\psi$ is the potential rate interpolation matrix, and $\mathbf{N}_p$ is the pressure interpolation matrix. Because the stress tensor $\mathbf{T}$ and the strain tensor $\mathbf{S}$ are symmetric, they can conveniently be expressed as vectors of six components using *Voigt* notation as $\vec{T} = \{t_{xx},\ t_{yy},\ t_{zz},\ t_{yz},\ t_{xz}\ t_{xy}\}^\top$ and $\vec{S} = \{s_{xx},\ s_{yy},\ s_{zz},\ 2s_{yz},\ 2s_{xz}\ 2s_{xy}\}^\top$, respectively. The spatially discontinuous assumed field variables, namely the stresses and dielectric displacements are interpolated in a similar way as

$$\vec{T}^e = [T^1\mathbf{N}_t \quad T^2\mathbf{N}_t]\hat{\vec{T}}^e, \quad \vec{D}^e = [T^1\mathbf{N}_d \quad T^2\mathbf{N}_d]\hat{\vec{\beta}}^e. \tag{4.39}$$

where $\mathbf{N}_t$ and $\mathbf{N}_d$ are interpolation functions for the assumed stress and electric displacements, respectively. The interpolation functions for the stresses and dielectric displacements follow the works by Pian et al. [75, 76] and Sze and Pan [48]. Whereas the 8-node isoparametric hexahedral element employed in [48] contained 18 stress components and 7 dielectric components in their semi-discrete mixed-hybrid formulation, the fully-discrete space-time formulation described in this work will have 36 stress components and 14 dielectric displacement components for an eight node isoparametric hexahedral element (for linear time interpolation).

Isoparametric surface elements are employed to discretize the upper electrode surface $P^{\psi}_{n,u}$ with electric charge (q) and electric potential rate (ψ) as nodal degrees of freedom. At the electrode boundary, the top nodes of the volumetric elements discretizing the piezoelectric domain must coincide with the nodes of the surface elements discretizing the electrode boundary. As previously mentioned, the global electric potential ϕ is spatially constant and varies only in time. Thus the interpolations of charge and global electric potential are given by

$$q^e = [T^1\mathbf{N}_q \quad T^2\mathbf{N}_q]\hat{\vec{q}}^e, \quad \phi = [T^1 \times 1 \quad T^2 \times 1]\hat{\phi}. \tag{4.40}$$

An illustration of the different domains of the coupled system with their corresponding global field variables is given in Fig. 4.2.

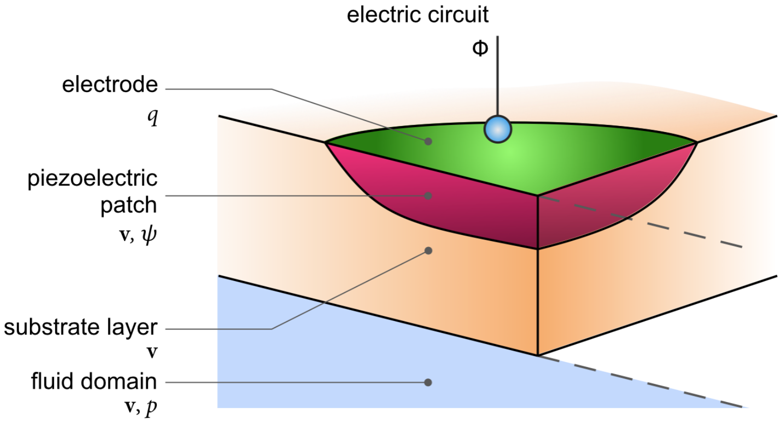

Figure 4.2: An illustration of the coupled system with global unknown field variables

4.3.3 Deforming Mesh

The deformation of the structure causes geometrical changes in the flow domain. The fluid domain must therefore be adapted to the current position of the deformed fluid-structure interface. In semi-discrete formulations, Arbitrary Lagrange-Euler (ALE) formulations are often applied. The space-time finite element formulation used here is fully discrete and allows consistent integration of the weak forms on the deforming flow domain. In order to communicate the structural displacements at the interface to the deformed fluid body, a pseudo-solid approach is used to determine the displaced node locations of the fluid mesh. To this end, the deformation of the fluid mesh is described by hyper-elastic solid that is subject to the boundary and interface displacements of the structure. This technique is fully integrated in the Newton-Raphson procedure for resolving non-linearities in the model as described below.

4.4 Solution Strategy

The highly non-linear system of equations (4.30a)–(4.34) describing the behavior of the entire coupled system—including the mesh deformation—are linearized by the Newton-Raphson method. The space-time discretization of a time slab Q_n applied to the linearized weak form results in a coupled algebraic system of equations given by

$$\mathbf{A}\Delta\hat{\vec{x}} \; = \vec{b}(t). \tag{4.41}$$

Here, $\mathbf{A}$ is the global algebraic system matrix obtained after static condensation of the local fields and assembly of element level matrices, $\Delta\hat{\vec{x}}$ is the vector of global unknowns, and $\vec{b}$ is the global force vector. The linear system of equations are solved simultaneously at each time instant in a single equation system using a preconditioned BICGStab iterative solver. The structure of the coefficient matrix along with the unknown fields pertaining to the different domains is shown in 4.3. Here, the interface traction to enforce the geometric continuity is not present because of the continuous velocity interpolation used in the example described in the proceeding section.

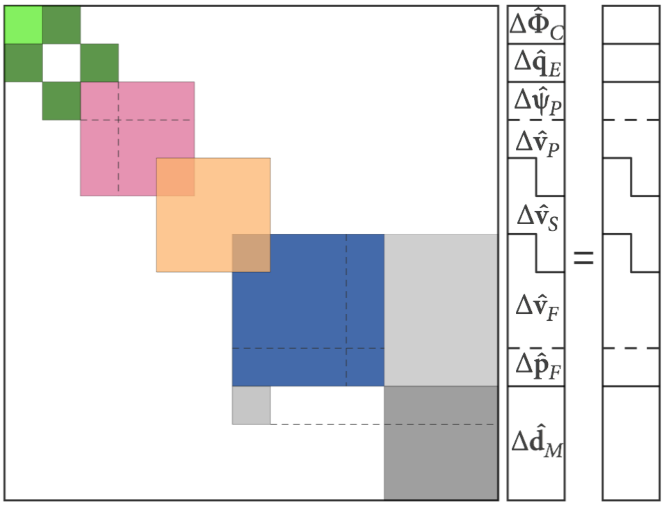

Figure 4.3: Monolithic coupled system of linear equations for a single step of the Newton-Raphson iteration

4.5 Numerical Example

A lid driven cavity with a flexible piezoelectric unimorph bottom wall is considered to illustrate the application of the monolithic space-time finite element formulation introduced in the preceding section for flow-driven piezoelectric energy harvesting. The problem setup with physical dimensions is shown in Fig. 4.4.

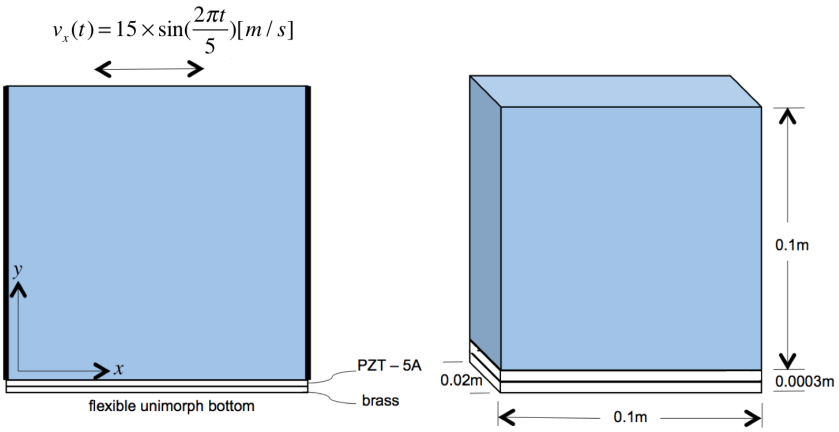

Figure 4.4: Driven cavity; **a** 2D view and **b** 3D view

The working fluid in the driven cavity is assumed to be an incompressible Newtonian fluid with a density of 1 kg/m^3 and a dynamic viscosity of 0.001 Ns/m^2. The domain is considered to be isothermal and enclosed within two rigid impermeable non-slip side walls. In other words, the side walls of the cavity are fixed, and at the surface of the side walls the fluid velocity follows the velocity of the walls. A periodical velocity is prescribed at the top of the cavity along the positive and negative axis (tangential) directions. The maximum prescribed velocity is 15 m/s. The bottom wall is made of a piezoelectric unimorph beam consisting of a PZT piezoceramic attached to a brass substrate. The total thickness of the bottom wall is 0.0003 m. The top left and right corners of the bottom wall are pin-supported to the side walls of the fluid domain, and the rest of the bottom wall is unconstrained on the length and thickness directions. The fluid properties and the lid velocity are so chosen to have a Reynolds number of 1500 and a laminar flow regime. The geometrical and material properties of the piezoelectric unimorph plate are given in Table 4.1.

Table 4.1: Geometric and material properties of the energy harvester

Quantity	Dimension	Value
Length of the beam	l (m)	0.10
Width of the beam	b (m)	0.02
Thickness of the piezo. patch (PZT-5A)	h_p (m)	0.0002
Thickness of the substructure	h_s (m)	0.0001
Height of the fluid column	h_f (m)	0.1
Young's modulus of the substructure (brass)	Y_s $\left(\mathrm{N/m^2}\right)$	100×10^7
Young's modulus of PZT-5A	Y_p $\left(\mathrm{N/m^2}\right)$	66×10^7
Mass density of the substructure (brass)	ρ_s $\left(\mathrm{Kg\,m^{-3}}\right)$	7165
Mass density of PZT-5A	ρ_p $\left(\mathrm{Kg\,m^{-3}}\right)$	7800
Piezoelectric displacement coefficient	d_{31} (m/V)	-190×10^{-12}
Permittivity	$\varepsilon_{33}^{\mathbf{S}}$ $\left(\mathrm{C^2/Nm^2}\right)$	15.93×10^{-9}

Lid driven cavity with a flexible bottom wall has been investigated by many researchers in the past including Küttler et al. [77, 78] and Bathe and Zhang [79] for validating fluid-structure interaction solvers based on partitioned approaches but not in the context of energy harvesting. Lid driven cavity with flexible wall problem offers an interesting test case in fluid-structure interaction problems because of the incompressibility constraint imposed by the fluid in the structural displacements. In other words, the volume of the fluid domain is determined from the structural displacements, but the structural displacements are unaware of the incompressibility constraint on the fluid domain. In the references cited above, the case of a driven cavity with flexible bottom was studied to assess the performance of partitioned solvers for incompressible flow and highly deformable structures. They considered the bottom wall to be extremely flexible with Young's modulus ranging from 250 $\mathrm{N/m^2}$ [77, 78] to 25,000 $\mathrm{N/m^2}$ [79]. Partitioned approaches invariably fail to converge when dealing with incompressible flow and highly deformable structures [78]. To mitigate this problem of incompressibility in the case of driven cavity with highly flexible bottom wall, Küttler at al. [78] considered two unconstrained nodes on the side walls that allowed in- and outflow of the fluid. In our case, we consider a monolithic solution procedure, where the entire coupled system is solved in one go. The structural displacements are inherently aware of the incompressible constraint on the fluid domain; hence, there is not any need for unconstrained nodes on the side walls. Moreover, large deformations are not present in the example in this section. It is pertinent to mention here that the Young's modulus of PZT-5A and the brass substructure given in Table 4.1 are two orders of magnitude lower than the original stiffness of the materials. The original stiffness of PZT-5A is 66×10^9 $\mathrm{N/m^2}$ and that of brass is 100×10^9 $\mathrm{N/m^2}$. The stiffness is reduced in order to have appreciable displacements but not large displacements. This will alter the original strength of both the materials. Even though large deformations are not considered, the incompressibility condition is still valid. The unimorph can only deform in such a way that the divergence-free condition of the fluid is satisfied.

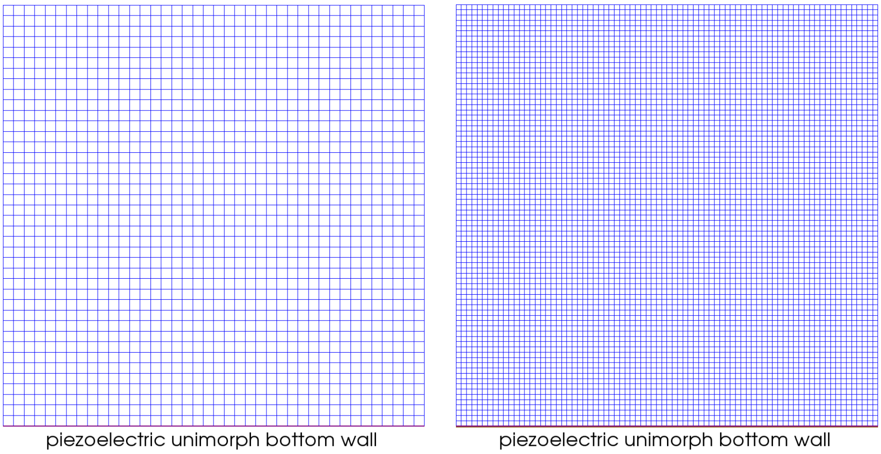

Figure 4.5: CFD mesh–front view; **a** Coarse grid and **b** fine grid

The simulations were performed on a coarse grid and a fine grid as shown in Fig. 4.5. In the coarse grid, the fluid domain is discretized with three-dimensional isoparametric hexahedral stabilized space-time finite elements in a uniform $40 \times 40 \times 1$ mesh. The piezoelectric material is discretized with three-dimensional isoparametric hexahedral space-time finite elements in a $40 \times 3 \times 1$ mesh, and the brass substructure is discretized in a uniform $40 \times 3 \times 1$ mesh as well (Fig. 4.5(a)). The width direction of all the domains is discretized with only one element. The velocity component along the width direction is set to zero at all the nodes of the mesh to emulate a 2D problem. In the fine grid, the fluid domain is discretized in a uniform $80 \times 80 \times 1$ mesh. The piezoelectric material is discretized in a uniform $80 \times 3 \times 1$ mesh, and the brass substructure is discretized in a uniform $80 \times 3 \times 1$ mesh as shown in Fig. 4.5(b). The conducting electrode on the top surface of the PZT patch is assumed to cover only the first 0.04 m of the top surface in both the simulations. The top electrode is discretized with isoparametric surface elements in a uniform 16×1 mesh in the coarse grid and with uniform 32×1 mesh in the fine grid. As mentioned earlier, the nodes of the elements discretizing the electrode surface must coincide with the top nodes of the three-dimensional elements discretizing the piezoelectric patch. The unimorph is assumed to be in open-circuit condition (infinite resistance). The choice of electrode coverage and open-circuit condition is explained further in the section. The simulations were run for a period of 100 s with a constant Δt value of 0.033 s at a Reynolds number of 1500. The tolerance criteria for the residual within the Newton-Raphson iteration was set to $\varepsilon = 1.0 \times 10^{-8}$, and the tolerance for the iterative solver was set to $\varepsilon_s = 1.0 \times 10^{-15}$.

The results of the fluid mesh displacement from the coarse grid simulations are shown in Fig. 4.6 for four different time instants. Figures 4.6(a) and 4.6(b) depict two of the various instances when the deformation is at its highest. Figures 4.6(c) and 4.6(d) show two of the other instances before the maximum displacement is reached. The pressure solution and the velocity magnitude glyphs from the coarse grid simulation are depicted in Fig. 4.7.

The unimorph at the bottom is unconstrained except for the top corner interface nodes and deforms under the influence of fluid pressure. The resistance of the unimorph comes from both its mass and density. It is clear from the fires that the flexible structure is cognizant of the incompressibility condition on the fluid and deforms in such a way that the divergence-free condition of the fluid is preserved at all time instances. In the context of this particular example, this deformation behavior of the structure has implications on the power harvested from the unimorph. Piezoelectric energy harvesters are very sensitive to excitation frequencies, and he maximum power output is harvested at resonance frequencies or near resonance frequencies of the harvester. The power output is typically higher if the harvester is operated in its fundamental vibration mode compared to higher vibration modes. Also, depending

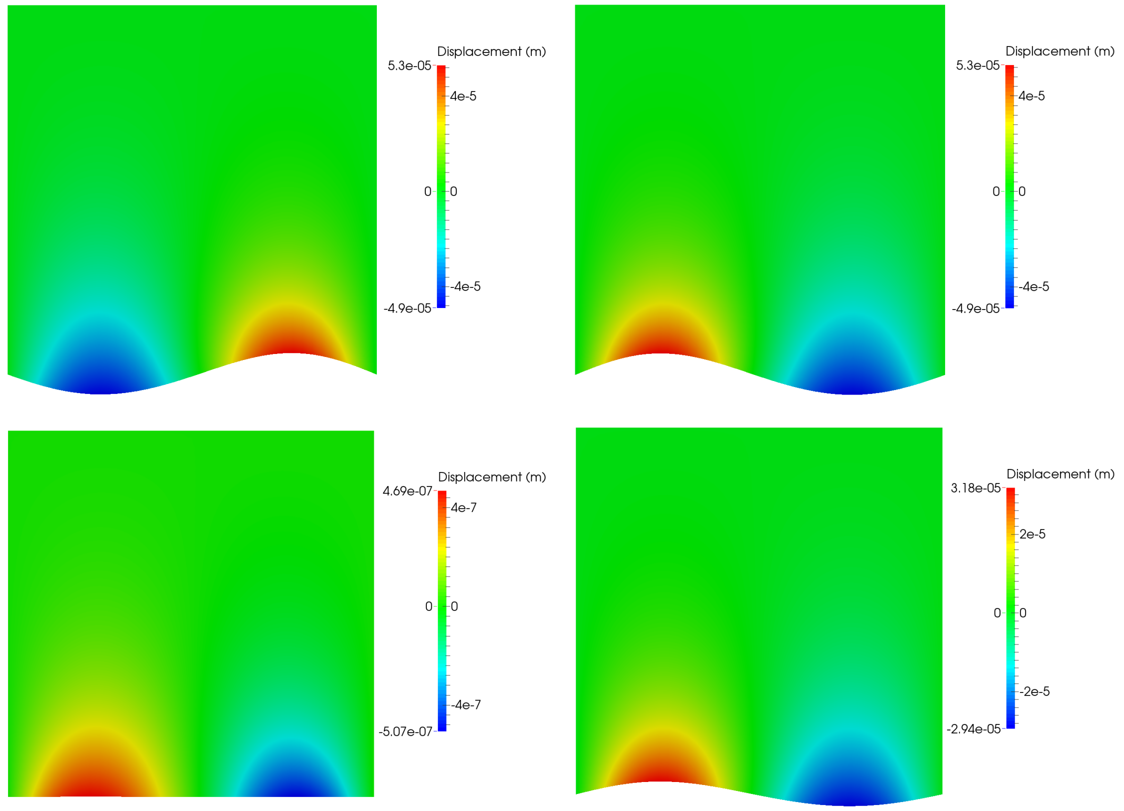

Figure 4.6: Displacement (coarse grid); **a** at $t = 1.33$ s, **b** at $t = 3.83$ s, **c** at $t = 25$ s and **d** at $t = 83.33$ s. The mesh deformation is amplified for visualization, and the actual deformation can be inferred from the color legend.

on how the harvester is supported (cantilever, pin-supported, clamped-clamped), the dynamic strain distribution changes sign at certain nodes for certain vibration modes. For cantilever beams, all the modes other than the first mode contain strain nodes, where the dynamic strain distribution changes sign. According to Gauss' law, the total charge on the electrode area is the integral of the electric displacement over the area of the conducting electrode covering the piezoelectric patch. Thus, the strain distribution influences the total charge collected on the electrodes. The electrode cover is not assumed to be continuous in our example to avoid charge cancellation due to the presence of strain nodes.

The fluid mesh displacements, pressure solution, and the velocity magnitude glyphs from the fine grid are shown in Figs. 4.8 and 4.9

As expected, the maximum value of pressure goes from 82.3 $\mathrm{N/m^2}$ for the coarse grid simulation to 109 $\mathrm{N/m^2}$ for the fine grid solution. In both the cases, the maximum pressure occurs at the top corners of the wall. The structural displacements, however, decrease as the resolution of the grid is increased. This decrease in displacement could be attributed to the change in natural frequency of the harvester due to the increase in mesh resolution. The voltage output from the two simulations is given in Fig. 4.10(a). It can be seen that the voltage output is very low even for the open-circuit condition, and the voltage output from the fine grid solution (12 mV) is less than the voltage output from the coarse grid simulation (15 mV). This is expected as the displacements form the fine grid simulation are lower than the displacements from the coarse grid simulation. It can be reasonably predicted that further increase in the resolution of the mesh would lead to a convergent behavior for the structural displacements and the voltage output. Furthermore, it is well known that the voltage output increases as the resistance

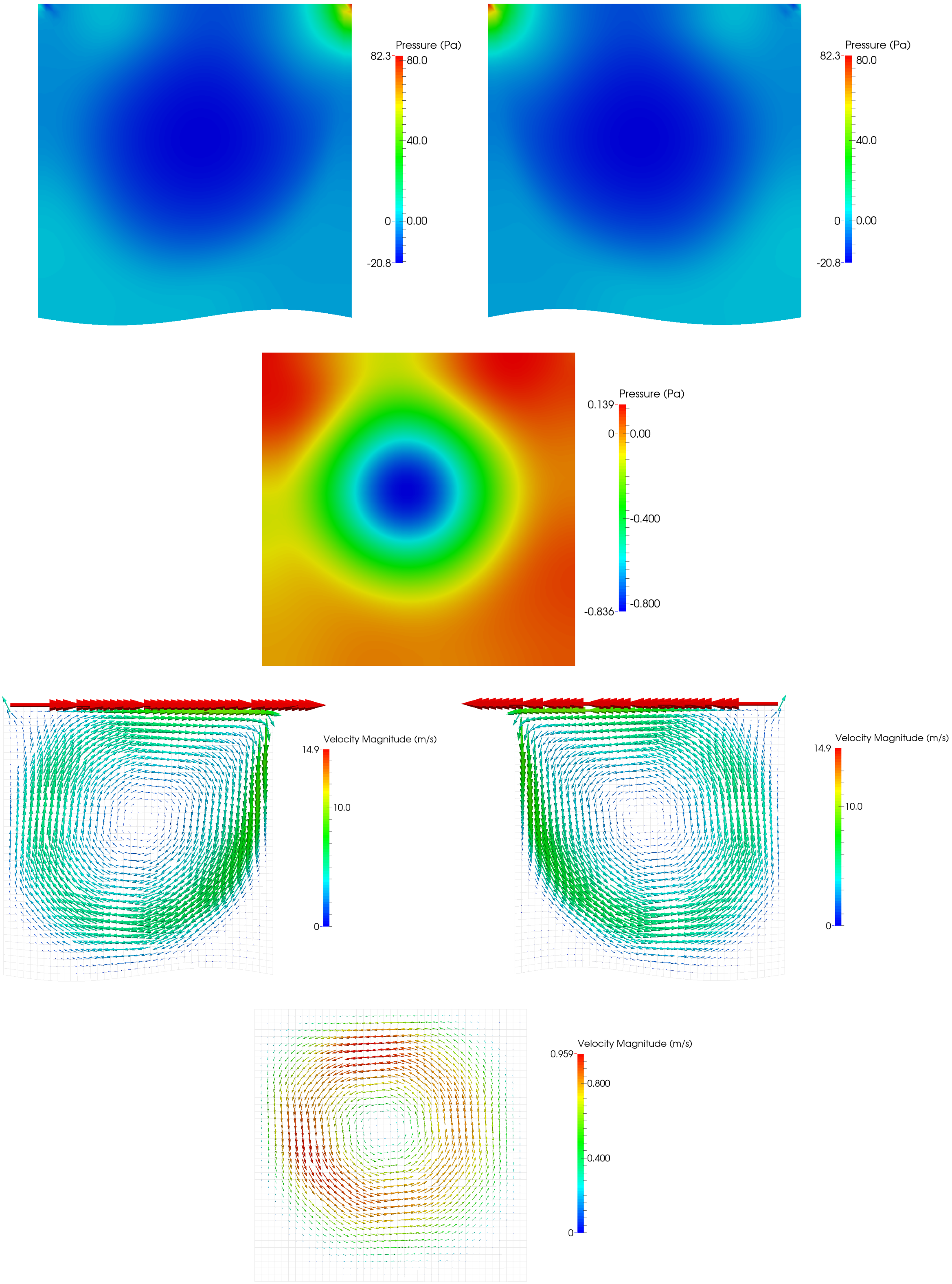

Figure 4.7: Pressure (coarse grid); **a** at $t = 1.33$ s, **b** at $t = 3.83$ s and **c** at $t = 25$ s. Glyphs–velocity magnitude (coarse grid); **a** at $t = 1.33$ s, **b** at $t = 3.83$ s and **c** at $t = 25$ s. The mesh deformation is amplified for visualization, and the actual deformation can be inferred from the color legend.

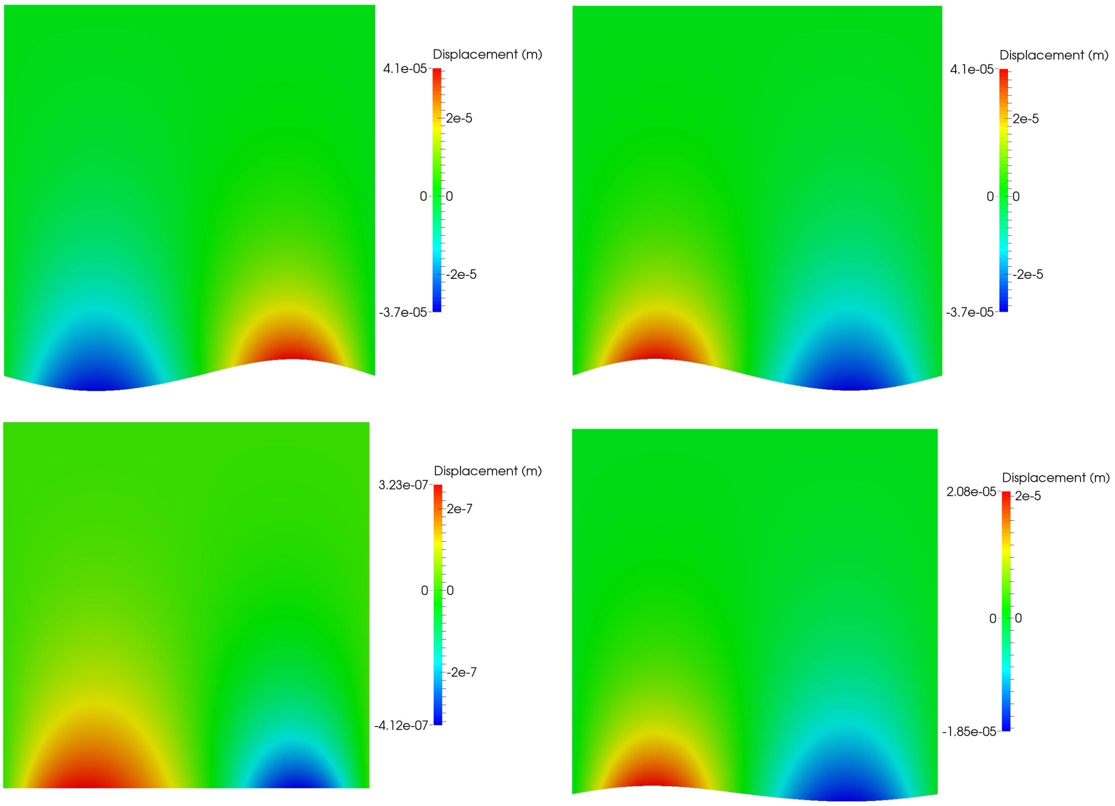

Figure 4.8: Displacement (fine grid); **a** at $t = 1.33$ s, **b** at $t = 3.83$ s, **c** at $t = 25$ s and **d** at $t = 83.33$ s. The mesh deformation is amplified for visualization, and the actual deformation can be inferred from the color legend.

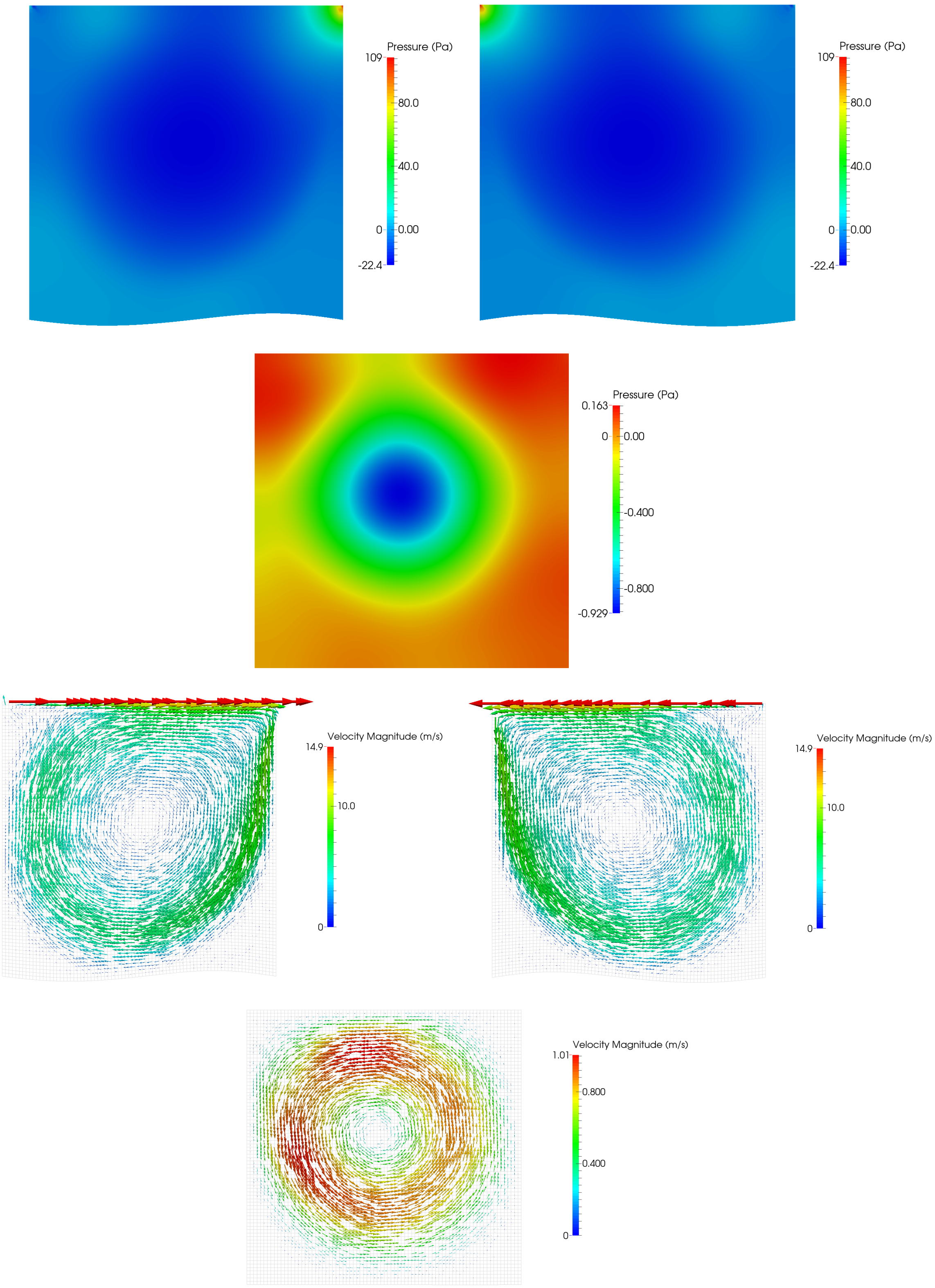

Figure 4.9: Pressure (fine grid); **a** at $t = 1.33$ s, **b** at $t = 3.83$ s and **c** at $t = 25$ s. Glyphs–velocity magnitude (fine grid); **a** at $t = 1.33$ s, **b** at $t = 3.83$ s and **c** at $t = 25$ s. The mesh deformation is amplified for visualization, and the actual deformation can be inferred from the color legend.

increases up to a certain value after which the voltage output becomes less sensitive to the variations in resistance value. The harvester in our example is not deforming in its fundamental mode and the displacements are very small. The voltage and power output in this case will be very negligible (close to zero) for a finite value of resistive load. Open-circuit condition is chosen to have a non-negligible voltage output.

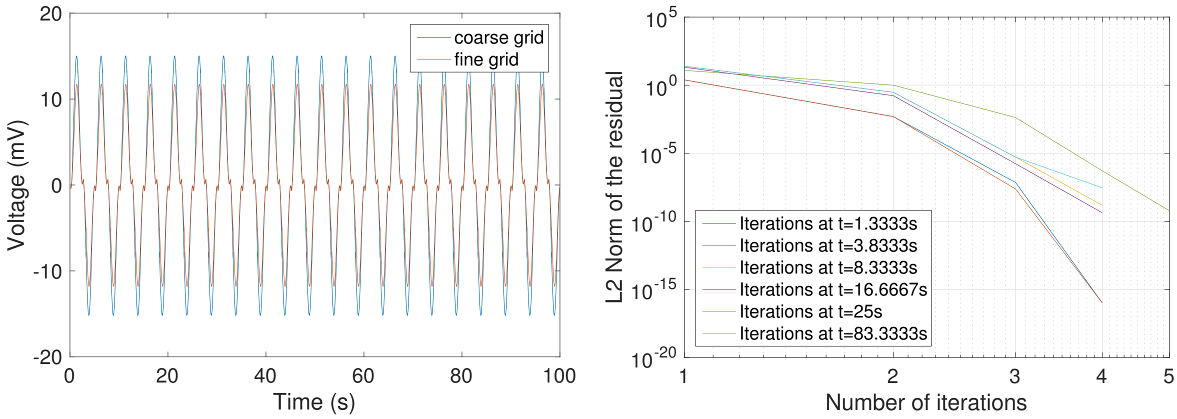

Figure 4.10: **a** Voltage output and **b** convergence history of the residual for six different time instances

The convergence history of the residual (from the coarse grid simulation) for six different time slabs is shown in Fig. 4.10(b). It has been argued that simultaneous solution procedures are not effective in dealing with structures with large internal forces compared to the fluid [80]. In the example considered here, the structure is indeed very stiff compared to what has usually been considered [78, 79]. It can be seen in Fig. 4.10(b) that the iteration scheme reached the coupled monolithic solution in a time slab within four to five iteration steps for the chosen accuracy level ($\varepsilon = 10^{-8}$).

4.6 Conclusion

A simultaneous solution scheme for flow-driven piezoelectric energy harvester is presented. The proposed solution scheme is based on a three-dimensional mixed-hybrid space-time finite element formulation that enables uniform discretization of the entire coupled system. The numerical example considered in this article, although academic in nature, provides a platform to demonstrate both the efficiency of the monolithic solution approach and its application for piezoelectric energy harvesting problems. Validation of the proposed approach for different flow-driven harvesting examples are currently under study.

Chapter 5

Summary and Future Work

The continued development of piezoelectric materials had led to their utilization in a wide range of applications including energy harvesting, shunt damping, and general actuation and sensing. Piezoelectric energy harvesting in particular has received significant attention over the past years due to the advances in low-power electronic devices, such as the ubiquitous wireless sensor networks used in structural health monitoring and conditional monitoring, portable electronic devices, and industrial measurement systems. The aim of piezoelectric energy harvesting is to power such electronic devices by scavenging ambient vibration energy, thereby minimizing the need for batteries and enabling cost-effective and environment-friendly solution. Real world applications require complex electrical circuitry to enable efficient transformation of ans storage of the power harvested. The circuit may include a capacitor for storage, a rectifier for ac-dc conversion, or just a resistive load to characterize the power generating capabilities of a harvester. In this work, the circuit is limited to a resistive load connected to the electrodes of the piezoelectric patches. Modeling and simulations are essential in order to characterize the power output of these devices and to develop novel design strategies for a wide variety of applications. Research in piezoelectric energy harvesting has been focused predominantly on harvesting energy from the vibration of the structure to which the piezoelectric material is attached, and the focus on converting kinetic energy of fluid flow has been limited.

The goal of this research work is to improve the state-of-the-art in modeling of piezoelectric energy harvesters by developing a unified mathematical model that can be used to analyze both base-excited and flow-driven energy harvesters. To that extent, a monolithic simultaneous solution method based on a three-dimensional mixed-hybrid space-time finite finite element formulation has been presented in this work. The simultaneous solution approach enables uniform and consistent discretization of all the domains and ensures accurate solution to the strongly coupled system. Monolithic solution methods need implementation of a completely new solver. The new solver with suitable preconditioner has been developed and implemented in a Python based object-oriented programming framework.

Chapter 2 In chapter two, a three-dimensional mixed-hybrid finite element method has been introduced for the frequency domain analysis of base-excited symmetric bimorph cantilever harvesters for parallel and series configuration of the piezoelectric layers. Typical piezoelectric energy harvesters are thin cantilever structures, and a mixed-hybrid formulation mitigates locking phenomenon, which is frequently encountered in modeling thin structures with three-dimensional elements. A Galerkin weighted residual formulation has been utilized to convert the model equations—pertaining to the piezoelectric structure, the elastic substrate structure, and the attached resistive load—into a single integral equation consisting of structural velocities, electric potential rate, electric charge, and the global electric potential as the global unknown field variables. The element-level unknown fields have been eliminated by dynamic condensation, and the resulting pseudo-rational eigenvalue problem has been solved to obtain the various FRFs for series and parallel bimorph configurations as studied by Erturk et al. [36]. A comparison of results indicates that the results from the mixed-hybrid finite element formulation are very close to both the experimental results and the results from the simplified mechanical model proposed in [36].

The originality of the mixed-hybrid formulation presented in this chapter lies in how the electrode-circuit coupling has been accomplished. The model equations of the electrode-circuit coupling has been naturally included in the weak formulation and allows calculating the fundamental frequencies of the harvesters for any given resistive load by directly solving the rational eigenvalue problem. It has been shown in the results that the resonant frequency of the harvester changes as the resistive load changes. In many conventional analytical models, this shift is calculated from the frequency response functions. In other numerical models, this shift is calculated by frequency sweeps. In these cases, identifying the shift accurately depends on the resolution of the frequency sweeps. However, in the formulation proposed in this chapter, this can be accurately calculating by solving the pseudo-rational eigenvalue problem.

Chapter 3 In chapter three, the mixed-hybrid finite element formulation from chapter two has been further developed to accommodate time domain analysis of base-excited piezoelectric harvesters. A fully discrete space-time finite element formulation has been developed for the analysis in time domain. Discontinuous Galerkin method has been utilized for time integration of the monolithic formulation. The element-level degrees of freedom has been eliminated from the global equations by static condensation, and the resulting monolithic algebraic equation of the coupled system has been solved by standard solution methods. First, a comparison of results from the time domain analysis with the results from the frequency domain analysis has been presented. In addition to this, the effect of quadratic approximation of the electric potential in the thickness direction of piezoelectric patches has been presented. A study on the electrode configuration on a unimorph harvester along with a study on the effect of strain nodes on the harvested power have been presented in this chapter. The outcome of the studies can be summarized as follows:

- The results from the time domain analysis were found to be in perfect match with the results from the frequency domain analysis, lending further confidence on the ability of the proposed formulation.
- A comparison of quadratic and linear approximations of electric potential along the thickness of the piezoelectric layer indicates that quadratic approximation is necessary to account for the induced electric potential, but the global voltage, power, and displacement trends are not significantly different between the two approximation, at least in the case of very thin beams considered in the study.
- The study on electrode coverage for the first bending mode of a unimorph harvester indicates that for low values of resistance, the maximum power output is achieved when the electrode layer completely covers the piezoelectric patch. For higher resistive loads, there exists an optimum electrode length above which the power output starts to decrease.
- For cantilever harvester configurations, all bending modes other than the first bending mode have strain nodes, where the dynamic strain distribution changes sign. Covering these strain nodes with electrode leads to a reduction in power output due to charge cancellation. Segmented electrode configurations are recommended to mitigate the charge cancellation effect.

Chapter 4 In this chapter, a unified monolithic space-time formulation for flow-driven harvesters has been presented. The formulation from the previous chapters has been further extended to include fluid domain into the monolithic framework. The choice of velocities as one of the primary field unknowns for the piezoelectric structure has been made apparent in this chapter. Formulation of the piezoelectric structure in velocity variables enables native coupling of the fluid domain, leading to a consistent discretization of the fluid and the piezoelectric structure in space and time. Moving mesh has been implemented by treating the fluid as hyper-elastic solid that is subject to the boundary displacements of the structure. This has been made possible by employing stabilized isoparametric space-time finite elements, which allow the fluid boundary to move along with the structural displacements by specifying arbitrary displacements of the mesh nodes. Galerkin/least-squares stabilization has been employed to suppress numerical oscillations, which utilizes equal order interpolations for velocity and pressure variables. After static condensation of the element-level degrees of freedom, the resulting non-linear systems of coupled equations is solved by Newton-Raphson method. Furthermore, a preconditioned BICGStab iterative solver has been employed to solve the large sparse systems of linearized equations. The developed formulation has been used to study the case of a driven cavity with flexible unimorph bottom wall. The simulations indicate that the structural displacements obey the incompressibility constraint of the fluid by deforming in a such a way that the volume of the fluid is conserved. The voltage output has been found to be very low due to the higher mode behavior of the structure.

The monolithic space-time finite element formulation and its implementation outlined in this research work are fundamentally new addition to the existing state-of-the-art modeling approaches for base-excited and flow-driven harvesters. Reproduction of any natural phenomenon through dynamic simulations is a challenging task owing to the vagaries of nature and assumptions on the model forced by computational constraints. The advantage of a fully three-dimensional approach and a uniform discretization scheme enable retaining as much of the physics of piezoelectric energy harvesting as possible. Furthermore, numerical results reported in this work are highly encouraging and lends confidence in increasing the complexity even further to assess the capabilities of the solver. This body of work could serve as the fundamental platform for future studies, which would increase the existing capabilities of the solver. As mentioned earlier, real world applications require complex circuitry. The formulation outlined in this dissertation is capable of including linear circuit components with little modification. However, addition of non-linear components require more in-depth investigations. The formulation is also capable of supporting geometrical and material non-linearities, although this is not touched upon in this work. Further model validation is also suggested as an area of future work. The primary focus of this research endeavor has been on developing a platform that will enable in-depth investigations of the strongly coupled problem. Validation of the model for base-excited and flow-driven harvesters with non-uniform geometry is already partially under progress. Output of these validation studies will help furthering our understanding of the coupled problem and improve the framework outlined in this work

Bibliography

[1] S. R. Anton and H. A. Sodano, "A review of power harvesting using piezoelectric materials (2003—2006)," *Smart Materials and Structures*, vol. 16, no. 3, p. R1, 2007. (Cited on pages 5, 7, 9, 17, 21, 39 and 63.)

[2] C. Mo, S. Kim, and W. W. Clark, "Theoretical analysis of energy harvesting performance for unimorph piezoelectric benders with interdigitated electrodes," *Smart Materials and Structures*, vol. 18, no. 5, p. 055017, 2009. (Cited on pages 5 and 9.)

[3] S. Lee, B. D. Youn, and B. C. Jung, "Robust segment-type energy harvester and its application to a wireless sensor," *Smart Materials and Structures*, vol. 18, no. 9, p. 095021, 2009. (Cited on pages 5 and 12.)

[4] A. Erturk, O. Bilgen, M. Fontenille, and D. J. Inman, "Piezoelectric energy harvesting from macro-fiber composites with an application to morphing-wing aircrafts," in *Morphing*, p. 21 pp, October 6-9, 2008 2008. (Cited on pages 5, 14 and 64.)

[5] F. Lu, H. P. Lee, and S. P. Lim, "Modeling and analysis of micro piezoelectric power generators for micro-electromechanical-systems applications," *Smart Materials and Structures*, vol. 13, no. 1, pp. 57–63, 2004. (Cited on pages 5, 15 and 22.)

[6] A. Mehmood, A. Abdelkefi, M. Hajj, A. Nayfeh, I. Akhtar, and A. Nuhait, "Piezoelectric energy harvesting from vortex-induced vibrations of circular cylinder," *Journal of Sound and Vibration*, vol. 332, no. 19, pp. 4656 – 4667, 2013. (Cited on pages 5, 17, 18 and 64.)

[7] B. Hübner, E. Walhorn, and D. Dinkler, "A monolithic approach to fluid-structure interaction using space–time finite elements," *Computer Methods in Applied Mechanics and Engineering*, vol. 193, no. 23–26, pp. 2087 – 2104, 2004. (Cited on pages 5, 19, 40, 48, 64, 68 and 70.)

[8] C. Williams and R. Yates, "Analysis of a micro-electric generator for microsystems," *Sensors and Actuators A: Physical*, vol. 52, no. 1, pp. 8 – 11, 1996. (Cited on pages 7 and 15.)

[9] P. Mitcheson, P. Miao, B. Stark, E. Yeatman, A. Holmes, and T. Green, "Mems electrostatic micropower generator for low frequency operation," *Sensors and Actuators A: Physical*, vol. 115, no. 2–3, pp. 523 – 529, 2004. The 17th European Conference on Solid-State Transducers. (Cited on page 7.)

[10] P. Glynne-Jones, M. Tudor, S. Beeby, and N. White, "An electromagnetic, vibration-powered generator for intelligent sensor systems," *Sensors and Actuators A: Physical*, vol. 110, no. 1–3, pp. 344 – 349, 2004. Selected Papers from Eurosensors {XVI} Prague, Czech Republic. (Cited on page 7.)

[11] H. A. Sodano, G. Park, and D. J. Inman, "Estimation of electric charge output for piezoelectric energy harvesting," *Strain*, vol. 40, pp. 49–58, 2004. (Cited on pages 7, 15, 16, 21, 22, 39 and 54.)

[12] S. Priya, "Advances in energy harvesting using low profile piezoelectric transducers," *Journal of Electroceramics*, vol. 19, no. 1, pp. 167–184, 2007. (Cited on pages 7 and 39.)

[13] S. Roundy, E. S. Leland, J. Baker, E. Carleton, E. Reilly, E. Lai, B. Otis, J. M. Rabaey, P. K. Wright, and V. Sundararajan, "Improving power output for vibration-based energy scavengers," *IEEE Pervasive Computing*, vol. 4, pp. 28–36, Jan 2005. (Cited on pages 7 and 11.)

[14] J. Baker, S. Roundy, and P. Wright, "Alternative Geometries for Increasing Power Density in Vibration Energy Scavenging," in *3rd International Energy Conversion Engineering Conference*, pp. 1–12, 2005. (Cited on pages 10 and 11.)

[15] K. A. Cook-Chennault, N. Thambi, and A. M. Sastry, “Powering mems portable devices—a review of non-regenerative and regenerative power supply systems with special emphasis on piezoelectric energy harvesting systems,” *Smart Materials and Structures*, vol. 17, no. 4, p. 043001, 2008. (Cited on page 10.)

[16] H. A. Sodano, J. Lloyd, and D. J. Inman, “An experimental comparison between several active composite actuators for power generation,” *Smart Materials and Structures*, vol. 15, pp. 1211–1216, 2006. (Cited on page 10.)

[17] F. Goldschmidtboeing and P. Woias, “Characterization of different beam shapes for piezoelectric energy harvesting,” *Journal of Micromechanics and Microengineering*, vol. 18, no. 10, p. 104013, 2008. (Cited on page 10.)

[18] D. Zhu, M. J. Tudor, and S. P. Beeby, “Strategies for increasing the operating frequency range of vibration energy harvesters: a review,” *Measurement Science and Technology*, vol. 21, no. 2, p. 022001, 2010. (Cited on page 11.)

[19] M. Zhu, E. Worthington, and A. Tiwari, “Design study of piezoelectric energy-harvesting devices for generation of higher electrical power using a coupled piezoelectric-circuit finite element method,” *IEEE Transactions on Ultrasonics, Ferroelectrics, and Frequency Control*, vol. 57, pp. 427–437, 2010. (Cited on pages 11 and 17.)

[20] M. I. Friswell and S. Adhikari, “Sensor shape design for piezoelectric cantilever beams to harvest vibration energy,” *Journal of Applied Physics*, vol. 108, no. 1, 2010. (Cited on pages 11 and 57.)

[21] T. Albach, A. Sutor, and R. Lech, “Elektromechanischer energiewandler auf basis eines piezokeramischen biegebalkens,” *Technisches Messen*, vol. 76, no. 3, pp. 112–121, 2009. (Cited on page 11.)

[22] A. Erturk, P. A. Tarazaga, J. R. Farmer, and D. J. Inman, “Effect of strain nodes and electrode configuration on piezoelectric energy harvesting from cantilevered beams,” *Journal of Vibration and Acoustics*, vol. 131, no. 1, p. 011010, 2009. (Cited on pages 12, 15, 56 and 59.)

[23] E. Naudascher and D. Rockwell, *Flow-Induced Vibrations: An Engineering Guide*. Dover Civil and Mechanical Engineering, Dover Publications, 2012. (Cited on page 12.)

[24] J. Allen and A. Smits, “Energy harvesting eel,” *Journal of Fluids and Structures*, vol. 15, no. 3, pp. 629 – 640, 2001. (Cited on pages 12, 13 and 63.)

[25] A. H. Techet, J. J. Allen, and A. J. Smits, “Piezoelectric eels for energy harvesting in the ocean,” *The 12th International Offshore and Polar Engineering Conference*, pp. 1–6, 2002. (Cited on pages 13 and 63.)

[26] G. W. Taylor, J. R. Burns, S. A. Kammann, W. B. Powers, and T. R. Welsh, “The energy harvesting eel: a small subsurface ocean/river power generator,” *IEEE Journal of Oceanic Engineering*, vol. 26, pp. 539–547, 2001. (Cited on pages 13 and 63.)

[27] N. G. Elvin and A. A. Elvin, “A general equivalent circuit model for piezoelectric generators,” *Intelligent Material Systems and Structures*, vol. 20, pp. 3–9, 2009. (Cited on page 13.)

[28] W. P. Robbins, D. Morris, I. Marusic, and T. O. Novak, “Wind-generated electrical energy using flexible piezoelectric mateials,” *ASME 2006 International Mechanical Engineering Congress and Exposition*, pp. 1–10, 2006. (Cited on pages 13 and 63.)

[29] S. Pobering and N. Schwesinger, “Power supply for wireless sensor systems,” *IEEE Sensors 2008 Conference*, pp. 685–688, 2008. (Cited on page 13.)

[30] H. D. Akaydin, N. Elvin, and Y. Andreopoulos, “Wake of a cylinder: a paradigm for energy harvesting with piezoelectric materials,” *Experiments in Fluids*, vol. 49, pp. 291–304, 2010. (Cited on page 14.)

[31] S. R. Anton and D. J. Inman, “Vibration energy harvesting for unmanned aerial vehicles,” vol. 6928 of *Proc. Spie.*, pp. 692824–692824–12, 2008. (Cited on pages 14 and 64.)

[32] S. Roundy and P. K. Wright, “A piezoelectric vibration based generator for wireless electronics,” *Smart Materials and Structures*, vol. 13, no. 5, p. 1131, 2004. (Cited on pages 15, 16, 19, 21 and 40.)

[33] N. E. Dutoit, B. L. Wardle, and S.-G. Kim, “Design considerations for mems-scale piezoelectric mechanical vibration energy harvesters,” *Integrated ferroelectrics*, vol. 71, pp. 121–160, 2005. (Cited on pages 15, 16, 19, 21, 22, 40 and 54.)

[34] A. Erturk and D. J. Inman, “A distributed parameter electromechanical model for cantilevered piezoelectric energy harvesters,” *Journal of Vibration and Acoustics*, vol. 130, no. 4, p. 041002, 2008. (Cited on pages 15, 57 and 64.)

[35] A. Erturk and D. J. Inman, “On mechanical modeling of cantilevered piezoelectric vibration energy harvesters,” *Intelligent Material Systems and Structures*, vol. 19, pp. 1311–1325, 2008. (Cited on pages 15, 16, 19, 21, 22 and 40.)

[36] A. Erturk and D. J. Inman, “An experimentally validated bimorph cantilever model for piezoelectric energy harvesting from base excitations,” *Smart Materials and Structures*, vol. 18, pp. 1–18, 2009. (Cited on pages 15, 16, 19, 20, 21, 22, 32, 35, 40, 51, 52, 53 and 81.)

[37] A. Tabesh and L. G. Fréchette, “An improved small-deflection electromechanical model for piezoelectric bending beam actuators and energy harvesters,” *Journal of Micromechanics and Microengineering*, vol. 18, no. 10, p. 104009, 2008. (Cited on page 15.)

[38] H. Allik and T. J. R. Hughes, “Finite element method for piezoelectric vibration,” *International Journal for Numerical Methods in Engineering*, vol. 2, no. 2, pp. 151–157, 1970. (Cited on pages 16, 22 and 40.)

[39] A. Benjeddou, “Advances in piezoelectric finite element modeling of adaptive structural elements: a survey,” *Computers & Structures*, vol. 76, no. 1-3, pp. 347 – 363, 2000. (Cited on pages 16, 22, 40 and 54.)

[40] A. R. Barnett, S. M. Peelamedu, R. V. Dukkipati, and N. G. Naganathan, “Finite element approach to model and analyze piezoelectric actuators,” *Series c*, vol. 44, pp. 476–485, 2001. (Cited on page 16.)

[41] S. Wang, “A finite element model for the static and dynamic analysis of a piezoelectric bimorph,” *International Journal of Solids and Structures*, vol. 41, no. 15, pp. 4075 – 4096, 2004. (Cited on pages 16 and 55.)

[42] C. De Marqui Junior, A. Erturk, and D. J. Inman, “An electromechanical finite element model for piezoelectric energy harvester plates,” *Sound and vibration*, vol. 327, pp. 9–25, 2009. (Cited on pages 16, 17 and 64.)

[43] M. Zhu, E. Worthington, and J. Njuguna, “Analyses of power output of piezoelectric energy-harvesting devices directly connected to a load resistor using a coupled piezoelectric-circuit finite element method,” *IEEE Transactions on Ultrasonics, Ferroelectrics, and Frequency Control*, vol. 56, pp. 1309–1318, 2009. (Cited on pages 16 and 17.)

[44] O. Thomas, J.-F. Deü, and J. Ducarne, "Vibrations of an elastic structure with shunted piezoelectric patches: efficient finite element formulation and electromechanical coupling coefficients," *International Journal for Numerical Methods in Engineering*, vol. 80, no. 2, pp. 235–268, 2009. (Cited on pages 16, 17, 22, 27, 40, 45 and 70.)

[45] N. G. Elvin and A. A. Elvin, "A coupled finite element-circuit simulation model for analyzing piezoelectric energy generators," *Intelligent Material Systems and Structures*, vol. 20, pp. 587–595, 2009. (Cited on page 16.)

[46] H. S. Tzou and C. I. Tseng, "Distributed piezoelectric sensor/actuator design for dynamic measurement/control of distributed parameter systems: A piezoelectric finite element approach," *Journal of Sound and Vibration*, vol. 138, no. 1, pp. 17–34, 1990. (Cited on pages 16 and 40.)

[47] K. Ghandi and N. W. Hagood, "Hybrid finite element model for phase transitions in nonlinear electromechanically coupled material," in *Smart Structures and Materials 1997: Mathematics and Control in Smart Structures* (V. V. Varadan and J. Chandra, eds.), vol. 3039 of *Proc. Spie.*, pp. 97–112, June 1997. (Cited on pages 16 and 22.)

[48] K. Sze and Y. Pan, "Hybrid finite element models for piezoelectric materials," *Journal of Sound and Vibration*, vol. 226, no. 3, pp. 519 – 547, 1999. (Cited on pages 16, 22, 24, 28, 40, 44, 45 and 71.)

[49] S. Klinkel and W. Wagner, "A geometrically non-linear piezoelectric solid shell element based on a mixed multi-field variational formulation," *International Journal for Numerical Methods in Engineering*, vol. 65, no. 3, pp. 349–382, 2006. (Cited on pages 16, 22 and 40.)

[50] S. Klinkel, F. Gruttmann, and W. Wagner, "A robust non-linear solid shell element based on a mixed variational formulation," *Computer Methods in Applied Mechanics and Engineering*, vol. 195, no. 1–3, pp. 179 – 201, 2006. (Cited on pages 16, 22 and 40.)

[51] J. S. Yang, "Equations for thick elastic plates with partially electroded piezoelectric actuators and higher order electric fields," *Smart Materials and Structures*, vol. 8, no. 1, p. 73, 1999. (Cited on pages 16, 22 and 54.)

[52] H. A. Sodano, D. J. Inman, and G. Park, "A review of power harvesting from vibration using piezoelectric materials," *The shock and vibration digest*, vol. 36, pp. 197–205, 2004. (Cited on pages 17 and 63.)

[53] H. S. Kim, J.-H. Kim, and J. Kim, "A review of piezoelectric energy harvesting based on vibration," *International Journal of Precision Engineering and Manufacturing*, vol. 12, no. 6, pp. 1129–1141, 2011. (Cited on pages 17 and 63.)

[54] R. Caliò, U. B. Rongala, D. Camboni, M. Milazzo, C. Stefanini, G. de Petris, and C. M. Oddo, "Piezoelectric energy harvesting solutions," *Sensors*, vol. 14, no. 3, p. 4755, 2014. (Cited on pages 17 and 63.)

[55] A. Erturk, W. G. R. Vieira, C. De Marqui, and D. J. Inman, "On the energy harvesting potential of piezoaeroelastic systems," *Applied Physics Letters*, vol. 96, no. 18, 2010. (Cited on pages 17, 22 and 64.)

[56] C. De Marqui, A. Erturk, and D. J. Inman, "Piezoaeroelastic modeling and analysis of a generator wing with continuous and segmented electrodes," *Journal of Intelligent Material Systems and Structures*, vol. 21, no. 10, pp. 983–993, 2010. (Cited on pages 17 and 64.)

[57] C. De Marqui, W. G. R. Vieira, A. Erturk, and D. J. Inman, "Modeling and Analysis of Piezoelectric Energy Harvesting From Aeroelastic Vibrations Using the Doublet-Lattice Method," *Journal of Vibration and Acoustics*, vol. 133, no. February, p. 011003, 2011. (Cited on page 17.)

[58] H. D. Akaydin, N. Elvin, and Y. Andreopoulos, “Energy harvesting from highly unsteady fluid flows using piezoelectric materials,” *Intelligent Material Systems and Structures*, vol. 21, pp. 1263–1278, 2010. (Cited on pages 17, 18 and 64.)

[59] Y. Amini, H. Emdad, and M. Farid, “An accurate model for numerical prediction of piezoelectric energy harvesting from fluid structure interaction problems,” *Smart Materials and Structures*, vol. 23, pp. 1–17, 2014. (Cited on pages 17, 18 and 64.)

[60] M. Heil, A. L. Hazel, and J. Boyle, “Solvers for large-displacement fluid–structure interaction problems: segregated versus monolithic approaches,” *Computational Mechanics*, vol. 43, no. 1, pp. 91–101, 2008. (Cited on page 19.)

[61] A. Abdelkefi, F. Najar, A. H. Nayfeh, and S. B. Ayed, “An energy harvester using piezoelectric cantilever beams undergoing coupled bending–torsion vibrations,” *Smart Materials and Structures*, vol. 20, no. 11, p. 115007, 2011. (Cited on pages 19, 21 and 40.)

[62] S. Ravi and A. Zilian, *Numerical Modeling of Flow-Driven Piezoelectric Energy Harvesting Devices*, pp. 399–426. Springer International Publishing, 2016. (Cited on pages 20, 22, 48, 62 and 68.)

[63] A. Zilian and S. Ravi, “Strongly-coupled modelling and analysis of energy harvesting devices,” *PAMM*, vol. 16, no. 1, pp. 505–506, 2016. (Cited on page 20.)

[64] K. Y. Sze and A. Ghali, “Hybrid hexahedral element for solids, plates, shells and beams by selective scaling,” *International Journal for Numerical Methods in Engineering*, vol. 36, no. 9, pp. 1519–1540, 1993. (Cited on page 22.)

[65] S.-N. Chen, G.-J. Wang, and M.-C. Chien, “Analytical modeling of piezoelectric vibration-induced micro power generator,” *Mechatronics*, vol. 16, no. 7, pp. 379 – 387, 2006. (Cited on page 22.)

[66] J. Becker, O. Fein, M. Maess, and L. Gaul, “Finite element-based analysis of shunted piezoelectric structures for vibration damping,” *Computers & Structures.*, vol. 84, pp. 2340–2350, Dec. 2006. (Cited on page 22.)

[67] C. C. Wu, K. Y. Sze, and Y. Q. Huang, “Numerical solutions on fracture of piezoelectric materials by hybrid element,” *Solids and structures*, vol. 38, pp. 4315–4329, 2001. (Cited on page 40.)

[68] T. J. R. Hughes and G. M. Hulbert, “Space-time finite elmement methods for elastodynamics: formulations and error estimates,” *Computer Methods in Applied Mechanics and Engineering*, vol. 66, pp. 339–363, 1988. (Cited on pages 40, 48 and 68.)

[69] K. Y. Sze and L. Q. Yao, “Modelling smart structures with segmented piezoelectric sensors and actuators,” *Journal of Sound and Vibration*, vol. 235, no. 3, pp. 495 – 520, 2000. (Cited on page 44.)

[70] J. Argyris and D. Scharpf, “Finite elements in time and space,” *Nuclear Engineering and Design*, vol. 10, no. 4, pp. 456 – 464, 1969. (Cited on pages 48 and 68.)

[71] A. Zilian and A. Legay, “The enriched space–time finite element method (est) for simultaneous solution of fluid–structure interaction,” *International Journal for Numerical Methods in Engineering*, vol. 75, no. 3, pp. 305–334, 2008. (Cited on pages 48, 68 and 70.)

[72] T. E. Tezduyar, S. Sathe, R. Keedy, and K. Stein, “Space–time finite element techniques for computation of fluid–structure interactions,” *Computer Methods in Applied Mechanics and Engineering*, vol. 195, pp. 2002–2027, 2006. (Cited on pages 48, 50 and 68.)

[73] K. Y. Sze, X.-M. Yang, and H. Fan, “Electric assumptions for piezoelectric laminate analysis,” *International Journal of Solids and Structures*, vol. 41, no. 9–10, pp. 2363 – 2382, 2004. (Cited on page 54.)

[74] M. Behr and T. Tezduyar, "Finite element solution strategies for large-scale flow simulations," *Computer Methods in Applied Mechanics and Engineering*, vol. 112, no. 1, pp. 3 – 24, 1994. (Cited on page 69.)

[75] T. H. H. Pian and D.-P. Chen, "Alternative ways for formulation of hybrid stress elements," *Numerical methods in engineering*, vol. 18, pp. 1679–1684, 1982. (Cited on page 71.)

[76] T. H. H. Pian and P. Tong, "Relations between incompatible displacement model and hybrid stress model," *Numerical methods in engineering*, vol. 22, pp. 173–181, 1986. (Cited on page 71.)

[77] U. Küttler, C. Förster, and W. A. Wall, "A solution for the incompressibility dilemma in partitioned fluid–structure interaction with pure dirichlet fluid domains," *Computational Mechanics*, vol. 38, no. 4, pp. 417–429, 2006. (Cited on page 74.)

[78] U. Küttler and W. A. Wall, "Fixed-point fluid–structure interaction solvers with dynamic relaxation," *Computational Mechanics*, vol. 43, no. 1, pp. 61–72, 2008. (Cited on pages 74 and 80.)

[79] K.-J. Bathe and H. Zhang, "A mesh adaptivity procedure for cfd and fluid-structure interactions," *Computers & Structures*, vol. 87, no. 11–12, pp. 604 – 617, 2009. Fifth MIT Conference on Computational Fluid and Solid Mechanics. (Cited on pages 74 and 80.)

[80] S. Rugonyi and K. Bathe, "On finite element analysis of fluid flows fully coupled with structural interactions," *CMES - Computer Modeling in Engineering and Sciences*, vol. 2, no. 2, pp. 195–212, 2001. (Cited on page 80.)